STRUCTURAL STUDIES BY CRYO-ELECTRON TOMOGRAPHY OF TWO INITIATION COMPLEXES OF THE IMMUNE SYSTEM:

C1-IgG$_6$ AND NAIP5-NLRC4

Christoph Andreas Diebolder

The research described in this thesis was performed at the group of Crystal and Structural Chemistry, Bijvoet Center for Biomolecular Research, Utrecht University, Utrecht, The Netherlands and

at the Department of Molecular Cell Biology, Leiden University Medical Center, Leiden, The Netherlands.

Front picture by: Joost Bakker, scicomvisuals.com;

Cover design and back picture by: Christoph Diebolder

Printed by: Proefschriftmaken.nl, Uitgeverij BOXPress, 's-Hertogenbosch

Published by: Uitgeverij BOXPress, 's-Hertogenbosch

ISBN: 978-94-6295-346-8

STRUCTURAL STUDIES BY CRYO-ELECTRON TOMOGRAPHY OF TWO INITIATION COMPLEXES OF THE IMMUNE SYSTEM: C1-IgG$_6$ AND NAIP5-NLRC4

STRUCTUREEL ONDERZOEK
MET BEHULP VAN CRYO-ELEKTRONEN-TOMOGRAFIE
VAN TWEE AKTIVERENDE COMPLEXEN VAN HET IMMUUNSYSTEEM:
C1-IgG$_6$ EN NAIP5-NLRC4
(met een samenvatting in het Nederlands)

STRUKTURUNTERSUCHUNGEN MITTELS
KRYO-ELEKTRONENTOMOGRAFIE
ZWEIER INITIATIONSKOMPLEXE DES IMMUNSYSTEMS:
C1-IgG$_6$ UND NAIP5-NLRC4
(mit einer Zusammenfassung in deutscher Sprache)

Proefschrift

ter verkrijging van de graad van doctor aan de Universiteit Utrecht op gezag van de rector magnificus, prof. dr. G.J. van der Zwaan, ingevolge het besluit van het college voor promoties in het openbaar te verdedigen op woensdag 30 september 2015 des middags te 12.45 uur

door

Christoph Andreas Diebolder

geboren op 4 april 1981
te Geislingen an der Steige, Duitsland

Promotoren: Prof. dr. P. Gros
Prof. dr. ir. A.J. Koster
Copromotor: Dr. R.I. Koning

The research described in this thesis was accomplished with financial support from the *European Research Council* (ERC), advanced grant 233229 (COCO).
Print of this thesis was financially supported by *Genmab B.V.*, Utrecht and through a publication grant of the *Stichting tot Bevordering van de Electronenmicroscopie in Nederland* (SEN).

meiner Familie

TABLE OF CONTENTS

CHAPTER 1

GENERAL INTRODUCTION

Christoph A. Diebolder[1,2]

[1]Crystal and Structural Chemistry, Bijvoet Center for Biomolecular Research, Department of Chemistry, Faculty of Science, Utrecht University, 3584 CH Utrecht, The Netherlands.

[2]Department of Molecular Cell Biology, Section Electron Microscopy, Leiden University Medical Center, 2300 RC Leiden, The Netherlands.

RECOGNITION OF PATHOGENS BY THE IMMUNE SYSTEM

The human body faces permanent attack by a multiplicity of pathogens e.g. bacteria, fungi or viruses. Our immune system has developed powerful defense mechanisms against these threats. The first line of this defense is formed by physical and chemical barriers such as the epidermis of the skin or secreted proteases. Once the invaders conquer this first phalanx, they are attacked by the weaponry of the innate and –if the pathogen had been previously encountered - adaptive immune system. However, rigorous differentiation between self and non-self is the pivotal step for a successful immune reaction (Fig.1).

Innate immune responses are based on general recognition of structures that are typical for pathogens. At the same time these patterns must be significantly different from any host structure to prevent the immune system from attacking the own body. Examples for such structures are components of the bacterial cell wall such as lipopolysaccharides, the building block of the bacterial flagellum flagellin, or double stranded RNA which codes genetic information of viruses. Such structures are called Pathogen-Associated Molecular Patterns, PAMPs (*1*). Accordingly, the host's immune system receptors which are designed to recognize these structures are PAMP Recognition Receptors, (also Pattern recognition receptors) or PRRs. PRRs have a crucial role in the innate immune system, because of their ability to promptly recognize a variety of pathogens. Induction of a broad arsenal of effector functions of the innate immune system make PRRs the spearheads in this early immune response, providing the host with sufficient time and information needed to develop highly specific weaponry during the adaptive immune response (*2,3*). PRRs can be classified into three groups according to their site of action. The first group comprises extracellular freely floating receptors such as Pentraxins (e.g. CRP), Ficolins, and Collectins (e.g. Mannose binding lectin (MBL)), which are able to activate the complement system by the MBL-pathway (*4*). After initial recognition, the complement cascade provides efficient signal amplification and several powerful effector mechanisms that will lead to efficient killing and clearance of the pathogen (*5*). Alternatively, PAMPs can be detected by cell-bound PRRs. The membrane spanning Toll-like receptors belong in this category, being able to transduce the received signal via dimerization to the cytosolic compartment inside the cell. Effector functions of TLR signaling include cytokine formation leading to inflammation (*6*). Thirdly, pathogen recognition can also take place inside the cytosol. This is accomplished by another group of PRRs, all containing a Nucleotide Oligomarization Domain and consequently called the NOD-like receptors, short NLRs. NLR signaling leads to formation of large complexes with caspase activity, called inflammasomes, that cause inflammation by cytokine formation and pyroptotic cell death (*7*).

In contrast, adaptive immune response allows recognition of virtually any specific structure using highly specific antibodies as receptors (*8*). Antibodies have to mature in the course of an infection to reach optimal affinity for their specific targets. However, once the immune system designed the right antibody for a specific target, it remembers it to be able to quickly respond to a future infection and thus making the host immune to recurrent infections by this pathogen. Antibodies act by various effector functions: They neutralize by binding to and thus blocking of crucial interactions sites, they crosslink and aggregate pathogens, or they label target cells so they are recognized and either killed by effector cells or digested by phagocytes (*9*). They further induce the classical pathway of complement activation. This pathway links the specific recognition of antigens by the adap-

tive immune response with effector functions of the innate immunity cascade which evolutionary was designed for the response to general PAMPs, thus "complementing" other effector functions of the adaptive immune system.

This thesis is focused on structural investigation of two different mechanisms for pathogen recognition. First, activation of the complement system by antibodies -called the classical pathway of complement activation- and second the sensing of intracellular PAMPS by the so-called NAIP5-NRC4 inflammasome, giving rise to a more detailed introduction of these two systems.

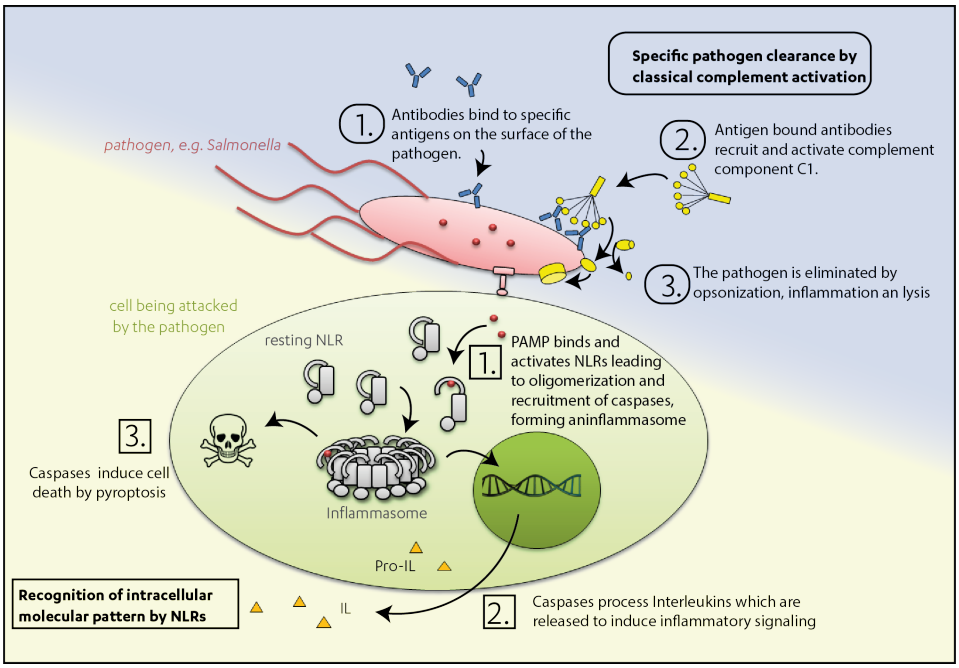

Fig. 1. Recognition of general and specific pathogenic patterns by the innate and adaptive immune system. A human cell (green) that is threatened by a bacterial pathogen (red) is protected by several pathways of the innate (yellow) or adaptive (blue) immune system. Pathogen-associated molecular patterns (PAMPs), such as bacterial flagellin, which enters the cell via bacterial sectretion systems, are recognized by NOD-like receptors, inducing formation of an inflammasome that leads to infammation and cell death by pyroptoses.

In the course of an infection, antibodies (blue) are formed that recognize specific structures on the surface ot the pathogen, inducing multiple effector mechanisms, e.g. activation of the classical pathway of the complement system which labels the pathogen for attack by immune cells and directly kills the pathogen. Figure adapted from (*10*).

THE CLASSICAL PATHWAY OF COMPLEMENT ACTIVATION

The complement system was discovered, described and named in the 19th century by the pioneering immunologists Hans Buchner, Richard Pfeiffer, Jules Bordet and Paul Ehrlich (*11,12,13,14*). The system consists of ~30 proteins either circulating in the plasma or being bound to cell surfaces. These proteins act together in a tightly regulated cascade to detect and kill pathogens (*5,15*). Central element of the complement cascade is the C3 convertase, an enzyme complex on the surface of the pathogen that leads to signal amplification and induces multiple effector functions that will eliminate the pathogen (*16*). Formation of active C3 convertases can be initiated by three different routes of activation. First, they are formed spontaneously in the so-called tick-over pathway. This will cause random complement activation on virtually any surface. However, cells of the own body will protect themselves by exposing regulatory proteins on their surfaces, leading to inactivation of C3 convertases. Secondly, complement provides its own PRRs, e.g. MBL which binds to mannose or N-acetyl-glucosamine on bacterial surfaces. This binding induces activation of serine proteases that in turn form an active C3 convertase. Complement activation by PAMP recognition through MBL or other lectins is referred to as the MBL-pathway (*4*). Third, complement can be triggered by the classical pathway (CP), named so because it was the first one to be discovered (*17*). It is initiated by the first component of the complement, the C1-complex (Fig.2). C1 consists of a pattern recognition molecule C1q with six globular binding domains which are connected by collagen-like arms, making it appearing like a bouquet of flowers (*18*). C1 additionally contains two of each serine proteases C1r and C1s which are activated upon binding of several of the globular binding domains of C1q to its target, once again leading to formation of an active C3 convertase. C1q binds like MBL to certain PAMPs, such as lipoteichoic acid or CRP-labeled phosphocholine. Moreover, it binds to antigen-bound antibodies, again inducing formation of an active C3-convertase and thus complementing other effector functions of antibodies and therefore presents an important link between innate and adaptive immunity. The classical pathway can be activated by several immune complexes. Secreted IgM is the strongest complement activator because as pentameric or hexameric antibody it contains five to six proximate binding sites for C1q that become accessible upon antigen binding of IgM (*19*). Also, the monomeric immunoglobulins IgG1 and IgG3 are capable of classical pathway activation. However, several IgGs must bind antigens in close proximity in order to allow several C1q head pieces to bind and activate C1r and C1s thus starting off the complement cascade (*20*). Classical complement activation is considered to be a crucial protection mechanism against several bacterial infections such as Neisserial meningitis. That is why individuals with classical pathway deficiencies suffer from recurrent and life threatening infections caused by otherwise harmless commensal bacteria (*21*). These individuals are further prone to systemic lupus erythematosus, a condition characterized by the inability to clear circulating immune complexes that lead to inflammation and tissue damage (*22*). Despite its relevance, little is known about the molecular requirements for efficient complement activation by antigen bound IgG antibodies. Based on structural and functional insights textbooks depict C1-antibody-antigen as presented in Fig. 2C (*2*). Here, two IgGs bind bivalently to the antigens in a short relative distance but do not interact with each other, exposing C1q binding sites in their constant region to allow binding and activation of C1. However, details about the binding valence of antibodies or C1q, the stoichiometry between C1q and IgG and possible interaction between several antibodies within the complex remain unknown.

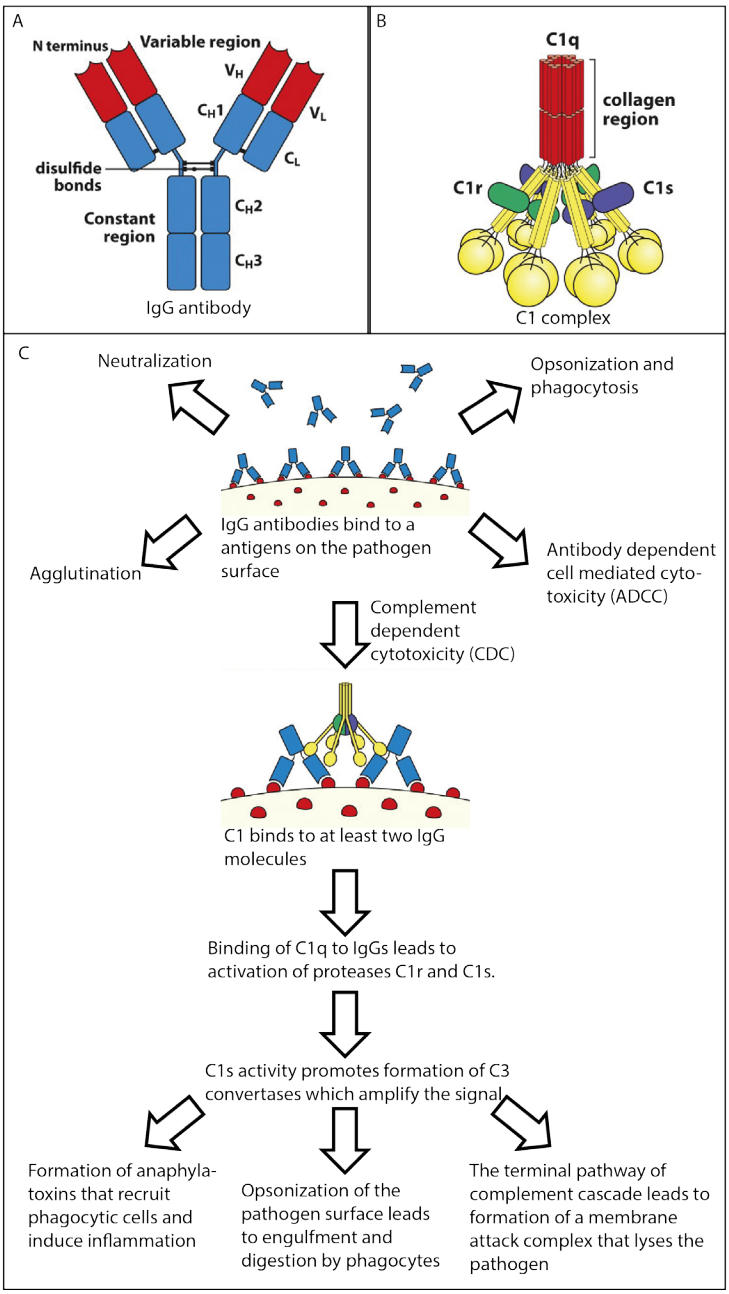

Fig. 2. Schematic of classical complement pathway activation by IgG and effector functions. A: Domain organisation of an IgG antibody; constant segments (blue), variable regions (red). B: C1 complex consisting of C1q (yellow/red) and two copies each of C1r (green) and C1s (purple). C1q itself is a hexemer of trimers which contain globular head regions (yellow) and a connecting collagen-like region (red). C: Classical complement pathway activation by IgG antibodies and induced effector functions. Central element is the C1-antibody-antigen complex. Cartoons of IgG, C1 and the C1-IgG-antigen complex reproduced from (*2*) with permission from Garland Science.

THE NAIP5-NLRC4 INFLAMMSOME

The term inflammasome was coined little more than ten years ago by Jürg Tschopp et al. (*23,24*). It describes a large cytosolic signaling protein complex composed of PAMPs, NOD-like receptors (NLRs) that act as PRRs, adaptor molecules which are signal amplifiers, and caspases as effector molecules.

The NAIP5-NLRC4 is a heterooligomeric inflammasome in that it requires recruitment of two different NLRs, NAIP5 and NLRC4 into the same inflammasome (*25*). NAIP5 acts as PRR and senses bacterial PAMPs such as Type-III-secretion system and bacterial flagellin. Upon recognition it undergoes conformational changes that allow recruitment and ATP dependent polymerization of the adapter NLRC4. Polymerized NLRC4 is thought to expose proximate CARD domains that allow in turn recruitment and and polymerization of pro-caspase1, which is autoactivated and cleaves as active enzyme pro-IL1β and pro-IL18 - two important cytokines with proinflammatory properties. NAIP5-NLRC4 deficiencies are associated with disorders such as Muckle-Wells Syndrome and Familial Cold Autoinflammatory Syndrome (*26*).

Much of our limited knowledge about NAIP5-NLRC4 inflammasome mechanism is based on biochemical experiments (*27*). Structural information only recently started to emerge and is mainly based on flourescence light microscopy, showing that a cell forms a single inflammasome of enourmeous size (*28*) and very limited high-resolution data, most importantly for the inactive crystal structure of core domains of NLRC4 (*29*). Based on homologies, structural similarity with apoptosomes is assumed (*30*; Fig.3). Indeed, initial negative stain EM suggests similarities (*25*) and raises important questions: Why is this structure so much smaller than the one seen in light microscopy? What are the oligomeric state, composition and stoicheometry within the complex? In other words: What is the quaternary structure of the assemled NAIP5-NLRC4 inflammasome?

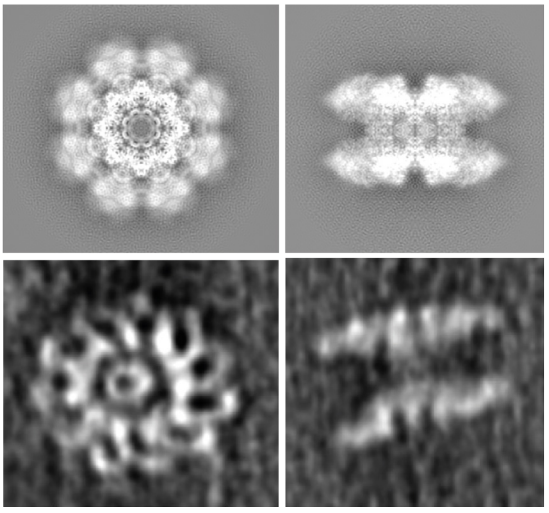

Fig. 3. Structural similarity of apoptosomes and inflammasomes. A: Top (left) and side view (right) projections of a single particle reconstruction of the DARK aopoptosomes, EMDB entry EMD-2870,(*30*). B: Corresponding sections through electron tomogram of negatively stained NAIP5-NLRC4 inflammasome, reprinted form (*25*) with permission. Both structures seem to resemble double discs that are formed by homotypic CARD-CARD interaction.

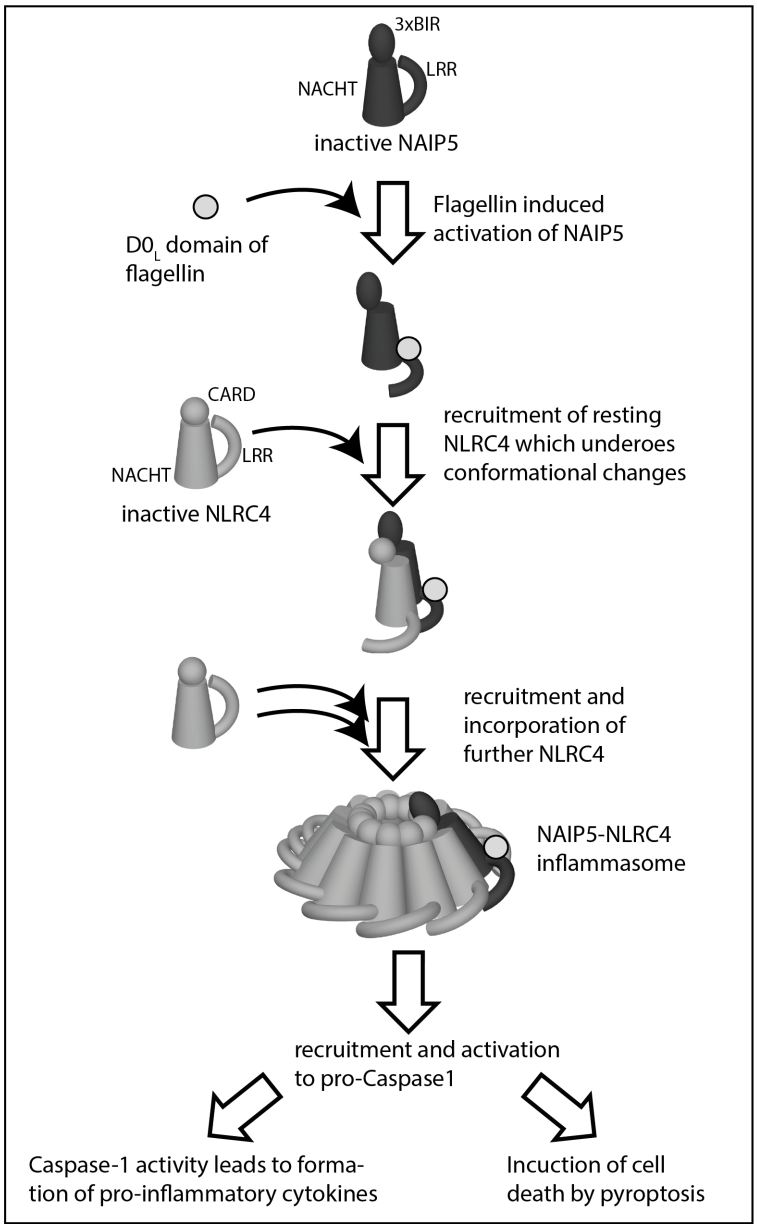

Fig. 4. Schematic model of flagellin-induced NAIP5-NLRC4 inflammasome activation and effector functions. Resting NAIP5 undergoes conformational changes upon interaction with flagellin. Activated NAIP5 then recruits resting NLRC4, which in turn undergoes conformational changes. This activated form of NLRC4 is recognized by resting NLRC4, which results in progressive incorporation of NLRC4 into a disc-like complex that exposes the NLRC4 CARD domains at one face and thus creating a platform suitable for procaspase-1 recruitment and activation. Figure adapted from (*25*) with permission.

CRYO-ELECTRON TOMOGRAPHY AS A TOOL IN STRUCTURAL IMMUNOLOGY

Structural investigation of biomolecular complexes is important to understand their functions. Electron microscopy (EM) has proven to be a very useful tool structural studies of protein complexes such as complement activating immune complexes or inflammasomes because it allows to depict them in their native environment, e.g. in context of a biological membrane (*31*). The resolution obtained by EM techniques is typically in the range of a few nm, which is mandatory to reveal the quaternary structure of multiprotein complexes. Other techniques that allow to obtain atomic resolution are limited to smaller molecule sizes (NMR spectroscopy) or require crystallized samples (X-ray crystallography). Biological samples are highly sensitive to electron beam radiation and the structure will be destroyed while the sample is being observed in the microscope. To cope with this, the total electron dose being used for imaging is limited, resulting in underexposed images with very low contrast. Additionally, the electrons strongly interact with any molecule while progressing through the electromagnetic lens system of the EM. Thus high vacuum conditions within the EM column are required to prevent electron scattering which would hinder imaging of the sample. As a consequence, samples containing protein complexes in solution have to be pretreated in order to withstand the harsh conditions in the EM –the high radiation and vacuum- as well as to increase the contrast. Traditionally, this is achieved by the so-called negative staining technique. This technique makes use of the fact that heavy metals atoms strongly scatter electrons are thus not transparent to the electron beam providing strong amplitude contrast to biological material consisting of elements with low atomic numbers (*32*). The sample is often chemically cross-linked in order to increase stability and keep the protein complex in a fixed conformation (*33*). The embedded sample is stable in vacuum, the stain itself resists high radiation and provides high amplitude contrast so that the sample is seen as a relief-like imprint in the stain. This allows high contrast imaging up to sub nanometer resolution (*34*). However, the sample is objected to harsh treatment involving dehydration and strong mechanical forces introducing severe artifacts limiting the validity of the nominal high-resolution data. Despite these downsides, negative stain transmission electron microscopy (TEM), for more than 50 years, has been a widely applied method in structural biology and fundamental parts of our current knowledge on antibodies, immune complexes and the complement system are directly derived from groundbreaking negative stain TEM studies as reviewed by Roux (*35*) and Kishore and Reid (*18*). Besides, first insights in the quaternary structure of inflammasomes were obtained by negative stain EM (*25*).

Cryo-preservation techniques were introduced to overcome the limitations of negative staining (*36*). Here, the biological sample is vitrified by very fast freezing, allowing to fix it while staying in its native, fully hydrated state. Moreover, biomolecules are imaged directly and not indirectly as stained imprints, which results in cryo-EM being a strongly emerging technique in structural biology. However, vitrified samples are highly sensitive to electron beam-induced radiation damage, limiting the total electron dose that can be used to image a sample and leading to very noisy data. This constraint ultimately limits the resolution obtainable in cryo-EM, and enormous efforts during sample preparation, data collection and image processing need to be undertaken in order to reach optimal resolution.

Ultimately, the resolution of a three-dimensional reconstruction can only be increased by averaging of many similar particles. In single particle reconstructions, individual protein complexes are

imaged once in one orientation, requiring many thousands of particles imaged in many orientations to obtain a full 3D reconstruction, which can reach atomic resolution (*37*). Nevertheless, often this technique is not applicable because the sample does not contain enough separated similar particles in all orientations needed. This is usually the case for complexes that cannot be obtained in high concentration, that are flexible, or are aimed to be imaged in their native environment e.g. on a biological membrane such as antibodies binding to an antigen on a bacterial membrane. In these cases, electron tomography (ET) can be used to obtain a three-dimensional reconstruction of unique samples (*38*). This is done by imaging this sample from many different angles, but because of the radiation sensitivity, the final reconstruction will be very noisy and incomplete and usually, the resolution too low to reveal the quaternary structure of the protein complex. Averaging of several (sub) tomograms of different particles offers then a possibility to increase this resolution (*39*).

To reach this, the quality of the initial cryo-tomograms needs to be as good as possible and much attention needs to be paid to the individual steps during the reconstruction process, such as tilt series alignment or correction of the contrast transfer function. But how can the quality of the resulting tomogrambe judged best? Since the three dimensional dataset is incomplete and thus anisotropic, the resolution of a reconstruction cannot be expressed in a single number. However, this issue has been neglected for a long time and rather simplistic approximations are used that are solely based on theoretical considerations (*40*), ignore anisotropy, or only try to estimate resolution in a single direction (*41,42*). Knowing about this shortcoming, electron microscopists today even only rarely apply any these methods to quantitatively estimate quality of their data sets.

SCOPE OF THESIS

Antibodies belong to the best studied objects in life sciences. The IgG structure is known to atomic resolution, we know about its countless interactions that resulted in elaborate models for its many roles in immunity and disease and we use antibodies in many applications ranging from research via diagnostics to biotechnology and therapy. The more surprising it may be that there is still fundamental lack in understanding how antibodies perform one of their most important biological functions: Activation of the classical complement pathway. What are the structural requirements and constraints for efficient complement activation by IgG immune complexes? **Chapter 2** describes the structure of C1–antibody complexes by cryo-EM and many biochemical techniques. Based on this data we provide a general CP activation model by IgG antibodies.

Chapter 3 provides first structural insights to the possible activation mechanisms of the hetero-oligomeric NAIP5-NLRC4 inflammasome that is initiated in presence of bacterial flagellin. We use negative stain and cryo-electron microscopy and tomography to image several recombinantly expressed complexes at different stages of oligomerization and combine our three-dimensional data with recent structural findings on inactive NLRC4 to an inflammasome activation model. NOD-like receptors have only relatively recently been discovered and their multifold role in immunity, homeostasis and disease is subject of intense worldwide research activity. How do these pattern recognition receptors sense and transduce the signal of intracellular pathogen assotiated molecular patterns such as bacterial flagellin and what drives them to form large multimeric com-

plexes called inflammasomes?

In **Chapter 4** we review factors intrinsically limiting the resolution in cryo electron tomography and discuss which factors need to be considered during sample preparation, data collection and image processing to achieve as high resolution as possible. We further highlight how foreseeable technical developments might be able to shift current practical and theoretical resolution limits in cryo-ET towards atomic resolution. Three-dimensional imaging of protein complexes such as membrane-bound complement components or active inflammasomes aims for the highest attainable resolution.

In **Chapter 5** we set out to test a new method for the estimation of resolution isotropy that might help to compare data sets and optimize acquisition and reconstruction parameters. Any structural data set needs to be validated in order to be able to compare different datasets and improve their quality. Consequently, objective validation criteria such as for resolution estimation are crucial. In cryo-ET, three-dimensional sampling is incomplete which makes it difficult to measure "the resolution" of a dataset.

Finally, **Chapter 6** summarizes the data presented in this thesis and discusses the results in context of recent literature. We further provide an outlook on how the structural models of C1-immune complexes and activated inflammasomes might be able to explain their function and therefore contribute to understanding and fighting diseases.

REFERENCES

1. R Medzhitov, CA Janeway, Innate immunity: the virtues of a nonclonal system of recognition, *Cell* **91**, 295-298 (1997).
2. K. M. Murphy, *Janeway's immunobiology*, (2011).
3. P. J. Delves, S. J. Martin, D. R. Burton, and I. M. Roitt, *Roitt's essential immunology*, (2011).
4. U. Holmskov, S. Thiel, and J. C. Jensenius, Collectins and ficolins: humoral lectins of the innate immune defense, *Annual review of immunology* **21**, 547-578 (2003).
5. M. J. Walport, Complement. First of two parts, *The New England journal of medicine* **344,** 1058-1066 (2001).
6. T. Kawai and S. Akira, The role of pattern-recognition receptors in innate immunity: update on Toll-like receptors, *Nature immunology* **11**, 373-384 (2010).
7. T. D. Kanneganti, M. Lamkanfi, and G. Nunez, Intracellular NOD-like receptors in host defense and disease, *Immunity* **27**, 549-559 (2007).
8. D. R. Davies and H. Metzger, Structural basis of antibody function, *Annual review of immunology* **1**, 87-115 (1983).
9. M. Brüggemann, G. T. Williams, C. I. Bindon, M. R. Clark, M. R. Walker, R. Jefferis, H. Waldmann, and M. S. Neuberger, Comparison of the effector functions of human immunoglobulins using a matched set of chimeric antibodies, *The Journal of experimental medicine* **166**, 1351-1361 (1987).
10. E. F. Halff, *Structural and functional studies on Nod like receptors: insights into NAIP/ NLRC4 inflammasome formation*, (2013).
11. H. Buchner, Über die höhere Natur der bakterientötenden Substanz in Blutserum, *Zentralbl*

Bakteriol **6**, 561-572 (1889).
12. R. Pfeiffer, Über die specifische Bedeutung der Choleraimmunität, *Zeitschrift für Hygiene und Infektionskrankheiten* **17**, 355-400 (1894).
13. J. Bordet, Contribution a l'etude du serum chez les animaux vaccines, (1895).
14. P. Ehrlich and H. Sachs, Über die Vielheit der Komplemente im Serum, *Berl. klin. Wschr* **297**, 335 (1902).
15. D. Ricklin, G. Hajishengallis, K. Yang, and J. D. Lambris, Complement: a key system for immune surveillance and homeostasis, *Nature immunology* **11**, 785-797 (2010).
16. P. Gros, F. J. Milder, and B. J. Janssen, Complement driven by conformational changes, *Nature Reviews Immunology* **8**, 48-58 (2008).
17. R. R. Porter and K. B. M. Reid, Activation of the complement system by antibody-antigen complexes: the classical pathway, *Advances in protein chemistry* **33**, 1-71 (1979).
18. U. Kishore and K. B. Reid, C1q: structure, function, and receptors, *Immunopharmacology* **49**, 159-170 (2000).
19. D. M. Czajkowsky and Z. Shao, The human IgM pentamer is a mushroom-shaped molecule with a flexural bias, *PNAS* **106**, 14960-14965 (2009).
20. C. Gaboriaud, N. M. Thielens, L. A. Gregory, V. Rossi, J. C. Fontecilla-Camps, and G. J. Arlaud, Structure and activation of the C1 complex of complement: unraveling the puzzle, *Trends in immunology* **25**, 368-373 (2004).
21. H. D. Pettigrew, S. S. Teuber, and M. E. Gershwin, Clinical significance of complement deficiencies, *Annals of the New York Academy of Sciences* **1173**, 108-123 (2009).
22. L. A. Trouw, A. M. Blom, and P. Gasque, Role of complement and complement regulators in the removal of apoptotic cells, *Molecular immunology* **45**, 1199-1207 (2008).
23. F. Martinon, K. Burns, and J. Tschopp, The inflammasome: a molecular platform triggering activation of inflammatory caspases and processing of proIL-b, *Mol cell* **10**, 417-426 (2002).
24. K. Schroder and J. Tschopp, The inflammasomes, *Cell* **140**, 821-832 (2010).
25. E. F. Halff, C. A. Diebolder, M. Versteeg, A. Schouten, T. H. Brondijk, and E. G. Huizinga, Formation and structure of a NAIP5-NLRC4 inflammasome induced by direct interactions with conserved N-and C-terminal regions of flagellin, *JBiol Chem* **287**, 38460-38472 (2012).
26. D. R. Mason, P. L. Beck, and D. A. Muruve, Nucleotide-binding oligomerization domain-like receptors and inflammasomes in the pathogenesis of non-microbial inflammation and diseases, *Journal of innate immunity* **4**, 16-30 (2011).
27. J. Tenthorey, E. Kofoed, M. Daugherty, H. Malik, and R. Vance, Molecular Basis for Specific Recognition of Bacterial Ligands by NAIP/NLRC4 Inflammasomes, *Mol cell* **54**, 17-29 (2014)
28. S. M. Man, L. J. Hopkins, E. Nugent, S. Cox, I. M. Glück, P. Tourlomousis, J. A. Wright, P. Cicuta, T. P. Monie, and C. E. Bryant, Inflammasome activation causes dual recruitment of NLRC4 and NLRP3 to the same macromolecular complex, *PNAS* **111**, 7403-7408 (2014).
29. Z. Hu, C. Yan, P. Liu, Z. Huang, R. Ma, C. Zhang, R. Wang, Y. Zhang, F. Martinon, and D. Miao, Crystal structure of NLRC4 reveals its autoinhibition mechanism, *Science* **341**, 172-175 (2013).
30. Y. Pang, X. c. Bai, C. Yan, Q. Hao, Z. Chen, J. W. Wang, S. H. Scheres, and Y. Shi, Structure of the apoptosome: mechanistic insights into activation of an initiator caspase from Drosophila, *Genes & development* **29**, 277-287 (2015).

31. J. Frank, *Three-dimensional electron microscopy of macromolecular assemblies*, (1996).
32. R. M. Glaeser, Limitations to significant information in biological electron microscopy as a result of radiation damage, *Journal of ultrastructure research* **36**, 466-482 (1971).
33. S. Brenner and R. W. Horne, A negative staining method for high resolution electron microscopy of viruses, *Biochimica et biophysica acta* **34**, 103-110 (1959).
34. S. De Carlo and J. R. Harris, Negative staining and cryo-negative staining of macromolecules and viruses for TEM, *Micron* **42**, 117-131 (2011).
35. K. H. Roux, Immunoglobulin structure and function as revealed by electron microscopy, *International archives of allergy and immunology* **120**, 85-99 (1999).
36. J. Dubochet, Cryo-EM first thirty years, *Journal of microscopy* **245**, 221-224 (2012).
37. X. Zhang, L. Jin, Q. Fang, W. H. Hui, and Z. H. Zhou, 3.3 Å cryo-EM structure of a nonenveloped virus reveals a priming mechanism for cell entry, *Cell* **141**, 472-482 (2010).
38. R. I. Koning and A. J. Koster, Cryo-electron tomography in biology and medicine, *Annals of Anatomy-Anatomischer Anzeiger* **191**, 427-445 (2009).
39. G. Zanetti, J. A. Briggs, K. Grünewald, Q. J. Sattentau, and S. D. Fuller, Cryo-electron tomographic structure of an immunodeficiency virus envelope complex in situ, *PLoS pathogens* **2**, e83 (2006).
40. R.A. Crowther, D.J. Derosier, A. Klug, Reconstruction of 3-dimensional structure from projections and its application to electron microscopy, *Proceedings of the Royal Society of London Series A Mathematical and Physical Sciences* **317**,319-340 (1970).
41. P.A. Penczek, and J.Frank, *Resolution in electron tomography. Electron Tomography* 307-330 (2006)
42. G. Cardone, K. Grünewald, and A. C. Steven, A resolution criterion for electron tomography based on cross-validation, *Journal of structural biology* **151**, 117-129 (2005).

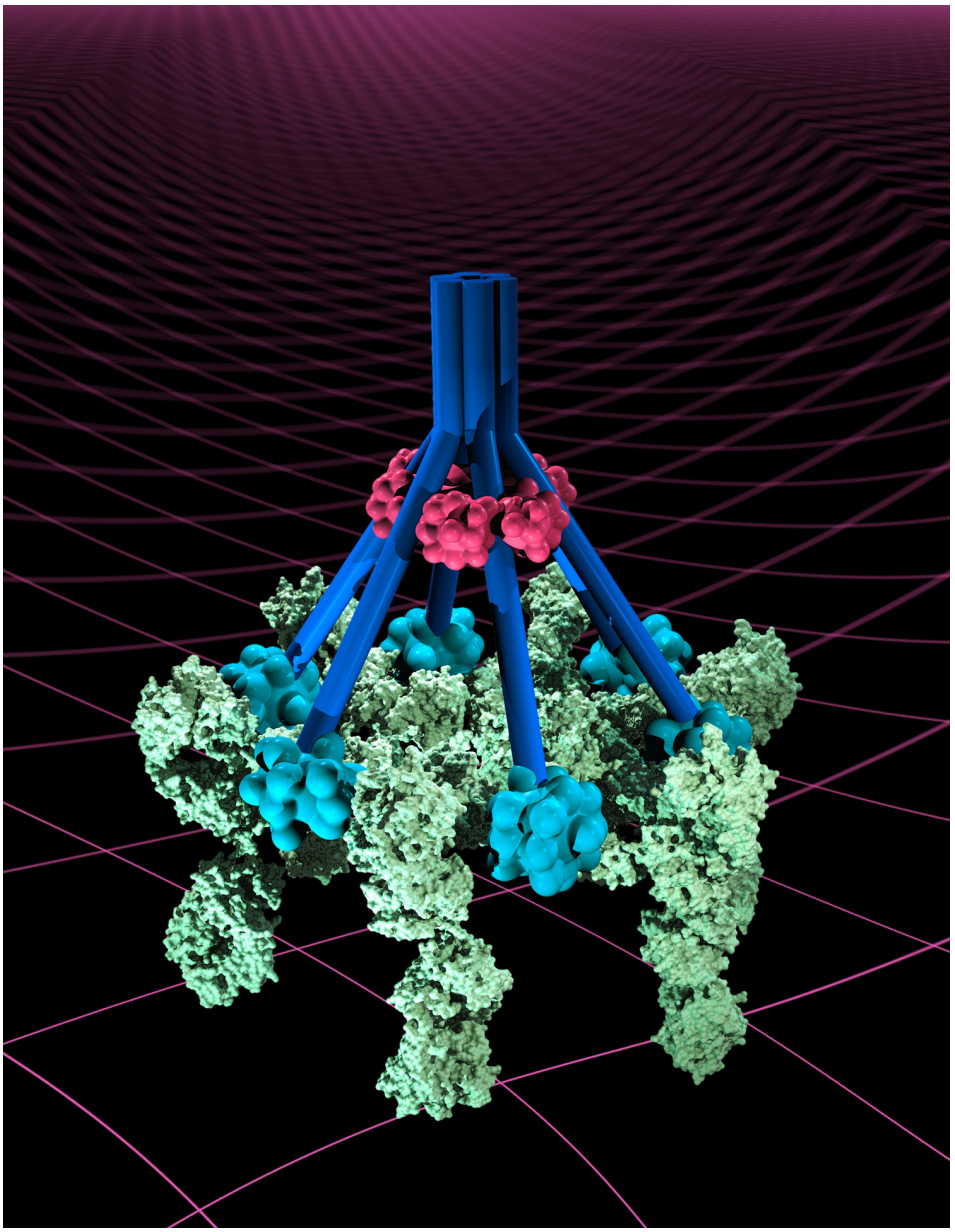

(c) Joost Bakker, scicomvisuals.com

CHAPTER 2

Complement is Activated by IgG Hexamers Assembled at the Cell Surface

Christoph A. Diebolder[1,2,†], Frank J. Beurskens[3,†], Rob N. de Jong[3], Roman I. Koning[2], Kristin Strumane[3], Margaret A. Lindorfer[4], Marleen Voorhorst[3], Deniz Ugurlar[1], Sara Rosati[5], Albert J.R. Heck[5], Jan G.J. van de Winkel[3,6], Ian A. Wilson[7,8], Abraham J. Koster[2], Ronald P. Taylor[4], Erica Ollmann Saphire[9], Dennis R. Burton[8,9,10], Janine Schuurman[3], Piet Gros[1,*], and Paul W.H.I. Parren[3,*]

Science, Vol. **343** no. 6176 pp. 1260-1263 (2014)

[1]Crystal and Structural Chemistry, Bijvoet Center for Biomolecular Research, Department of Chemistry, Faculty of Science, Utrecht University, 3584 CH Utrecht, The Netherlands

[2]Department of Molecular Cell Biology, Section Electron Microscopy, Leiden University Medical Center, 2300 RC Leiden, The Netherlands

[3]Genmab, 3584 CM Utrecht, The Netherlands

[4]Department of Biochemistry and Molecular Genetics, University of Virginia School of Medicine, Charlottesville, VA 22908, USA

[5]Biomolecular Mass Spectrometry and Proteomics, Bijvoet Center for Biomolecular Research and Utrecht Institute for Pharmaceutical Sciences, Utrecht University, 3584 CH Utrecht, The Netherlands

[6]Immunotherapy Laboratory, Department of Immunology, University Medical Center, 3584 CX, Utrecht, the Netherlands

[7]Department of Integrative Structural and Computational Biology, The Scripps Research Institute, La Jolla, CA 92037, USA

[8]IAVI Neutralizing Antibody Center and Center for HIV/AIDS Vaccine Immunology and Immunogen Discovery, The Scripps Research Institute, La Jolla, CA 92037, USA

[9]Department of Immunology and Microbial Science, The Scripps Research Institute, La Jolla, CA 92037, USA

[10]Ragon Institute of MGH, MIT and Harvard, Cambridge, MA 02139, USA

† These authors contributed equally to this work

*Corresponding authors

ABSTRACT

Complement activation by antibodies bound to pathogens, tumors, and self antigens is a critical feature of natural immune defense, a number of disease processes, and immunotherapies. How antibodies activate the complement cascade, however, is poorly understood. We found that specific noncovalent interactions between Fc segments of immunoglobulin G (IgG) antibodies resulted in the formation of ordered antibody hexamers after antigen binding on cells. These hexamers recruited and activated C1, the first component of complement, thereby triggering the complement cascade. The interactions between neighboring Fc segments could be manipulated to block, reconstitute, and enhance complement activation and the killing of target cells, using all four human IgG subclasses. We offer a general model for understanding antibody-mediated complement activation and the design of antibody therapeutics with enhanced efficacy.

INTRODUCTION

Complement activation by antibodies initiates immune protection through the generation of an array of biologically active products including opsonins, anaphylatoxins, chemotactic agents, and membrane attack complexes (*1*, *2*). The classical pathway of complement is triggered when antigen-bound immunoglobulin M (IgM) or IgG antibody molecules bind C1, which consists of the multimeric pattern recognition molecule C1q and a heterotetramer of the proteases C1r and C1s (*3*, *4*). C1q binds a single IgG Fc segment with very low affinity (dissociation constant $K_d \approx 10^{-4}$ M) (*5*, *6*), and physiological C1 binding thus requires an increase in the apparent binding constant—for instance, through antigen-driven antibody clustering, which allows multivalent C1q binding (*7*). The molecular events governing complement activation, including the C1-antibody stoichiometry required for optimal activation, remain poorly understood (*3*, *8*–*13*). Here, we set out to characterize and visualize the first steps in complement activation by IgG at the molecular level.

RESULTS & DISCUSSION

In the structure of human anti–HIV-1 gp120 antibody IgG1-b12 at 2.7 Å resolution [Protein Data Bank (PDB) entry 1HZH] (*14*, *15*), the IgG Fc segments are arranged in a hexameric ring (Fig. 1A). A similar crystal packing is found for human antibody 2G12 (*16*). The spatial orientation of Lys^{322} (Fig. 1A), a critical residue in the C1q binding site on IgG, suggested a compatibility of the hexamer with the arrangement of the six antibody-binding headpieces in C1q. We hypothesized that IgG antibodies activate complement-dependent cytotoxicity (CDC) via ordered clustering into hexamers through specific noncovalent Fc interactions. To investigate this hypothesis, we used a peptide that has been shown to bind residues in the observed Fc-Fc interface (*17*) (Fig. 1B). The peptide inhibited CDC of human B cell lymphomas by CD20 antibody IgG1-7D8 and CD38 antibody IgG1-005 (Fig. 1C), both of which potently induce CDC by the classical pathway (*18*, *19*). Next, we generated interface mutations designed to weaken Fc-Fc interactions. We confirmed that antigen binding and C1q binding to randomly immobilized IgG1 (fig. S1) were mostly unaffected by the mutations. In contrast, the apparent avidity of C1q for cell-bound IgG1-7D8 mutated at positions Ile^{253}, His^{433}, or Asn^{434} decreased by as much as a factor of 20 (Fig. 1D, fig. S2A, and table S1); this resulted in reduced

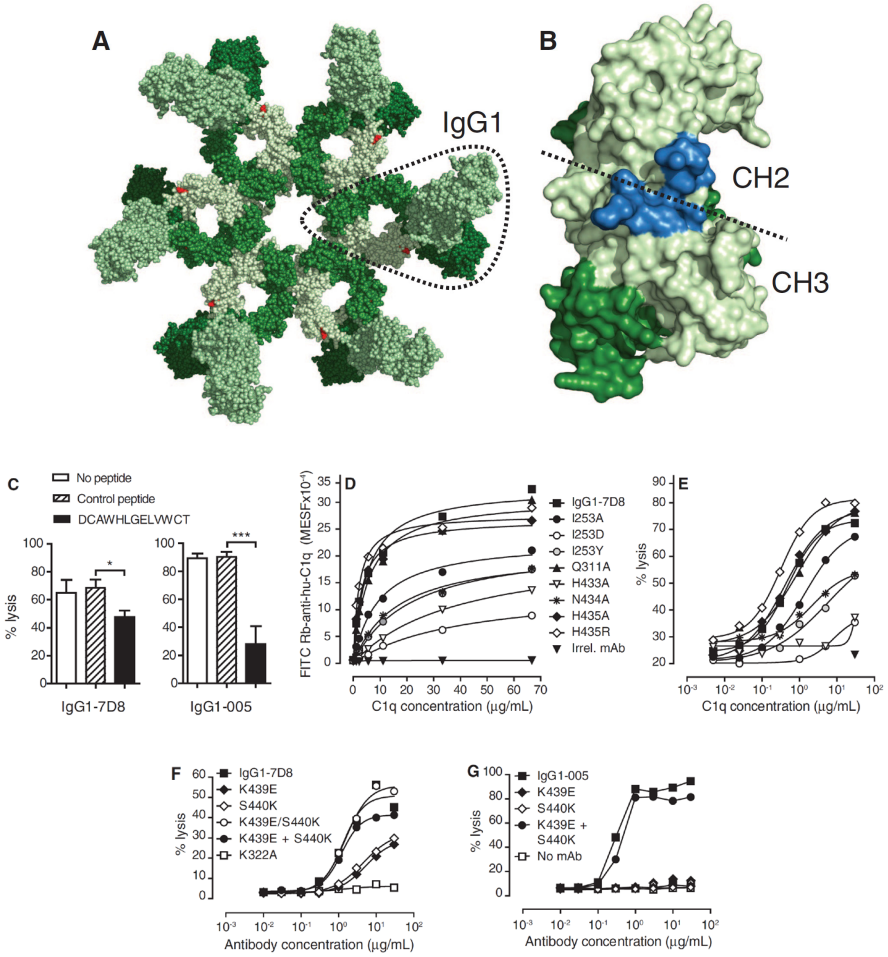

Fig. 1. C1q binding and complement activation by antibody hexamers. (A) IgG hexamer crystal packing of IgG1-b12 (1HZH). The dashed enclosure indicates a single IgG molecule. The C1q binding residue Lys322, located in the CH2 domain, is indicated in red. (B) Surface map depicting the Fc-Fc interface. Residues interacting with the Fc-binding peptide DCAWHLGELVWCT are indicated in blue. (C) The Fc-binding peptide inhibits CDC mediated by IgG1-7D8 (Raji cells) and IgG1-005 (Daudi cells). Data are average values T SD (N = 3); one-way analysis of variance followed by Dunnett's multiple comparison post hoc test: *P < 0.05,***P < 0.001. (D) C1q binding to CD20+ Raji cells opsonized with wild-type or mutated CD20 antibody IgG1-7D8. FITC, fluorescein isothiocyanate; MESF, molecules of equivalent soluble fluorochrome. A representative example is shown (N = 3). (E) CDC of Raji cells opsonized with wild-type and mutated IgG1-7D8. A representative example is shown (N = 3). The absence of CDC without added C1q indicates classical pathway activation. (F and G) CDC of K439E and S440K, abrogated in single point mutants, is restored in an IgG1-7D8 double mutant [(F), Raji cells] and by mixing single mutants of IgG1-7D8 (F) or IgG1-005 [(G), Daudi cells]. Representative examples are shown (N = 3). Amino acid abbreviations: A, Ala; C, Cys; D, Asp; E, Glu; G, Gly; H, His; I, Ile; K, Lys; L, Leu; N, Asn; Q, Gln; R, Arg; S, Ser; T, Thr; V, Val; W, Trp; Y, Tyr.

complement activation and CDC, consistent with other mutations in the Fc-Fc interface (Fig. 1E, fig. S2A, and table S2). Modeling suggested that Lys^{439} and Ser^{440} could be manipulated to test Fc-Fc interactions in a gain-of-function experiment (fig. S2B). In isolation, charge repulsion in mutants K439E (Lys^{439} → Glu) and S440K (Ser^{440} → Lys), indeed, inhibited CDC; this inhibition could be overcome with double mutants or mixtures containing both mutants that neutralized this repulsion (Fig. 1, F and G, and tables S1 and S2). We also identified mutations that resulted in significantly enhanced CDC, as exemplified by E345R (Glu^{345} → Arg), which increased C1q avidity to opsonized cells by a factor of ~5 and CDC by a factor of ~10 when introduced into CD20 antibody IgG1-7D8 (Fig. 2A and tables S1 and S2) (*20*). Similarly, the E345R substitution increased CDC of CD38 antibody IgG1-005 (Fig. 2B) as well as of its IgG2, IgG3, and IgG4 isotype variants (Fig. 2C). A triple mutant, IgG1-005-RGY, combining E345R with two additional enhancing mutations [E430G (Glu^{430} → Gly) and S440Y (Ser^{440} → Tyr)] readily formed hexamers in solution. The presence of monomeric and hexameric species of IgG1-005-RGY, presumably in equilibrium, was demonstrated by native mass spectrometry (Fig. 3A and table S3), high-performance size exclusion chromatography (HP-SEC) combined with multiangle static light scattering (MALS) (Fig. 3B), and negative-stain electron tomography (ET) (Fig. 3, C to F). Solution-phase hexamers of IgG1-005-RGY directly activated complement when added to human serum, as shown by the generation of C4d (Fig. 2D). This was also observed for IgG1-7D8-RGY, a triple mutant of the CD20 antibody. Together, these findings directly link a biophysically characterized noncovalent IgG1 hexamer with classical pathway complement activation. Finally, IgG1-005-RGY showed a further potency increase when bound to cells, as shown by stronger CDC at low concentrations relative to the single mutant (Fig. 2E), which may be explained by preformed hexamers or enhanced Fc-Fc–mediated assembly on the

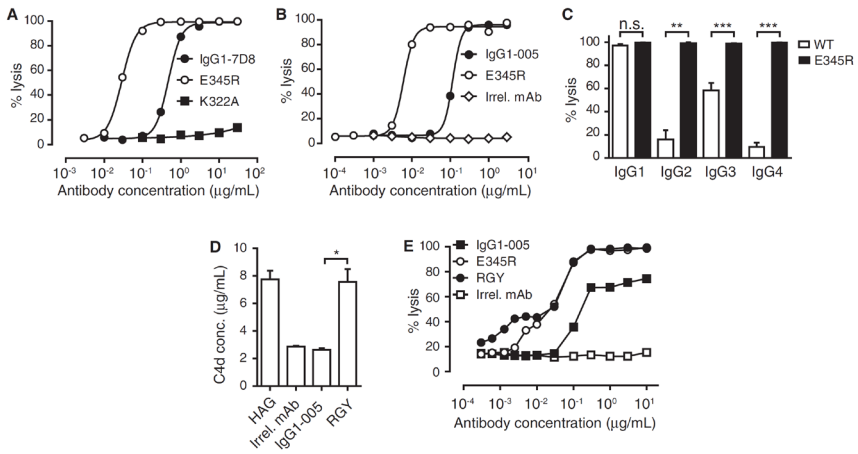

Fig. 2. Increased CDC by enhanced hexamer formation. (A and B) Increased CDC of Daudi cells by IgG1-7D8-E345R (A) and IgG1-005-E345R (B) relative to wild-type antibodies. Representative examples are shown (N = 4). (C) E345R mutants of IgG1-005 isotype variants induce CDC of Daudi cells more potently than wild-type (WT) IgG2, IgG3, and IgG4; IgGs were tested at 10 mg/ml. Data are average values T SD (N = 3); two-sided unpaired *t*-test with Welch's correction: n.s., not significant; **P < 0.01, ***P < 0.001. (D) IgG1-005-RGY induced C4d generation in normal human serum. Data are average values T SD (N = 3). Two-sided unpaired t test with Welch's correction; *P < 0.05. Heat-aggregated IgG (HAG) was used as a positive control. (E) IgG1-005-RGY showed enhanced CDC activity of Ramos cells relative to wild-type IgG1-005 and IgG1-005-E345R. A representative example is shown (N = 3).

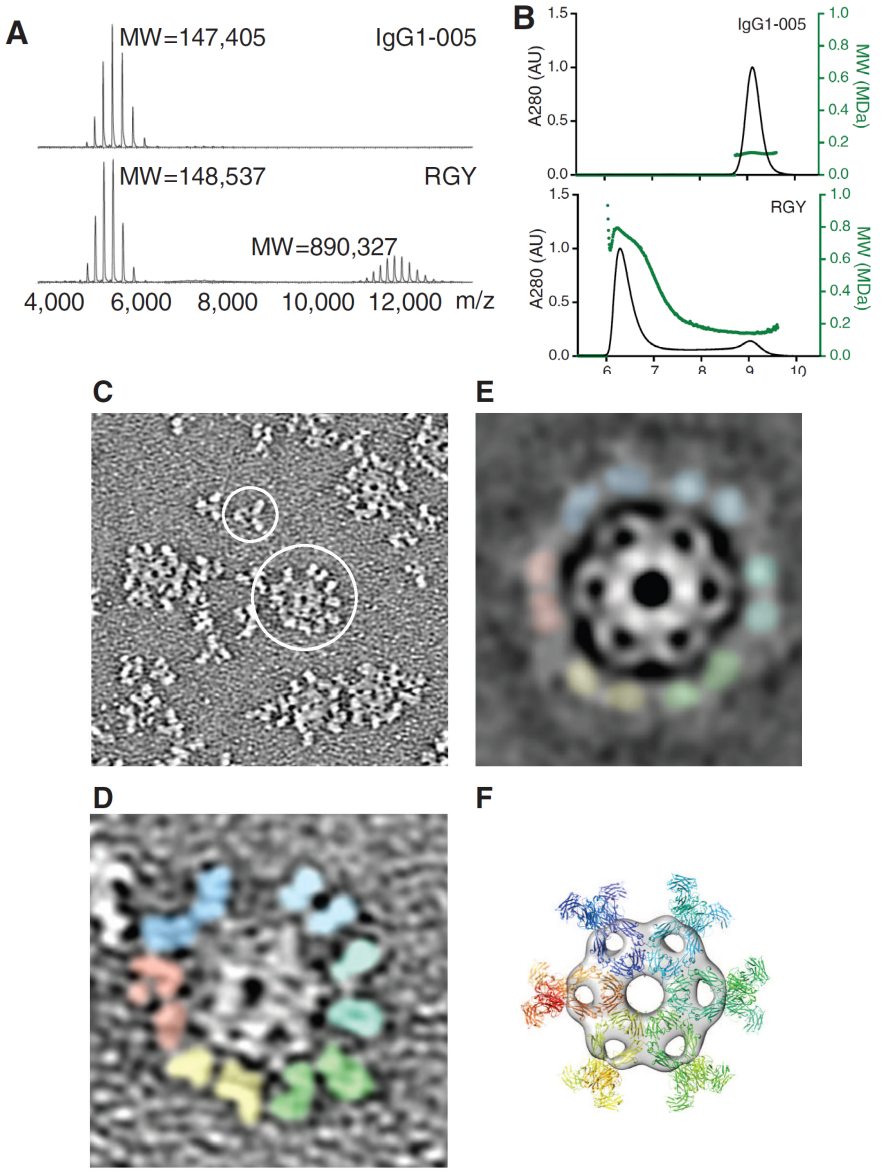

Fig. 3. Solution-phase hexamers formed by triple mutant IgG1-005-RGY. (A) Native mass spectrometry of IgG1-005 indicating a molecular weight (MW) of 147,405 daltons and IgG1-005-RGY showing MWs of a monomer (148,537 daltons) and a hexamer (890,327 daltons) (table S3). The hexameric state was confirmed in experiments using different conditions (N = 6); m/z, mass/charge ratio. (B) Overlay of HP-SEC–MALS profiles [absorbance at 280 nm (A280), black, left axis; MW, green, right axis] of IgG1-005 (top) and IgG1-005-RGY (bottom) shows that ~79% IgG1- 005-RGY eluted as hexamer and ~21% as monomer, whereas >99% of IgG1-005 eluted as monomer. A representative example is shown (N = 3). (C to F) ET of negatively stained IgG1-005-RGY (C) ET overview image showing a monomer (small circle) and a hexamer (large circle). (D) Representative hexamer with colored Fab pairs. (E) ET average of 200 subtomograms at a resolution of 2.9 nm. (F) Surface rendering of a symmetrized Fc ring withdocked 1HZH hexamer.

cell surface.

To image C1 binding to antigen-bound IgG on a membrane, we performed cryo-electron tomography (cryo-ET) using dinitrophenyl (DNP)-labeled liposomes (*20*). In the cryo-ET reconstructions, antibodies on the liposome surface assembled in single-layer patches with maximum density at a distance of 11 nm from the membrane (fig. S3, A and E) (*20*). Addition of purified C1 protein, C4-depleted serum, or normal human serum resulted in C1 binding on top of the antibody layer (fig. S3, F to H). Cryo-ET tomograms of 107 particles representing antibody-C1 complexes were averaged (fig. S4), resulting in an electron density map at low (>6 nm) resolution. The map showed a lower platform at 11 nm (coinciding with the maximum density observed on liposomes with antibody alone), a second platform at 20 nm, and a stalk on top of the upper platform (Fig. 4A). Horizontal sections through the tomogram average indicated that the lower platform was composed of a continuous disk with six poorly resolved densities protruding toward the membrane and four discernible densities on top, arranged as an incomplete hexagon (Fig. 4, B to E). We generated a model of the C1-antibody complex by docking the 1HZH crystal packing [adapted by Fab rotation (fig. S5)] into the lower platform and manually fitting C1q headpieces (Fig. 4F and fig. S6) (*20*). The four densities on top of the lower platform suggested incomplete (4:6) C1q headpiece binding to the antibody hexamer (Fig. 4C) and may reflect flexibility and dynamics of the C1q-IgG interactions. The model suggested that one Fab arm of each antibody in the hexamer bound the membrane-associated antigen while the other Fab arm was positioned at the height of the platform (Fig. 4F). To test the concept that complement activation might only require monovalent binding, we generated functionally monovalent bispecific antibodies (*20*, *21*) that contained one specific and one innocuous Fab arm (i.e., IgG1-7D8/b12 and IgG1-2F8/b12, monovalently binding CD20 and EGFR, respectively). Both antibodies induced efficient CDC of relevant target cells (Fig. 4, G and H), which for the bispecific antibody 2F8/b12 was strongly enhanced relative to the parental 2F8 antibody. Thus, for this antibody-antigen pair, monovalent binding is better able than (high-affinity) bivalent binding to accommodate the Fc-Fc hexamerization required for efficient CDC. The hexameric IgG-C1 binding model (Fig. 4, A and F, and fig. S6) revealed geometrical restraints that could explain the strong antigen and epitope dependency of complement activation. Potent complement activation by monoclonal antibodies is restricted to certain antigens and epitopes (*12*, *19*, *22*), presumably because antigen size, density, and fluidity may affect activation (*18*, *22*–*26*) and because IgG orientation resulting from epitope geometry imposes additional structural constraints (*12*, *19*, *22*, *25*, *27*). Polyclonal antibodies appear to be less sensitive than monoclonal antibodies to such constraints (*24*, *28*, *29*), potentially because binding of antibodies to a variety of antigens or epitopes facilitates clustering of Fc segments, thereby allowing efficient Fc-Fc assembly. Monovalent binding of IgG molecules in the platform is consistent with earlier observations (*30*) and could be envisaged to provide more degrees of freedom for the Fc segments, allowing their optimal positioning for C1q recruitment.

Our model is in agreement with an evolutionary relationship between IgM and IgG in triggering complement (*11*). IgM normally exists in a polymeric state, in which C1q binding sites are sequestered and only become exposed when antigen is bound (*6*, *31*), whereas IgG normally exists in a monomeric state in which C1q binding sites are exposed but affinity is too low to allow adequate C1 binding. In our model, sequential antigen and Fc-Fc binding by IgG leads to the formation of hexamers that bind C1q with high avidity and activate complement. The model is nonetheless

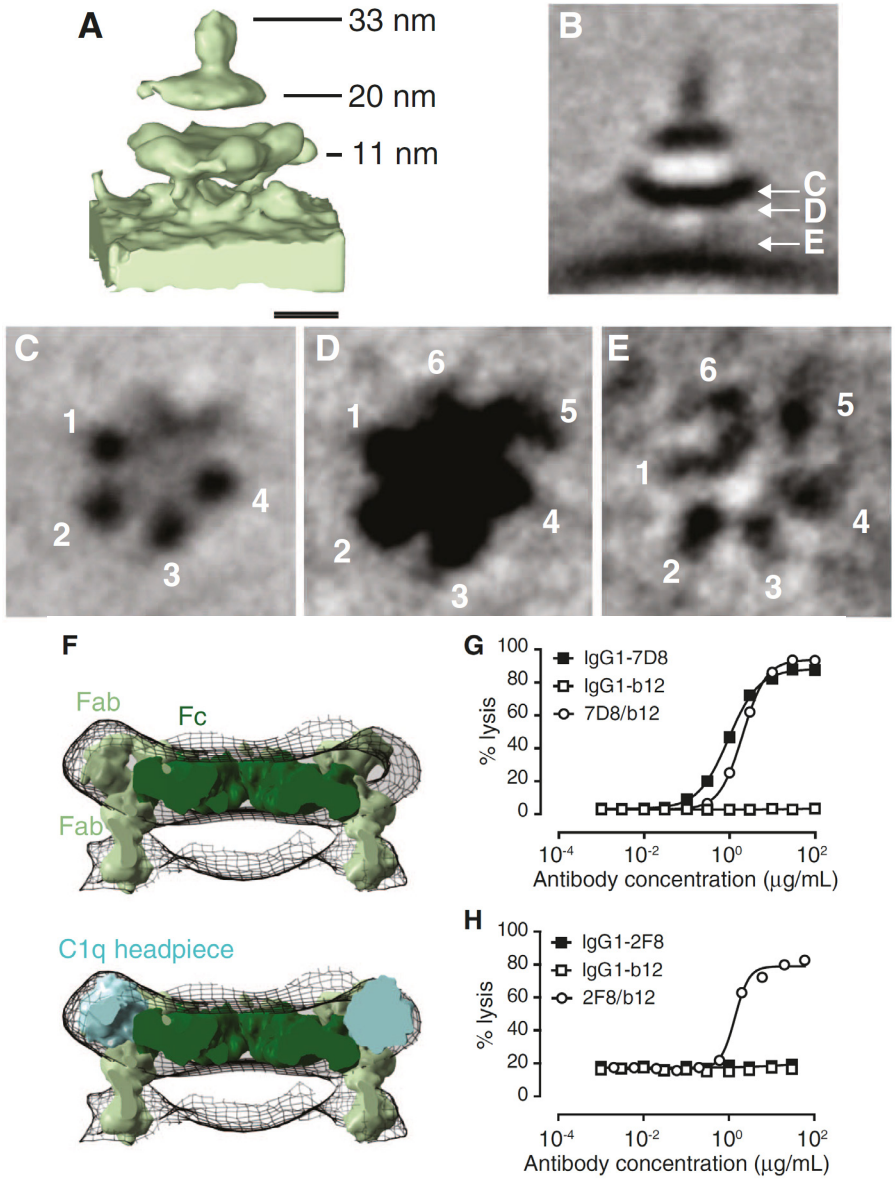

Fig. 4. Visualization of antibody-C1 complexes on antigen-coated liposomes. (A) Subtomogram average of antibody-C1 at >6 nm resolution shown as an isosurface. Heights indicate distances to the membrane center. (B) Vertical section through cryo-ET average. White arrows indicate the positions of sections shown in (C) to (E). (C) Top horizontal section showing four putative C1q globular headpieces. (D) Center section showing a dense hexagonal platform. (E) Bottom section showing six putative antigen-binding Fab arms. (F) Side view of the IgG1-b12–based hexamer model placed into the six-fold symmetrized density of the lower cryo-ET platform (top) and hexamer model with docked C1q headpieces (bottom). (G) CDC of CD20+ Raji cells by (functionally monovalent) bispecific antibody IgG1-7D8/b12. A representative example is shown (N = 3). (H) CDC of EGFR+ A431 cells by (functionally monovalent) bispecific antibody IgG1-2F8/b12. A representative example is shown (N = 4). IgG1-b12 against HIV-1 gp120 contributed the innocuous Fab arm.

compatible with observations that smaller IgG complexes may suffice to initiate some complement activation (*8*, *32*). However, low-avidity C1q binding will result in only modest complement activity (*27*), whereas the IgG hexamer will bind C1q most avidly, thus ensuring optimal complement activation when required. The observation that IgG hexamerization after antigen binding leads to effective complement activation could be exploited by increasing Fc-Fc contact formation. Because the E345R mutation bestowed complement-activating capability on all human IgG subclasses, IgG hexamerization may be a general concept applicable to the engineering of therapeutic antibodies with enhanced activity.

REFERENCES

1. D. Ricklin, G. Hajishengallis, K. Yang, J. D. Lambris, Complement: A key system for immune surveillance and homeostasis. *Nat. Immunol.* **11**, 785–797 (2010).
2. J. R. Dunkelberger, W. C. Song, Complement and its role in innate and adaptive immune responses. *Cell Res.* **20**, 34–50 (2010).
3. C. Gaboriaud, N. M. Thielens, L. A. Gregory, V. Rossi, J. C. Fontecilla-Camps, G. J. Arlaud, Structure and activation of the C1 complex of complement: Unraveling the puzzle. *Trends Immunol.* **25**, 368–373 (2004).
4. U. Kishore, K. B. Reid, C1q: Structure, function, and receptors. *Immunopharmacology* **49**, 159–170 (2000).
5. N. C. Hughes-Jones, B. Gardner, Reaction between the isolated globular sub-units of the complement component C1q and IgG-complexes. *Mol. Immunol.* **16**, 697–701 (1979).
6. A. Feinstein, N. Richardson, M. J. Taussig, Immunoglobulin flexibility in complement activation. *Immunol. Today* **7**, 169–174 (1986).
7. D. R. Burton, Immunoglobulin G: Functional sites. *Mol. Immunol.* **22,** 161–206 (1985).
8. T. Borsos, H. J. Rapp, Complement fixation on cell surfaces by 19S and 7S antibodies. *Science* **150**, 505–506 (1965).
9. W. F. Rosse, Quantitative immunology of immune hemolytic anemia. I. The fixation of C1 by autoimmune antibody and heterologous anti-IgG antibody. *J. Clin. Invest.* **50**, 727–733 (1971).
10. J. J. Thompson, L. G. Hoffman, Cooperative binding of a complement component to antigenantibody complexes. II. Effect of variations in temperature and ionic strength. *Immunochemistry* **11**, 537–541 (1974).
11. D. R. Burton, Is IgM-like dislocation a common feature of antibody function? *Immunol. Today* **7**, 165–167 (1986).
12. C. I. Bindon, G. Hale, H. Waldmann, Importance of antigen specificity for complementmediated lysis by monoclonal antibodies. *Eur. J. Immunol.* **18**, 1507–1514 (1988).
13. D. R. Burton, Antibody: The flexible adaptor molecule. *Trends Biochem. Sci.* **15**, 64–69 (1990).
14. E. O. Saphire, P. W. H. I. Parren, C. F. Barbas 3rd, D. R. Burton, I. A. Wilson, Crystallization and preliminary structure determination of an intact human immunoglobulin, b12: An antibody that broadly neutralizes primary isolates of HIV-1. *Acta Crystallogr. D* **57**, 168–171 (2001).

15. E. O. Saphire, P. W. Parren, R. Pantophlet, M. B. Zwick, G. M. Morris, P. M. Rudd, R. A. Dwek, R. L. Stanfield, D. R. Burton, I. A. Wilson, Crystal structure of a neutralizing human IGG against HIV-1: A template for vaccine design. *Science* **293**, 1155–1159 (2001).
16. Y. Wu, A. P. West Jr., H. J. Kim, M. E. Thornton, A. B. Ward, P. J. Bjorkman, Structural basis for enhanced HIV-1 neutralization by a dimeric immunoglobulin G form of the glycan-recognizing antibody 2G12. *Cell Rep.* **5**, 1443–1455 (2013).
17. W. L. DeLano, M. H. Ultsch, A. M. de Vos, J. A. Wells, Convergent solutions to binding at a protein-protein interface. *Science* **287**, 1279–1283 (2000).
18. J. L. Teeling, R. R. French, M. S. Cragg, J. van den Brakel, M. Pluyter, H. Huang, C. Chan, P. W. Parren, C. E. Hack, M. Dechant, T. Valerius, J. G. van de Winkel, M. J. Glennie, Characterization of new human CD20 monoclonal antibodies with potent cytolytic activity against non-Hodgkin lymphomas. *Blood* **104**, 1793–1800 (2004).
19. M. de Weers, Y. T. Tai, M. S. van der Veer, J. M. Bakker, T. Vink, D. C. Jacobs, L. A. Oomen, M. Peipp, T. Valerius, J. W. Slootstra, T. Mutis, W. K. Bleeker, K. C. Anderson, H. M. Lokhorst, J. G. van de Winkel, P. W. Parren, Daratumumab, a novel therapeutic human CD38 monoclonal antibody, induces killing of multiple myeloma and other hematological tumors. *J. Immunol.* **186**, 1840–1848 (2011).
20. See supplementary materials.
21. A. F. Labrijn, J. I. Meesters, B. E. de Goeij, E. T. van den Bremer, J. Neijssen, M. D. van Kampen, K. Strumane, S. Verploegen, A. Kundu, M. J. Gramer, P. H. van Berkel, J. G. van de Winkel, J. Schuurman, P. W. Parren, Efficient generation of stable bispecific IgG1 by controlled Fab-arm exchange. *Proc. Natl. Acad. Sci. U.S.A.* **110**, 5145–5150 (2013).
22. M. S. Cragg, S. M. Morgan, H. T. Chan, B. P. Morgan, A. V. Filatov, P. W. Johnson, R. R. French, M. J. Glennie, Complement-mediated lysis by anti-CD20 mAb correlates with segregation into lipid rafts. *Blood* **101**, 1045–1052 (2003).
23. J. W. Parce, D. Kelley, K. Heinzelmann, Measurement of antibody-dependent binding, proteolysis, and turnover of C1s on liposomal antigens localizes the fluidity-dependent step in C1 activation. *Biochim. Biophys. Acta* **736**, 92–98 (1983).
24. N. C. Hughes-Jones, B. D. Gorick, J. C. Howard, A. Feinstein, Antibody density on rat red cells determines the rate of activation of the complement component C1. *Eur. J. Immunol.* **15**, 976–980 (1985).
25. J. L. Teeling, W. J. Mackus, L. J. Wiegman, J. H. van den Brakel, S. A. Beers, R. R. French, T. van Meerten, S. Ebeling, T. Vink, J. W. Slootstra, P. W. Parren, M. J. Glennie, J. G. van de Winkel, The biological activity of human CD20 monoclonal antibodies is linked to unique epitopes on CD20. *J. Immunol.* **177**, 362–371 (2006).
26. M. Q. Xia, G. Hale, H. Waldmann, Efficient complement-mediated lysis of cells containing the CAMPATH-1 (CDw52) antigen. *Mol. Immunol.* **30**, 1089–1096 (1993).
27. A. W. Pawluczkowycz, F. J. Beurskens, P. V. Beum, M. A. Lindorfer, J. G. van de Winkel, P. W. Parren, R. P. Taylor, Binding of submaximal C1q promotes complement-dependent cytotoxicity (CDC) of B cells opsonized with anti-CD20 mAbs ofatumumab (OFA) or rituximab (RTX): Considerably higher levels of CDC are induced by OFA than by RTX. *J. Immunol.* **183**, 749–758 (2009).
28. M. Dechant, W. Weisner, S. Berger, M. Peipp, T. Beyer, T. Schneider-Merck, J. J. Lammerts van

Bueren, W. K. Bleeker, P. W. Parren, J. G. van de Winkel, T. Valerius, Complementdependent tumor cell lysis triggered by combinations of epidermal growth factor receptor antibodies. *Cancer Res.* **68**, 4998–5003 (2008).

29. F. Kushihata, J. Watanabe, A. Mulder, F. Claas, J. C. Scornik, Human leukocyte antigen antibodies and human complement activation: Role of IgG subclass, specificity, and cytotoxic potential. *Transplantation* **78**, 995–1001 (2004).
30. H. F. Watts, V. A. Anderson, V. M. Cole, G. T. Stevenson, Activation of complement pathways by univalent antibody derivatives with intact Fc zones. *Mol. Immunol.* **22**, 803– 810 (1985).
31. D. M. Czajkowsky, Z. Shao, The human IgM pentamer is a mushroom-shaped molecule with a flexural bias. *Proc. Natl. Acad. Sci. U.S.A.* **106**, 14960–14965 (2009).
32. W. F. Rosse, H. J. Rapp, T. Borsos, Structural characteristics of hemolytic antibodies as determined by the effects of ionizing radiation. *J. Immunol.* **98**, 1190–1195 (1967).

SUPPLEMENTAL MATERIALS AND METHODS

Visualization of antibody structure and modeling of mutants. Schematic views of the structure of human monoclonal antibody IgG1-b12 were generated from the 1HZH crystal structure using PyMOL version 1.5.0.4 (Schrödinger LLC). Mutant models were generated by selecting the rotamers closest to the original sidechain conformation using the mutagenesis module; no energy minimization was applied.

Construction, expression and purification of antibody variants. Human monoclonal antibodies IgG1-7D8 recognizing CD20 (*18*), IgG1-005 recognizing CD38 (*19*), IgG1-2F8 recognizing EGFR (*33*) and IgG1-b12 recognizing HIV-1 gp120 (*34*) were used as model antibodies with G1m(f) allotypes. Codon-optimized antibody genes (GeneArt, Germany) were cloned in pConG1f (Lonza) for 7D8 heavy chain variants, pConKappa (Lonza) for the 7D8 light chain, and pcDNA3.3 (Invitrogen) for heavy and light chain variants of 005, 2F8 and b12. Isotype variants were generated as described previously (*35*). Isotypic variants were based on human IgG2 (Uniprot entry P01859), IgG3 (P01860) and IgG4 (P01861). Mutations were introduced in heavy chain expression vectors using Quikchange technology (Agilent Technologies, US) at positions numbered according to Eu nomenclature. Antibodies were expressed in HEK293 FreeStyle cells by transfection of light chain and heavy chain expression vector DNA using 293fectin essentially as described by the manufacturer (Invitrogen, US). Antibodies were purified by Protein A affinity chromatography (rProtein A FF; GE Healthcare), dialyzed overnight against PBS, and filter-sterilized over 0.2-µM dead-end filters. Concentration of purified IgGs was determined by absorbance at 280 nm. Quality assessment of purified antibodies was performed by SDS/PAGE, mass spectrometry, and HP-SEC. Bispecific molecules were generated by controlled Fab arm exchange of the purified homodimeric components in the presence of 25 mM 2-MEA as described (*21*). The functionally monovalent bispecific antibodies directed against CD20 and the, for this experiment, innocuous antigen HIV1 gp120 (IgG1-7D8/b12) or against EGFR and HIV-1 gp120 (IgG1-2F8/b12), were generated by controlled Fab arm exchange of IgG1-b12-F405L with IgG1-7D8-K409R and with IgG1-2F8K409R, respectively.

Cell culture and reagents. A431 cells (human epidermoid cell line) were obtained from the Deutsche Sammlung von Mikroorganismen und Zellkulturen (cell line number ACC 91; Braunschweig, Germany). Daudi, Raji and Ramos cells (human Burkitt's lymphoma) were obtained from the American Type Culture Collection (ATCC no. CCL-213, CLL-86 and CRL-1596 respectively; Rockville, MD). HEK293 FreeStyle cells were obtained from Invitrogen (Paisley, UK). All cell lines were routinely tested for mycoplasma contamination and generally aliquoted and banked to allow in vitro assays to be performed from frozen cell stocks and not from continuous cultures to ensure authenticity of the cells. Pooled normal human serum (NHS) AB was obtained from Sanquin (The Netherlands), C1q-depleted serum from Quidel (San Diego, CA) and C4-depleted serum from Complement Technology Inc. (Tyler TX). Purified C1 was provided by M. Daha (Leiden University Medical Center, Leiden, the Netherlands) and C1q was purchased from Complement Technology Inc. The Fc binding peptide DCAWHLGELVWCT (*17*) and control peptide GWTVFQKRLDGSV were synthesized by Pepscan Presto B.V. (Lelystad, The Netherlands).

Determination of C1q binding to antibody-opsonized cells. Determinations of C1q binding to B cells pre-reacted with CD20 antibodies was performed as described previously (*27*).

CDC assays. CDC assays were performed as described (*27*), either with a fixed antibody concentration of 10 µg/mL in C1q-deficient serum supplemented with a concentration series of C1q, or with an antibody concentration series or a fixed antibody concentration and normal human serum (20% final concentration) as a source of complement. Killing was calculated as the % PI+ cells determined by a BD FACSCanto II flow cytometer for Daudi, Raji and Ramos B cells, and as % TOPRO-iodide+ cells determined by a Celigo imaging cytometer (Brooks Life Science Systems) for A431 carcinoma cells.

CDC assay with Fc-binding peptide or irrelevant peptide. Raji or Daudi cells were incubated with a fixed concentration of IgG1-7D8 (6 µg/mL) or IgG1-005 (0.8 µg/mL), respectively and the Fc binding peptide DCAWHLGELVWCT or control peptide GWTVFQKRLDGSV at a final concentration of 60 µg/mL with normal human serum (20% final concentration) as a source of complement. Killing was calculated as the % PI+ cells determined by a BD FACSCanto II flow cytometer.

Solution-phase complement activation assay. Complement activation in the absence of target was determined by measuring C4d concentrations, a marker for classical pathway complement activation, after incubating 100 µg antibody in 1 mL 90% normal human serum for 1 hour at 37ºC. C4d concentrations were measured in an ELISA (MicroVue C4d EIA kit, Quidel Corporation, San Diego, US) according to the manufacturer's instructions.

HP-SEC analysis. HP-SEC fractionation was performed using a Waters Alliance 2975 separation unit (Waters, Etten-Leur, The Netherlands) connected to a TSK HP-SEC column (G3000SW$_{xl}$; Toso Biosciences, via Omnilabo, Breda, The Netherlands), a Waters 2487 dual λ absorbance detector (Waters), and a Mini Dawn Treos MALS detection unit (Wyatt). 50 µL samples containing 1.25 µg/mL protein were separated at 1 mL/min in 0.1 M Na_2SO_4 /0.1 M sodium phosphate buffered at pH 6.8. Results were processed using Empower software version 2002 and expressed per peak as percentage of total peak area.

Native mass spectrometry. IgG1 oligomerization was studied by native mass spectrometry as described previously (*36*). The constructs were analyzed in 0.05 M ammonium acetate (pH 7.0) at an antibody concentration of 5 µM. This protein preparation was obtained by five sequential concentration and dilution steps at 4ºC using a centrifugal filter with a cut-off of 10 kDa (Millipore). Samples were sprayed from borosilicate glass capillaries and analyzed on a modified quadrupole time-of-flight instruments (Waters, UK) adjusted for optimal performance in high mass detection (*37*, *38*). Instrument settings were as follows; needle voltage ~1.4 kV, cone voltage ~150 V, source pressure 9 mbar. Extent of oligomerization was estimated by summing the areas under the curves. We analyzed wild type IgG1-005 and triple mutant IgG1-005-RGY in parallel. Peak intensities may have been affected by ionization and transmission efficiency of the different protein species and therefore did not directly represent relative abundance.

Negative stain electron microscopy. 4 µL of IgG1-005-RGY (30 µg/mL) was applied to a glow discharged EM grid with continuous carbon film and stained with 3% uranyl-acetate solution as described previously (*39*). Electron tomograms were acquired using a Tecnai F20 (FEI) electron microscope, equipped with FEI 4k x 4k Eagle CCD camera at 200 kV. 50,000 x magnification resulting in a pixel size of 4.4 Å at specimen level and a nominal defocus of -1 µm were applied. Tomograms were reconstructed and visualized in IMOD (*40*, *41*) after low-pass filtering to the first zero of the CTF (~2 nm). 237 subtomograms of hexamers were boxed for averaging in PEET (*42*). The final average comprising 200 particles had a resolution of 2.9 nm according to the 0.5 FSC criterion.

Sample preparation for cryo-electron tomography. Incubations of DNP-labeled liposomes and anti-DNP antibody (Wako Diagnostics, Richmond, VA) with purified C1, C4-depleted human serum and normal human serum were performed as described previously for liposome immune assays for measuring total complement activity of reconstituted complexes (*43*). Purified bovine C1 was provided by Dr. M. Daha. Samples for cryo-ET were prepared by plunge freezing. EM grids, R1.2 1.3, Cu, 200 mesh (Quantifoil), were glow discharged for 1 min at 30 mA and negative polarity using a K950X carbon coater (Emitech). Protein conjugated 6 nm gold particles (Aurion) were added as fiducial markers. Grids were blotted 3 s with filter paper (Whatman 541) and vitrified in a propane/ethane (2:1 v/v) mixture using a EM GP (Leica) at 95% humidity at room temperature.

Single and dual axis cryo-electron tomography. Single axis cryo-electron tomography tilt series were acquired using Gatan 626 or Gatan 914 high-tilt cryo-holders on a Tecnai F20 (FEI), equipped with FEI 4k x 4k Eagle CCD camera and a GIF (Gatan) operated at 200 kV. Low-dose tilt series comprising 51 images were acquired in a range of +/- 60° in continuous Saxton tilt scheme at an initial increment of 3°, using tiltangle dependent exposure times. Initial microscope magnification of 29,000 x using a 2x binned 4k x 4k FEI Eagle CCD camera resulted in a pixel size of 7.6 Å at specimen level. The total dose was 10,000 e^-/nm^2 or ~5,100 e^-/nm^2 per tilt series. Auto focusing was performed every second tilt angle at ~ 5 micron distance. Tilt series were taken at -5 to -7.5 micron defocus resulting in a first zero of the contrast transfer function (CTF) between 3.5 nm and 4.3 nm. Dual-axis tilt series were acquired in a similar manner using a FEI Titan Krios at 200 kV acceleration voltage and parallel illumination with a GATAN Quantum imaging filter. The total electron dose was 10,000 e^-/nm^2 per dual-tilt series.

Image processing. Cryo-electron tomograms were reconstructed using IMOD version 4.5.3 (*40*, *41*). The defocus was measured using TOMOCTF (version Dec 2009 (*44*)) and CTF correction was applied by phase flipping in IMOD. 3D volumes were reconstructed applying five iterations of SIRT (*45*), while applying a low pass filter to ~1.3 nm resolution. Dual axis data sets were combined using manually pre-aligned reference points in separately reconstructed single tilt tomograms (*41*). PEET (*42*) was used for subtomogram averaging. Binary particle masks were created in SPIDER (*46*). 230 particles were pre-aligned using the PEET program stalkInit. The average of pre-oriented particles was used as an initial reference for alignments. Principle component analysis and k-means clustering for classification were performed on 200 the best particles (*47*). The three main structure factors were used for separation into seven clusters (fig. S4B). The main class of 111 particles contained 107

particles obtained from tomograms of C4-depleted serum, which were used for final analysis (fig. S4D). After symmetrization in IMOD and volume estimation using VADAR (*48*), atomic structures for IgG1-b12 antibody (1HZH (*15*)), globular head domains of C1q (1PK6 (*49*)), collagen (1CGD (*50*)) and C1rs (1NZI (*51*); 3DEM (*52*); 3POB (*53*)) were docked into the EM map by hand and refined using SITUS collage (*54*, *55*). IMOD and UCSF Chimera (*56*) were used for visualization.

Adaptation of the 1HZH hexamer structure for docking. To dock the 1HZH crystal packing arrangement in the lower platform of the cryo-ET density map, we adapted the alternating up-down pattern of Fab arms in neighboring antibodies (fig. S5A). Orienting all six axial Fab segments downwards left the central hexameric Fc ring unchanged (fig. S5, B and D) and fitted the IgG model in the observed lower platform by creating a table-like arrangement with Fc segments and six Fab arms equatorial and six Fab arms pointing downwards (Fig. 4F, fig. S5C).

Modeling of the antibody-C1 complex. The ~6 nm resolution was too low for direct automated docking of high-resolution crystal structures. Initial manual placement of components (hexameric Fc ring, 12 Fabs, six C1q headpieces and collagen stalks, and a premodelled $C1r_2s_2$ platform) was guided by structural details and orthogonal biochemical data that were available. Comparison of a number of simulations (fig. S4, H and I) indicated that the lower platform was best modeled by the hexameric IgG ring with incomplete binding of four C1q headpieces, accounting for the four discernible densities on top of this platform (Fig. 4C, fig. S4I). Positioning the C1q headpieces on the rim of the Fc ring was consistent with independent computational modeling of Fc-C1q headpieces based on available mutagenesis data (*57*).To prepare a model of the complete C1-antibody complex, we applied six-fold symmetry to fill in the two missing C1q headpieces (fig. S4, fig. S6). Keeping the hexameric Fc ring fixed, we manually fitted six globular C1q headpieces, each associated sideways with an equatorial Fab into the main globular densities of the lower platform. In this model, C1q contacted the Fc segment in a manner that was consistent with binding of the globular head to the C_H2 domain of IgG as previously proposed (*57*). For each IgG, one Fab arm was bound to the surface antigen DNP, whereas the other Fab and Fc interacted with C1q (fig. S6C). From the non-symmetrized average density of the C1-antibody complex, four of these interactions could be readily discerned, whereas disorder was apparent at the remaining two positions (Fig. 4C; fig. S4I). The manual placement of the individual atomic models was improved from 7.4% correlation to a converged value of 13.3% after 10 rounds of Powell optimization using Situs collage (*54*, *55*). The six globular and trimeric C1q headpieces are connected to each other through collagenous triple-helices that form a bundle at the N-terminus (*49*, *58*). While the 14-nm long collagenous stems were not resolved in the averaged map, density was observed for the 10nm bundle on top of the upper platform (Fig. 4, A and B). We modeled the stems as direct connections between the density of the bundle to the center of the globular densities of the lower platform; this resulted in an angle of 40° between the bundle and the stems (fig. S6E), which was in agreement with neutron scattering of C1q (*59*). To model the proteases C1r and C1s, we applied two-fold symmetry to the upper platform corresponding to their presumed heterotetrameric arrangement. The N-terminal domains were inserted in a planar arrangement, with the proposed collagen-binding sites on C1r and C1s in close proximity to the six collagen stems (fig. S6, D and E), consistent with Bally et al. (*60*) and Phillips et al. (*61*). We did not observe any density for the C-terminal domains of C1r and C1s. Presumably,

flexibility of the linker domains connecting the serine protease domains to the N-terminal base (*62*) resulted in absence of density.

SUPPLEMANTAL REFERENCES

33. J. J. Lammerts van Bueren, W. K. Bleeker, H. O. Bøgh, M. Houtkamp, J. Schuurman, J. G. van de Winkel, P. W. Parren, Effect of target dynamics on pharmacokinetics of a novel therapeutic antibody against the epidermal growth factor receptor: Implications for the mechanisms of action. *Cancer Res.* **66**, 7630–7638 (2006).
34. D. R. Burton, J. Pyati, R. Koduri, S. Sharp, G. Thornton, P. Parren, L. Sawyer, R. Hendry, N. Dunlop, P. Nara, Efficient neutralization of primary isolates of HIV-1 by a recombinant human monoclonal antibody. *Science* **266**, 1024–1027 (1994).
35. M. B. Overdijk, S. Verploegen, A. Ortiz Buijsse, T. Vink, J. H. Leusen, W. K. Bleeker, P. W. Parren, Crosstalk between human IgG isotypes and murine effector cells. *J. Immunol.* **189**, 3430–3438 (2012).
36. R. J. Rose, A. F. Labrijn, E. T. van den Bremer, S. Loverix, I. Lasters, P. H. van Berkel, J. G. van de Winkel, J. Schuurman, P. W. Parren, A. J. Heck, Quantitative analysis of the interaction strength and dynamics of human IgG4 half molecules by native mass spectrometry. *Structure* **19**, 1274–1282 (2011).
37. N. Tahallah, M. Pinkse, C. S. Maier, A. J. Heck, The effect of the source pressure on the abundance of ions of noncovalent protein assemblies in an electrospray ionization orthogonal time-of-flight instrument. Rapid Commun. *Mass Spectrom.* **15**, 596–601 (2001).
38. R. H. van den Heuvel, E. van Duijn, H. Mazon, S. A. Synowsky, K. Lorenzen, C. Versluis, S. J. Brouns, D. Langridge, J. van der Oost, J. Hoyes, A. J. Heck, Improving the performance of a quadrupole time-of-flight instrument for macromolecular mass spectrometry. *Anal. Chem.* **78**, 7473–7483 (2006).
39. J. R. Harris, Negative staining of thinly spread biological samples. *Methods Mol. Biol.* **369**, 107–142 (2007).
40. J. R. Kremer, D. N. Mastronarde, J. R. McIntosh, Computer visualization of threedimensional image data using IMOD. *J. Struct. Biol.* **116**, 71–76 (1996).
41. D. N. Mastronarde, Dual-axis tomography: An approach with alignment methods that preserve resolution. *J. Struct. Biol.* **120**, 343–352 (1997).
42. D. Nicastro, C. Schwartz, J. Pierson, R. Gaudette, M. E. Porter, J. R. McIntosh, The molecular architecture of axonemes revealed by cryoelectron tomography. *Science* **313**, 944–948 (2006).
43. S. Yamamoto, K. Kubotsu, M. Kida, K. Kondo, S. Matsuura, S. Uchiyama, O. Yonekawa, T. Kanno, Automated homogeneous liposome-based assay system for total complement activity. *Clin. Chem.* **41**, 586–590 (1995).
44. J. J. Fernández, S. Li, R. A. Crowther, CTF determination and correction in electron cryotomography. *Ultramicroscopy* **106**, 587–596 (2006).
45. P. Gilbert, Iterative methods for the three-dimensional reconstruction of an object from

projections. *J. Theor. Biol.* **36**, 105–117 (1972).

46. J. Frank, M. Radermacher, P. Penczek, J. Zhu, Y. Li, M. Ladjadj, A. Leith, SPIDER and WEB: Processing and visualization of images in 3D electron microscopy and related fields. *J. Struct. Biol.* **116**, 190–199 (1996).
47. J. M. Heumann, A. Hoenger, D. N. Mastronarde, Clustering and variance maps for cryoelectron tomography using wedge-masked differences. *J. Struct. Biol.* **175**, 288–299 (2011).
48. L. Willard, A. Ranjan, H. Zhang, H. Monzavi, R. F. Boyko, B. D. Sykes, D. S. Wishart, VADAR: A web server for quantitative evaluation of protein structure quality. *Nucleic Acids Res.* **31**, 3316–3319 (2003).
49. C. Gaboriaud, J. Juanhuix, A. Gruez, M. Lacroix, C. Darnault, D. Pignol, D. Verger, J. C. Fontecilla-Camps, G. J. Arlaud, The crystal structure of the globular head of complement protein C1q provides a basis for its versatile recognition properties. *J. Biol. Chem.* **278**, 46974–46982 (2003).
50. J. Bella, B. Brodsky, H. M. Berman, Hydration structure of a collagen peptide. *Structure* **3**, 893–906 (1995).
51. L. A. Gregory, N. M. Thielens, G. J. Arlaud, J. C. Fontecilla-Camps, C. Gaboriaud, X-ray structure of the Ca2+-binding interaction domain of C1s. Insights into the assembly of the C1 complex of complement. *J. Biol. Chem.* **278**, 32157–32164 (2003).
52. F. Teillet, C. Gaboriaud, M. Lacroix, L. Martin, G. J. Arlaud, N. M. Thielens, Crystal structure of the CUB1-EGF-CUB2 domain of human MASP-1/3 and identification of its interaction sites with mannan-binding lectin and ficolins. *J. Biol. Chem.* **283**, 25715– 25724 (2008).
53. A. R. Gingras, U. V. Girija, A. H. Keeble, R. Panchal, D. A. Mitchell, P. C. Moody, R. Wallis, Structural basis of mannan-binding lectin recognition by its associated serine protease MASP-1: Implications for complement activation. *Structure* **19**, 1635–1643 (2011).
54. S. Birmanns, M. Rusu, W. Wriggers, Using Sculptor and Situs for simultaneous assembly of atomic components into low-resolution shapes. *J. Struct. Biol.* **173**, 428–435 (2011).
55. W. Wriggers, Using Situs for the integration of multi-resolution structures. *Biophys. Rev.* **2**, 21–27 (2010).
56. E. F. Pettersen, T. D. Goddard, C. C. Huang, G. S. Couch, D. M. Greenblatt, E. C. Meng, T. E. Ferrin, UCSF Chimera—a visualization system for exploratory research and analysis. *J. Comput. Chem.* **25**, 1605–1612 (2004).
57. S. Schneider, M. Zacharias, Atomic resolution model of the antibody Fc interaction with the complement C1q component. *Mol. Immunol.* **51**, 66–72 (2012).
58. B. Brodsky-Doyle, K. R. Leonard, K. B. Reid, Circular-dichroism and electron-microscopy studies of human subcomponent C1q before and after limited proteolysis by pepsin. *Biochem. J.* **159**, 279–286 (1976).
59. S. J. Perkins, Molecular modelling of human complement subcomponent C1q and its complex with C1r2C1s2 derived from neutron-scattering curves and hydrodynamic properties. *Biochem. J.* **228**, 13–26 (1985).
60. I. Bally, V. Rossi, T. Lunardi, N. M. Thielens, C. Gaboriaud, G. J. Arlaud, Identification of the C1q-binding sites of human C1r and C1s: A refined three-dimensional model of the C1 complex of complement. *J. Biol. Chem.* **284**, 19340–19348 (2009).

61. A. E. Phillips, J. Toth, A. W. Dodds, U. V. Girija, C. M. Furze, E. Pala, R. B. Sim, K. B. Reid, W. J. Schwaeble, R. Schmid, A. H. Keeble, R. Wallis, Analogous interactions in initiating complexes of the classical and lectin pathways of complement. *J. Immunol.* **182**, 7708–7717 (2009).

62. C. Gaboriaud, V. Rossi, I. Bally, G. J. Arlaud, J. C. Fontecilla-Camps, Crystal structure of the catalytic domain of human complement C1s: A serine protease with a handle. *EMBO J.* **19**, 1755–1765 (2000).

SUPPLEMENTAL FIGURES

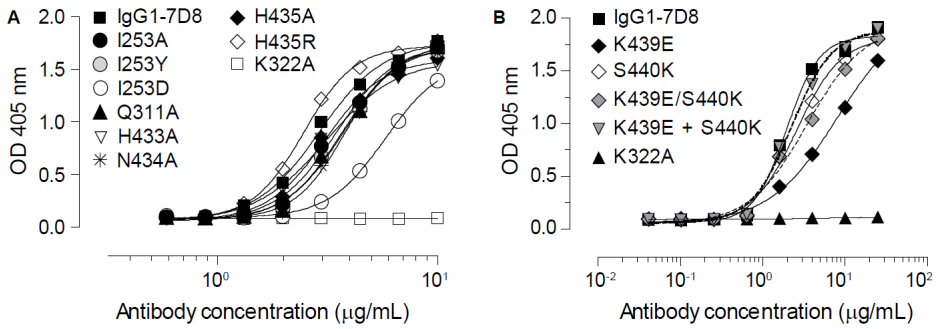

Fig. S1: C1 binding to immobilized IgG1-7D8 assessed by enzyme-linked immunosorbent assay (ELISA). Wild type IgG1-7D8 and IgG1-7D8 variants carrying amino acid mutations were randomly immobilized on microtiter plates. Binding of C1 captured from 3% pooled human serum and detected with rabbit anti-human C1q is shown. A K322A mutant abrogating C1 binding was used as a negative control. C1 binding was minimally (I253D and K439E) or not affected (all other mutants) as compared to wild type IgG1-7D8. (A) and (B) show a comparison of wild type IgG1-7D8 with a different set of mutants. Representative examples are shown (N=3).

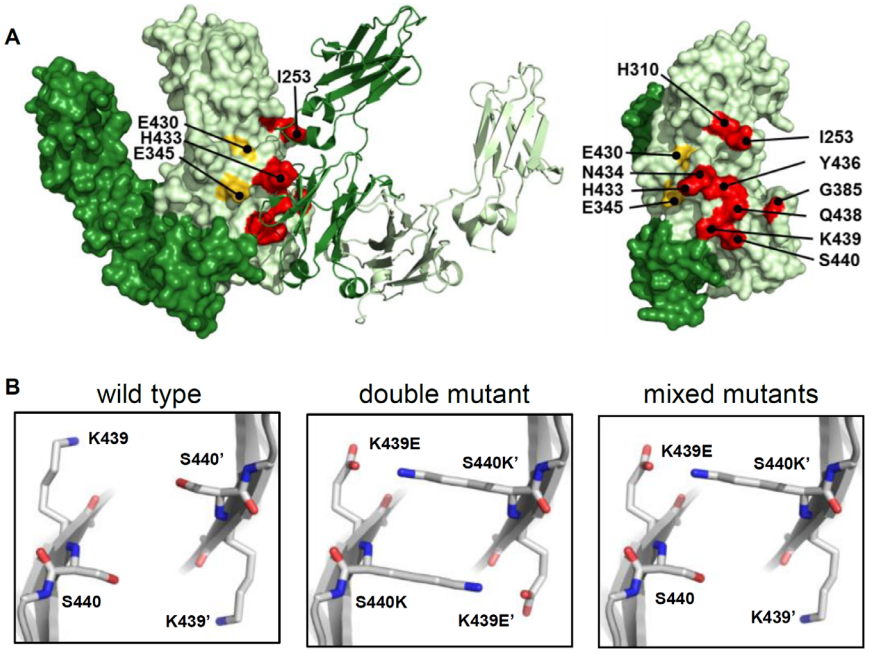

Fig. S2: Models indicating residues critical for Fc:Fc interactions. (A) Surface map of an IgG1 Fc segment and a ribbon cartoon representing a neighboring antibody Fc segment. Red and yellow indicate residues with mutations that decreased or enhanced complement activation respectively (Fig. 1, E,F and G; table S2). (B) Left: Detail from the hexamer structure 1HZH, which indicated that residue K439 faces residue S440 on the complementary Fc segment of a neighboring antibody. The middle and right panel show modeled interactions for a K439E/S440K double mutant and a mixture of K439E and S440K single mutants. The modeling suggested that the alignment of positive and negative charges between neighboring Fc segments would negate repulsion for the double mutant (middle) or the single mutant mixture (right).

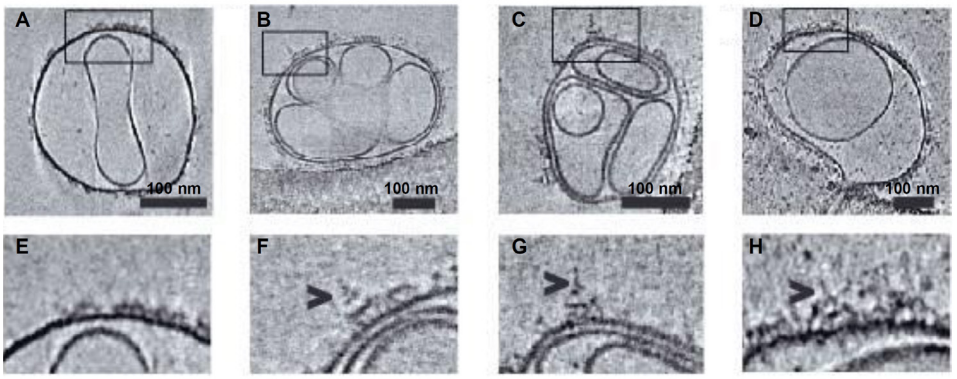

Fig. S3: Cryo-ET imaging of complement activation steps on DNP-labeled liposomes. Sections shown represent DNP-labeled liposomes incubated with: (A) anti-DNP antibody alone, (B) anti-DNP antibody and purified C1, (C) anti-DNP antibody and C4-depleted serum (complement activation arrests at C1), (D) anti-DNP antibody and normal human serum (resulting in a ~25-nm thick crowded layer covering the liposomes). (E to H) Represent enlargements of the areas indicated by a rectangle in the image above. Arrowheads point to antibody-C1 complexes with a height of ~ 33 nm.

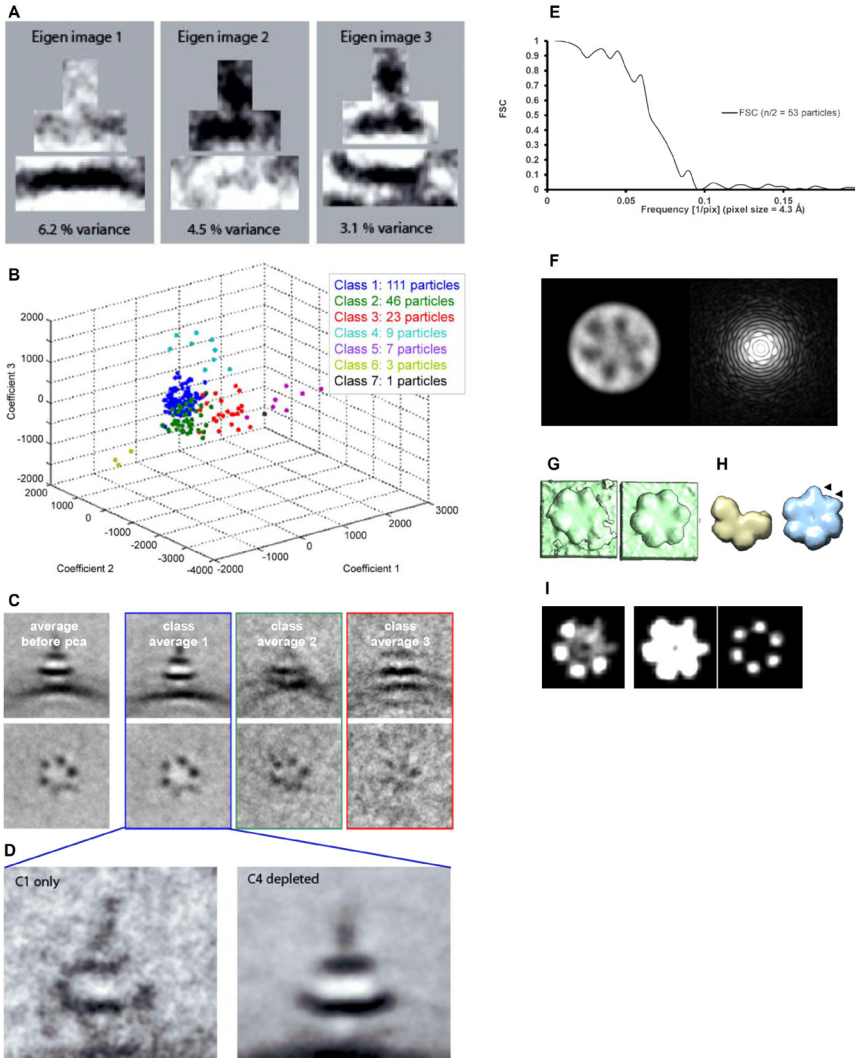

Fig. S4: Cryo-ET analyses. (A to D) Classification of subtomograms of C1 immune complexes by principle component analysis. (A) First three eigenimages accounting for 14% of variation within 200 subtomograms. (B) K-means clustering of seven classes (defined by the optimal Bayesian optimization criterion) using first three eigenvectors. (C) Vertical (top row) and horizontal (bottom row) sections through the non-classified average (left panel) and first three class averages (blue, green and red). (D) Sections through subclasses of class 1 (111 particles) originating from DNP-liposomes incubated with anti-DNP and C1 (4 particles; left panel), or anti-DNP and C4-depleted serum (107 particles; right panel). The subclass average of these latter 107 particles was used for symmetrization, docking and resolution measurement (20). (E) Fourier Shell correlation curve of an even-odd split data set, indicating a resolution of 5 nm or 6.6 nm with 0.143 or 0.5 cut off criteria, respectively. (F) A 5 nm thick section through the lower platform of the unsymmetrized average cryo-ET map (left) and its Fourier transform (right) indicate the overall 6-fold symmetry allowing for symmetric averaging for modeling. (G) Corresponding isosurfaces of unsymmetrized (left) and symmetrized (right) cryo-ET map of the lower platform. (H) Examples of simulated 6 nm resolution maps of complexes with imperfect hexagonal symmetry: Four IgGs with four headpieces (left) and six IgGs with four associated headpieces (right). Arrowheads indicate position of missing head pieces. (I) Sections through the simulated map of six IgG and four C1q headpieces at heights corresponding to the horizontal sections in Fig. 4B.

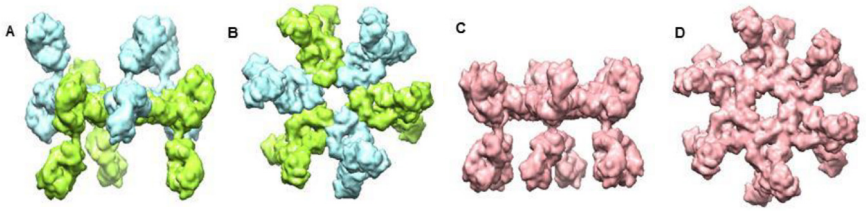

Fig. S5: Adaptation of the 1HZH IgG1-b12 hexamer structure for docking into the averaged cryo-ET density map. (A) Side view and (B) top view of 1HZH crystal packing showing alternating upwards oriented (blue) and downward oriented (green) Fab arms, with Fc segments in a central hexameric arrangement. (C) Side view and (D) top view of the adapted 1HZH structure with the upward oriented Fab segments flipped downwards (by 180° rotation around the Fc dimer axis), while keeping the hexameric arrangement in the Fc segments, resulting in six Fab arms pointing downwards and a platform comprising the other Fab arms and the Fc segments.

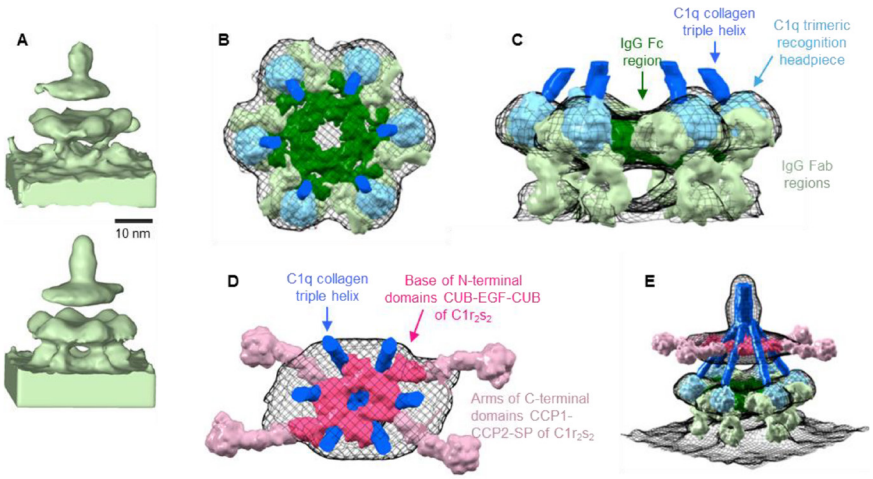

Fig. S6: Modeling the antibody-C1 complex. (A) Unsymmetrized (top) and symmetrized (bottom) isosurface density maps of the averaged antibody-C1 complexes. The symmetrized map was obtained by imposing six-fold symmetry to the lower platform and two-fold symmetry to the upper platform. (B) Top and (C) side view of the lower platform modeled by an IgG hexamer (green) interacting with C1q headpieces (light blue) and placed into the symmetrized ET map (black mesh). Fc segments form a hexameric ring (dark green) with Fab arms (light green) in an antigen-bound axial and an antigen-unbound equatorial orientation. Dark blue indicates the position of the collagen triple helices connected to the C1q headpieces. (D) C1r2s2 modeled with an N-terminal hetero-tetrameric base (dark pink) and four flexible arms exposing the serine protease domains (light pink). The electron density indicated the position of the N-terminal base, whereas the position of the proteolytic arms was unresolved. (E) Overview of the model with collagen stems and base (dark blue). The model was built as detailed in the Materials and Methods section (20).

Table S1: Apparent Kd values for C1q binding to antibody-opsonized cells. Mean Kd and SD for binding to Raji or Daudi cells opsonized with IgG1-7D8 or mutants thereof were calculated from C1q binding experiments as exemplified in Fig. 1D. Numbers of replicates and statistics are shown.

	Raji				Daudi			
Antibody	$N^{(1)}$	Mean K_d (nM)$^{(2)}$	SD$^{(2)}$	Significance$^{(3)}$	$N^{(1)}$	Mean K_d (nM)$^{(2)}$	SD$^{(2)}$	Significance$^{(3)}$
IgG1-7D8	3	6.5	3.1	n.a.	6	8.4	3.7	n.a.
I253A	3	18.6	7.9	*	4	21.5	8.0	**
I253D	3	109.1	55.0	**	4	157.4	44.2	***
I253Y	3	38.7	12.4	**	4	41.3	16.1	**
Q311A	3	9.1	3.5	n.s.	4	10.7	3.8	n.s.
H433A	3	97.9	23.3	***	4	117.5	67.0	**
N434A	3	44.9	12.5	***	4	40.4	9.7	***
H435A	3	7.3	2.3	n.s.	4	8.6	2.8	n.s.
H435R	3	4.7	1.4	n.s.	4	4.9	2.8	n.s.
K439E					2	361	81	***
S440K					2	109	87	*
K439E/S440K$^{(4)}$					4	2.6	1.6	*
K439E+S440K$^{(5)}$					3	3.3	0.3	n.s.
E345R					4	1.7	1.7	*

(1) Number of experiments. (2) Mean and standard deviation (SD.) were calculated from all experiments. (3) Statistics: 1 way ANOVA on log-transformed data followed by Dunnett's Multiple Comparison Posthoc Test (GraphPad Prism 5.01). Significance was calculated in comparison to the wild type IgG1-7D8: (n.a.) not applicable; (n.s.) not significant P > 0.05; *P < 0.05; **P <0.01; ***P < 0.001. (4) Double mutant. (5) Assessed as a mixture of single mutants (1:1). The experiments were performed in a blinded fashion with coded antibody samples.

Table S2: EC50 (antibody concentration inducing half-maximal lysis) values for CDC of antibody-opsonized cells. Mean EC50 and SD for CDC of Daudi cells opsonized with IgG1-7D8 or mutants thereof were assessed in the presence of human serum. Numbers of replicates and statistics are shown.

Antibody	$N^{(1)}$	Mean EC_{50} (µg/mL)$^{(2)}$	$SD^{(2)}$	Significance$^{(3)}$
IgG1-7D8	5	0.48	0.11	n.a.
I253A	4	0.79	0.15	n.s.
I253D	5	3.33	1.05	***
I253Y	4	1.77	0.43	***
H310K	3	3.03	0.30	***
Q311A	4	0.42	0.12	n.s.
G385D	3	2.12	0.45	***
H433A	5	3.44	1.17	***
N434A	4	1.77	0.46	***
H435A	4	0.81	0.27	n.s.
H435R	5	0.28	0.06	**
Y436D	3	1.88	0.45	***
Q438D	3	2.61	0.38	***
K439E	4	2.34	0.38	***
S440K	4	1.78	0.46	***
K439E/S440K[4]	4	0.33	0.08	n.s.
K439E+S440K[5]	4	0.48	0.17	n.s.
K322A	4	>30[6]	n.d.	[7]
E345R	4	0.04	0.01	***

(1) Number of experiments. (2) Mean and standard deviation (SD) were calculated from all experiments. (n.d.) not determined. (3) Statistics: 1 way ANOVA on log-transformed data followed by Dunnett's Multiple Comparison Posthoc Test (GraphPad Prism 5.01). Significance was calculated in comparison to the wild type IgG1-7D8. (n.a.) not applicable; (n.s.) not significant $P > 0.05$; **$P < 0.01$; ***$P < 0.001$. (4) Double mutant. (5) Assessed as a mixture of single mutants (1:1). (6) EC50 indicated as >30 µg/mL as 50% lysis was not reached. (7) This difference was considered significant although P-value could not be determined.

Table S3: Native mass spectrometry of the IgG1-RGY hexamer. Observed ion signals and derived molecular weights for the monomeric antibody IgG1-005, and the monomeric and hexameric species of the triple mutant IgG1-005-RGY. The experimentally measured mass of the hexamer, 890,327 Da, is within 0.1% of the expected mass of 6 times the mass of the IgG1-005-RGY monomer.

	IgG1-005		RGY	
z	m/z	Mass (Da)	m/z	Mass (Da)
29	5,107.9	147,288.1	5,123.9	148,593.1
28	5,290.0	147,336.0	5,305.2	148,545.6
27	5,485.5	147,379.5	5,501.4	148,537.8
26	5,696.3	147,427.8	5,712.2	148,517.2
25	5,924.0	147,475.0	5,940.5	148,512.5
24	6,170.7	147,520.8	6,188.1	148,514.4
Average		**147,404.5**		**148,536.8**
SD		**87.1**		**30.7**
76			11,714.8	890,248.8
75			11,870.6	890,220.0
74			12,032.6	890,338.4
73			12,196.6	890,278.8
72			12,366.5	890,316.0
71			12,540.9	890,332.9
70			12,723.2	890,554.0
Average				**890,327.0**
SD				**109.3**

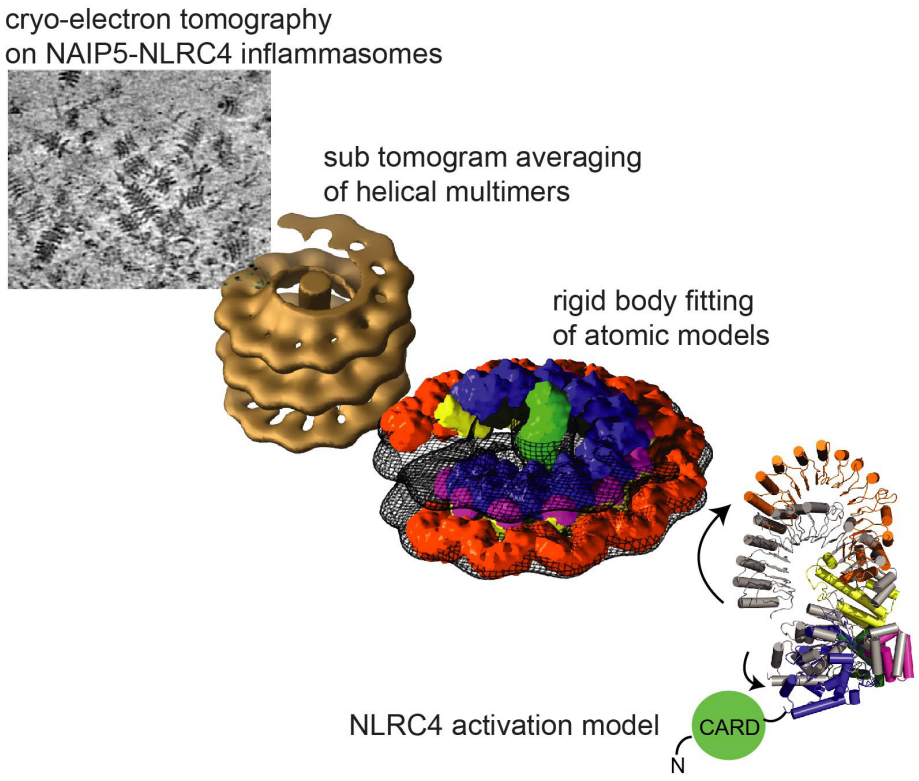
cryo-electron tomography
on NAIP5-NLRC4 inflammasomes
sub tomogram averaging
of helical multimers
rigid body fitting
of atomic models
NLRC4 activation model
CARD
N

CHAPTER 3

CRYO-ELECTRON TOMOGRAPHY OF THE NAIP5/NLRC4 INFLAMMASOME - IMPLICATIONS FOR NLR ACTIVATION

Christoph A. Diebolder [1,2,†], Els F. Halff [2,3,†], Abraham. J. Koster [1], Eric G. Huizinga [2], Roman I. Koning [1,*]

Submitted

[1]Department of Molecular Cell Biology, Leiden University Medical Center, P.O. Box 9600, 2300 RC Leiden, The Netherlands

[2]Crystal and Structural Chemistry, Bijvoet Center for Biomolecular Research, Department of Chemistry, Faculty of Science, Utrecht University, 3584 CH Utrecht, The Netherlands

[3]Current address: Department of Neuroscience, Physiology and Pharmacology, Division of Bioscience, University College London, London WC1E 6BT, United Kingdom

[†]These authors contributed equally to this work

[*]Corresponding author

SUMMARY

Inflammasomes are high molecular weight protein complexes that play a crucial role in innate immunity by activating caspase-1. Inflammasome formation is initiated when molecules originating from invading microorganisms activate NLRs and induce NLR multimerization. Little is known about the conformational changes involved in NLR activation and the structural organization of NLR multimers.
Here we show by cryo-electron tomography that flagellin-induced NAIP5/NLRC4 multimers form right- and left-handed helical polymers with a diameter of 28 nm and a rise of 6.5 nm. Sub tomogram averaging produced an electron density map at 4 nm resolution, which was used for rigid body fitting of NLR subdomains derived from the crystal structure of dormant NLRC4. The resulting structural model of inflammasome-incorporated NLRC4 indicates that a prominent rotation of the LRR domain of NLRC4 is necessary for multimer formation, providing unprecedented insight in the conformational changes that accompany NLR activation.

HIGHLIGHTS:

- Cryo-ET reveals structure of assembled NAIP5/NLRC4 multimers
- NAIP5/NLRC4 forms left- and right-handed helical polymers
- Rigid body fitting suggests a model for conformational changes within NLRC4 upon activation

INTRODUCTION

The innate immune system provides mechanisms for both recognition and clearance of invading microorganisms. In the cytosol the nucleotide-binding domain and leucine-rich repeat containing receptors (NLRs) play an essential role by recognizing a wide variety of pathogen associated molecular patterns (PAMPs) and subsequently inducing an immune response (*1*).
NLRs typically comprise three functional domains. The C-terminal leucine rich repeat (LRR) domain maintains the NLR in an auto-inhibited conformation in the absence of a stimulus (*2*). The central NOD or NACHT (Neuronal Apoptosis Inhibitor Protein (NAIP), Major Histocompatibility Complex Class II Transactivator (CIITA), HET-E and TP1) domain (*3*) is essential for ligand-induced and ATP-dependent multimerization of activated NLRs into an oligomeric complex (*4*, *5*). In this oligomer, the N-terminal effector binding domains (EBDs) are thought to be exposed, enabling the recruitment of downstream signaling proteins. For a subset of NLRs, activation leads to the recruitment and proteolytic activation of pro-caspase-1. Activated caspase-1 in turn processes pro-interleukins, thereby inducing inflammation and an inflammatory cell death called pyroptosis. Most caspase-1 activating NLRs possess a Pyrin Domain (PYD) as EBD at their N-terminus and require the helper protein ASC to recruit procaspase-1, whereas NLRC4 can directly interact with pro-caspase-1 via its N-terminal Caspase recruitment domain (CARD) (*5*). The assembled signaling hub containing the NLR multimer, ASC and pro-caspase-1 is termed inflammasome (*6*). Aberrant inflammasome formation is linked to severe inflammatory disorders such as Familial Cold Autoinflammatory Syndrome, enterocolitis, and macrophage activation syndrome (*7,8,9,10*). Understanding the

formation and composition of inflammasomes may prove important for understanding the underlying cause of these diseases.

Structural information on NLRs and the composition and formation of inflammasomes has only recently started to emerge. The crystal structure of monomeric CARD-deleted NLRC4 revealed how the dormant state is maintained by interactions between the LRR and NACHT domain as well as within the NACHT domain (*2*). Moreover, several EM-based studies provide insight into the prion-like polymerization of the effector molecules that regulate processes downstream of NLR activation (*11*,*12*). However, structural insight into the formation and composition of the NLR-containing core complex of inflammasomes is limited.

We recently provided the first negative stain electron tomography (ET) images of hetero-oligomeric NAIP5/NLRC4 multimers, which are formed upon specific detection of Salmonella Typhimurium flagellin by NAIP5. Our data suggested that they are disk-shaped particles comprising 11 or 12 protomers in a ring-like arrangement. Additionally, we also obtained helical structures that contained NLRC4 only (*13*). Similar filamentous structures, in addition to disk-like structures, have been reported for NLRP3 (*12*). In this study we employ cryo-electron tomography (cryo-ET) and sub tomogram averaging to obtain higher-resolution three-dimensional structural data of the hetero-oligomeric NAIP5/NLRC4 complex and to improve our understanding of its formation. We find that NAIP5/NLRC4 multimers occur as both left and right-handed helices of varying length, with the EBDs positioned at the center of the helix. Rigid-body fitting of the atomic structure of dormant mouse NLRC4 (*2*) into the sub-tomogram averaged map of the NAIP5/NLRC4 multimers suggests that conformational changes within the NACHT domain and rotation of the entire LRR domain are required to establish intermolecular interactions between neighboring NLRs and the formation of a CARD platform. Our data provides structural insight into the mechanism of NLR multimerization and the induction of downstream signaling.

RESULTS

Cryo-electron tomography reveals heterogeneity of NLRC4 containing inflammasomes. Our previous study on oligomeric complexes of NLRC4 and NAIP5/NLRC4/FliC-D0$_L$ by negative stain ET gave the first structural insights into inflammasome formation (*13*). Our data suggested that the hetero-oligomeric inflammasome comprises 11 or 12 protomers in a ring-shaped structure in which both NLRs occupy an equivalent position. To gain more structural detail we investigated the ultra-structures of fully hydrated samples, using cryo-ET. Complexes were purified from HEK293E cells either expressing murine NLRC4 alone or NLRC4 co-transfected with murine NAIP5 and the Salmonella Typhimurium flagellin fragment FliC-D0$_L$ as published previously (*13*,*14*). Cryo-EM of purified NLRC4 stored at high concentration shows large elongated complexes (Fig. 1A) that in size and shape are similar to the rod-shaped particles observed previously by negative stain EM (see Fig. 8C,D in *13*). Cryo-ET on NAIP5/NLRC4/FliC-D0$_L$ multimers likewise confirmed our previous observations, revealing similarly shaped and sized structures that resemble a dimeric disc (Fig. 1B, left panel) and occasionally elongated striated tube-like complexes (Fig. 1B, right panel; and see Fig. 8 E-G in *13*).

Our NAIP5/NLRC4/FliC-D0$_L$ particles bear strong resemblance to the homologous apoptosomes, in which the formation of dimeric discs was shown to be mediated by interaction between CARD-

exposing surfaces (*15,16*). To verify whether dimerization of NAIP5/NLRC4/FliC-D0$_L$ complexes is also CARD-mediated, we fused NLRC4 and NAIP5 at their N- or C- terminus to GFP and analyzed complex formation using native gel electrophoresis (fig. S1). Whereas fusion of GFP to the C-terminus of either NLR, or the N-terminal EBDs of NAIP5 leaves multimer size unaffected, fusion of GFP to the CARD of NLRC4 resulted in decreased complex size as seen on native gel (fig. S1, 3rd panel). This would indeed be consistent with obstruction of CARD-mediated dimerization.

In contrast to the appearance in stained samples, in which NAIP5/NLRC4/FliC-D0$_L$ complexes appeared to be a dimer of flat discs, analysis of the cryo-electron tomograms now suggests that the halves of the dimeric structures are short helical segments comprising one or two, or in rare cases more turns (Fig. 1B,C). In transversal cryo-tomograms slices through individual tubular NAIP5/NLRC4/FliC-D0$_L$ complexes the curved LRR domains protruding outwards can be observed, roughly indicating the location of individual NLRs (Fig. 1B, right panel, circle), as was also observed in tomograms of negatively stained NAIP5/NLRC/FliC-D0$_L$ samples (see Fig. 8F in *13*). Sub tomogram averaging of whole dimers, however, resulted in a very low resolution structure with the shape of an hourglass in which neither the structural build-up of the multimers nor individual protomers could be resolved (Fig. 1D). This loss of structural details upon averaging suggests heterogeneity of the particles.

Formation of rod-like NAIP5-PKG/NLRC4 particles. Neither negative stain ET nor sub tomogram

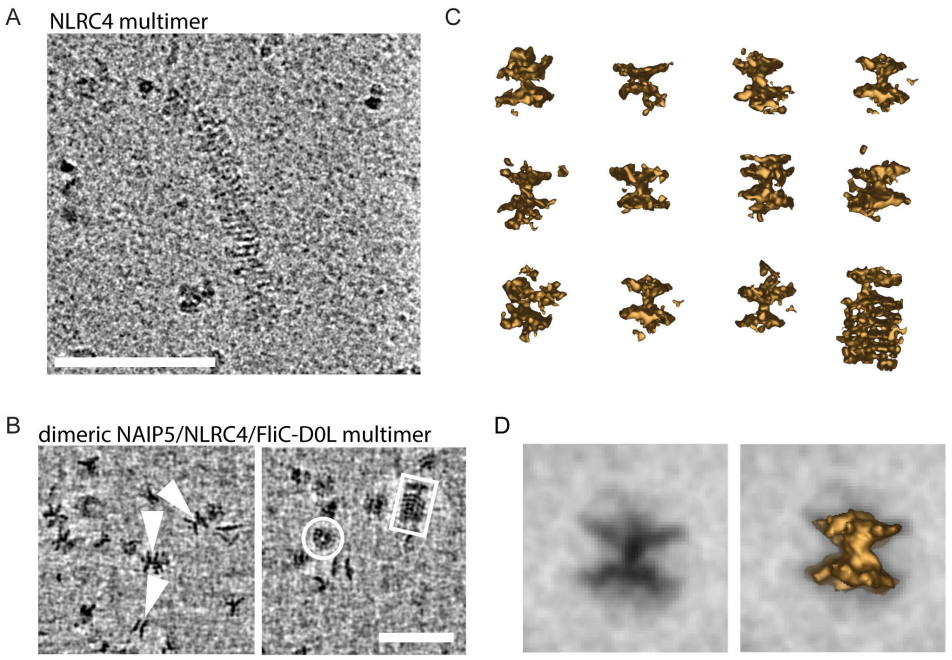

Figure 1: Structural heterogeneity of NLRC4-containing multimers. A: Cryo-EM projection image of an NLRC4 multimer. B: Sections through cryo-electron tomograms of dimeric NAIP5/NLRC4/FliC-D0$_L$ multimers at a concentration of 5 mg/ml, showing transversal (white circle) and lateral slices (white rectangle) through the complexes. Arrowheads denote dimer interfaces in lateral tomogram slices. C: Isosurface representations of selected particles seen in (B) reflecting a high degree of heterogeneity. D: Section (left panel) and isosurface representation (right panel) of averaged dimeric particles of NAIP5/NLRC4/FliC-D0$_L$. White scale bars represent 100 nm.

averaging of cryo-ET of dimeric particles allowed us to differentiate between NLRC4 (117kDa) and NAIP5 (160kDa). In an attempt to localize NAIP5 in the complex, we fused NAIP5 at its C-terminus to the 76kDa intracellular protein cGMP-dependent protein kinase I alpha (PKG). To achieve NAIP5-PKG/NLRC4 multimer formation, HEK293E cells were co-transfected with NLRC4-$Flag_3$-His_6, FliC-$D0_L$, and NAIP5-PKG-TEV-$StrepII_3$-His_6. Complex formation was assessed by single-step purification with StrepTactin beads (Fig. 2A). We verified that the presence of PKG does not induce auto-activation of NAIP5, or abrogate ligand-induced formation of the NAIP5/NLRC4 complex. Indeed we confirmed that, in the absence of FliC-$D0_L$, neither NAIP5 nor NAIP5-PKG form a complex with NLRC4. In the presence of FliC-$D0_L$, however, NLRC4 co-purifies with both NAIP5 and NAIP5-PKG and forms high molecular weight multimers. On native gel the NAIP5-PKG/NLRC4/FliC-$D0_L$ complex runs higher than the NAIP5/NLRC4/FliC-$D0_L$ complex and displays a more diffuse band than the complex without PKG-fusion, suggesting that the PKG-containing complex does differ in size and/or shape (Fig. 2A, 3rd panel). For structural analysis we purified the NAIP5-PKG/NLRC4 multimers at a larger scale by single-step affinity purification on StrepTactin beads as before, and additionally included a gel filtration purification step to remove monomeric NAIP5-PKG (Fig. 2B). SDS-PAGE analysis of affinity purified NAIP5-PKG/NLRC4/FliC-$D0_L$ complexes before and after gel filtration revealed NLRC4 to be the main component of the assembled multimers (Fig. 2C). Cryo-electron tomograms of the NAIP5-PKG/NLRC4/FliC-$D0_L$ multimer show dimeric particles with similar shape and diameter as tomograms of NAIP5/NLRC4/FliC-$D0_L$ multimers. However, they are longer, usually comprising two or more striations instead of one (Fig. 2D), which is in agreement with the increased molecular weight of this complex as measured by native gel electrophoresis (Fig. 2A). Averaging of the longer NAIP5-PKG/NLRC4/FliC-$D0_L$ multimers resulted in a structure with the shape of two double discs rather than single discs (Fig. 2E). This average had a slightly increased resolution (9 nm compared to 12 nm for the average of NAIP5/NLRC4/FliC-$D0_L$ (Fig. 1D)), indicating increased homogeneity and/or rigidity of the larger particles.

Sub tomogram averaging reveals helical buildup of NAIP5-PKG/NLRC4/FliC-$D0_L$ multimers. Initial sub tomogram averaging of the longest multimers resulted in a rod that seemed to consist of stacked disks. However, this average showed fewer features than the individual rods from the tomograms, since the LRR domains that were prominent in the tomograms did not show up in this average (Fig. 3C). This suggested that the rods might be a mix of left- and right- handed helices. Therefore we manually traced individual NAIP5-PKG/NLRC4/FliC-$D0_L$ multimers in the tomograms in order to determine their buildup. This indeed showed that both left- and right-handed helices were present in the tomograms, rather than stacked discs. To further confirm this apparent ambidexterity the 15 longest rods were analyzed for internal symmetry and grouped into two classes according to their handedness (Supplemental experimental procedures; Fig. 3A,B). For both classes, comprising 9 right-handed and 6 left-handed helices respectively, class averages were calculated making use of the visible rise of the helix, which for both multimers measures 6.5 nm. Both right and left-handed averaged helices show more structural detail than the combined average, which has a resolution of ~6 nm, according to the 0.5 FSC criterion (Fig. 3C).
The right-handed average (Fig. 3C, left panel; Fig 3D) has the highest resolution (~4 nm, fig. S2) and shows sufficient details to allow for determination and iterative refinement of helical symmetry parameters. After principle component analysis and unsupervised k-means clustering, the final

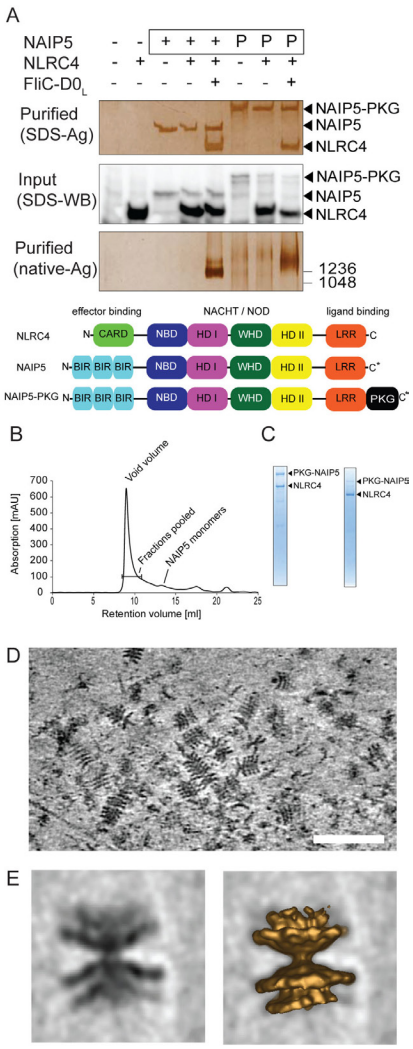

Figure 2: Purification and characterization of NAIP5-PKG/NLRC4/FliC-D0L multimers. A: Analysis of multimer formation in HEK293E cells transfected with proteins indicated. Boxed proteins carry a $StrepII_3$-His_6 purification handle; "P" indicates fusion to PKG at the C-terminus. Purified protein was analysed by SDS-PAGE (1st panel) or native PAGE (3rd panel, size markers on the right in kDa), followed by silver staining. Cleared cell lysate was analysed on Western blot probed with anti-His-antibody (2nd panel). Schematic of NLR constructs used; asterisks indicate position of the purification tag. B: Elution profile of NAIP5-PKG/NLRC4/FliC-$D0_L$ complexes separated by gel filtration after affinity purification on StrepTactin beads. Fractions pooled for cryo-ET analysis (D) are indicated. C: SDS-PAGE analysis of NAIP5-PKG/NLRC4/FliC-$D0_L$ complexes after affinity purification (left) and gel filtration (right). D: Section through cryo-electron tomogram of NAIP5-PKG/NLRC4/FliC-$D0_L$ multimers at a concentration of 1.2 mg/ml. White scale bar represents 100 nm. E: Section (left panel) and isosurface representation (right panel) of averaged dimeric particles of NAIP5-PKG/NLRC4/FliC-$D0_L$.

average comprised 50 protomers originating from initially 900 boxed protomers (100 per particle). The right-handed NAIP5-PKG/NLRC4/FliC-D0$_L$ multimer has a diameter of 28 nm, rise of 6.5 nm and shows H5.57±0.34 Å,+30.9°,1,1 symmetry according to EM convention (Fig. 3D,E; *17*), resulting in 11.65 protomers per turn, which is in accordance with the 11-12 protomers observed before (*13*).
The averaged density map reveals a structure containing a central rod shaped core, which forms the axis of an outer helical rim. In analogy to the homologous apoptosomes in which the ligand binding domains protrude outwards (*18*), the rim of the helix is expected to be formed by the C-terminal LRR domains of the NLRs, which display a typical arc-like structure. Indeed, the outer rim is well defined resembling connected arcs, which indicate the position of individual protomers (Fig. 3E). Closer to the center of the helix the density curves upward, a shape that is reminiscent of the so-called concave hub observed in apoptosomes, where it contains the NACHT domains. In apoptosomes, the concave hub forms a closed ring, whereas in our structure it forms a continuous helix (Fig. S3). We presume that the central rod-like density, which is weakly connected to the ring structure, harbors the EBDs, being either CARDs or baculovirus inhibitor of apoptosis repeat (BIR) domains.

Rigid body fitting of NLRC4 fragments has implications for an NLRC4 activation model. In order to interpret the helical map, we fitted atomic models derived from the crystal structure of dormant NLRC4 (PDB ID 4KXF; (*2*)) to the averaged and symmetrized right-handed EM map (Fig. 3F,G). The crystal structure of NLRC4 comprises the central NACHT and C-terminal LRR domains; both domains are also present in NAIP5. Given the overall conservation of their NACHT and LRR domains (24.7% identity and 34.2% similarity; fig. S4) and the limited resolution of the EM map we expected that a NACHT-LRR model based on the structure of NLRC4 is also adequate for the corresponding NAIP5 regions. The N-terminal NLRC4 CARD is absent in the crystal structure and therefore we used the crystal structure of the Apaf-1 CARD (PDB ID 1Z6T; *19*) for modeling. The 11 kDa FliC-D0$_L$ fragment that induces inflammasome formation by interacting with NAIP5 was omitted in the fitting procedure; due to its small size compared to the resolution of the map, the yet unknown binding site to NAIP5, and its presence in substoichiometric amounts, the contribution of the fragment to the averaged map will be negligible.
We first manually fitted the NLRC4 crystal structure into the density of the EM map, guided by the obvious position and direction of the LRR domains in the outer rim of the helix. Subsequent generation of symmetry-related protomers using the helical parameters resulted in severe steric clashes, while part of the EM map remains unoccupied (fig. S5A), indicating that multimerization requires substantial conformational rearrangements within NLR monomers.
Hu et al. proposed a mechanism for NLRC4-activation in which the NACHT subdomains Winged Helix Domain (WHD) and Helical Domain II (HD2) together with the LRR domain move as one rigid body with respect to the other two NACHT subdomains Nucleotide Binding Domain (NBD) and Helical Domain I (HD1) (*2*). Our data indicate, however, that this is not the case, since manual fitting of the WHD-HD2-LRR fragment resulted in significant protrusion of the HD2 domain (fig. S5B). In subsequent fitting attempts we therefore considered the LRR domain as a separate rigid body.
Since inflammasomes and apoptosomes have many functional and structural similarities (*20*), we tested the hypothesis that their NACHT subdomains are similarly arranged in the active conformation. The Apaf-1 and NLRC4 NACHT subdomains are structurally conserved with the

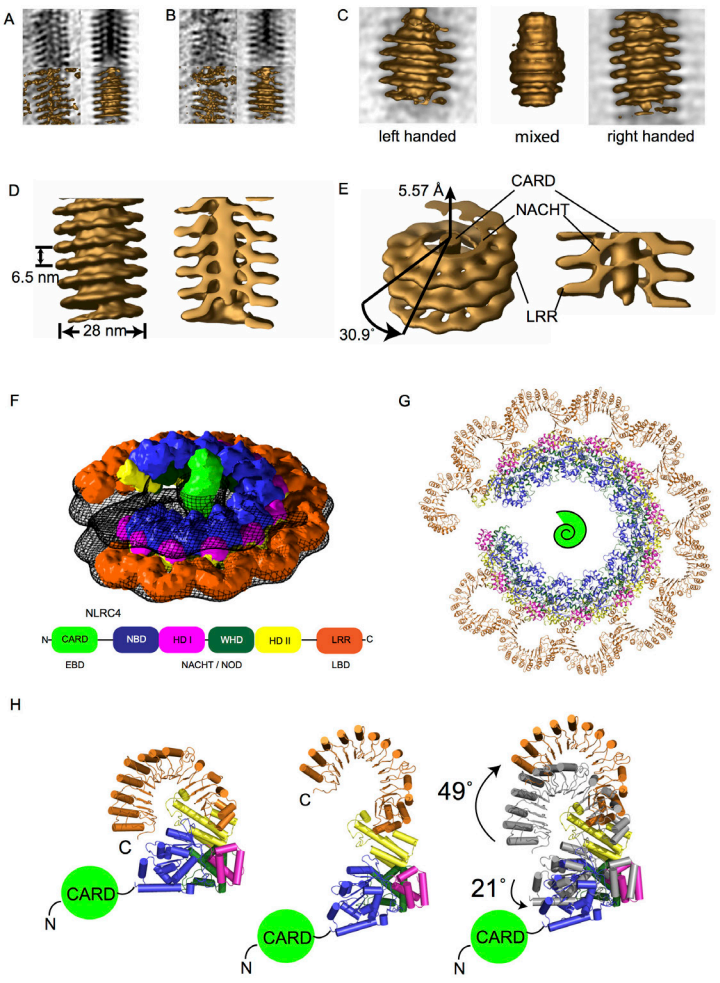

Figure 3: Sub-tomogram averaging and domain modeling of NAIP5-PKG/NLRC4/FliC-D0$_L$ multimers. A: Sections (upper panels) and isosurfaces (lower panels) of un-averaged individual particle (left) and the same particle after internal averaging using right-handed helical symmetry with slope of 6.5 nm (right). B: Similar analysis as in panel A of a particle assuming left-handed symmetry. C: Isosurfaces of sub tomogram averages of particle classes with right-handed (9 particles, left) or left-handed symmetry (6 particles, right) as well as an average of all 15 particles before classification (centre). D: Isosurface of refined right-handed average at ~40 Å resolution (left) and lateral section (right). Helical pitch and diameter are indicated. E: Surface renderings of helix (left) and section along the helix (right) of symmetrized average map of right-handed particles using H5.57±0.34 Å,+30.9°,1,1 symmetry. Proposed locations of NLRC4 domains are indicated. F: Fit of final pseudo atomic NLRC4 model of 11 protomers (coloured) into the symmetric average map of the right-handed multimer (meshed). The model is downsampled to 10 Å resolution; color-coding given in schematic at bottom is similar in G and H. G: Top view of the same model in ribbon representation (excluding the CARDs which are indicated as a green spiral). H: NLRC4 activation model. Shown are cartoon representations of the crystal structure of inactive NLRC4 (left, PDB ID 4KXF), the cryo-ET based model active NLRC4 (center) and an overlay of both models superposed on the WHD-HD2 segment (right, grey indicating inactive NLRC4).

exception of HD2 (fig. S6B). In Apaf-1 the NBD and HD1 are held together by the presence of a nucleotide, and activation causes a rotation of the WHD-HD2 fragment with respect to the NDB-HD1 fragment. To generate an Apaf-1-like active conformation, and assuming conservation of interdomain interfaces, we rearranged the WHD-HD2 fragment of NLRC4 with respect to its NBD-HD1 fragment, guided by the position of the WHD in apoptosome-incorporated Apaf-1. As with previous models this model did not fit the density (fig. S5C), indicating that the active conformation of the NACHT domain differs between inflammasomes and apoptosomes.

Finally, a satisfactory model could be obtained by fitting the NBD-HD1, WHD-HD2 and LRR domains as separate rigid bodies into the EM density. To this end the NLRC4 NACHT domain was initially placed in the density in its dormant conformation with the NBDs facing towards the central rod, similar to the orientation in the apoptosome, and the HD2 C-terminus positioned in close proximity to the N-terminus of the LRR domain, which was placed independently. Next, three consecutive symmetry related molecules were generated and minor adjustments in their orientation were applied manually to reduce clashes with symmetry related neighbors. This manual fit was refined computationally based on iterative rigid body refinement of symmetry related copies of NBD-HD1, WHD-HD2, and LRR domains (Fig 3F,G and fig. S5D).

During manual fitting of the CARD in the density of the central rod it became evident that it did not follow the helical symmetry of the NACHT-LRR region; generation of symmetry related CARDs resulted in severe steric clashes, while leaving a large fraction of the density unoccupied. When no symmetry constraints were applied, however, the CARDs could fill the density of the central rod satisfactory (fig. S7A). Because of its deviating symmetry, the CARD was not included in further automated optimization of the model.

The resulting optimized model shows a putative conformation of NLRC4 in its activated and polymerized state (Fig. 3H). Comparison of this model with the crystal structure of inactive NLRC4 (*2*) reveals significant conformational changes: a 21° rotation of the NBD-HD1 segment and a 49° rotation of the LRR domain with respect to the WHD-HD2 fragment generates an "open lock" structure. This conformational change exposes previously buried surfaces of the NACHT, thereby sterically allowing helical NLR oligomerization. Our results show that the conformational change within the NACHT domain of NLRC4 in the formation of inflammasomes is distinctly different from that in apoptosome formation. This may explain how these NLRs do not form a ring-like structure similar to apoptosomes, but rather polymerize into a helical multimer.

CONCLUSIONS AND DISCUSSION

NLRs have been shown to play an essential role in the induction of an inflammatory immune response. Their activation through detection of invading microorganism induces a conformational change that leads to their multimerization followed by recruitment of downstream signaling partners into the multi-component inflammasome. Recent high-resolution studies shed light on the polymerization mechanism of the activated inflammasome components ASC and pro-caspase-1 (*11*,*12*), however our understanding of the formation and composition of the NLR oligomer that is at the core of the inflammasome is limited. In this study we use cryo-ET to analyze the structure of hetero-oligomeric NAIP5/NLRC4 and NAIP5-PKG/NLRC4 complexes. We show that they form a heterogeneous mixture of particles, which can appear as dimeric disk-like structures, as well as

flexible left- and right-handed helices of variable length. The longer helices enabled analysis of the inflammasome structure. The right-handed conformation has a diameter of 28 nm, a rise of 6.5 nm and H5.57±0.34 Å,+30.9°,1,1 symmetry. Aided by the helical symmetry we obtained a sub tomogram averaged map at a resolution of ~4 nm. Rigid body fitting of atomic models of NLR domains into this map gives insight into the quaternary structure of NAIP5/NLRC4 multimers. Comparison of the crystal structure of dormant NLRC4 (*2*) with our model for inflammasome-incorporated NLRC4 suggests that NLR activation and formation of the helical multimer is accompanied by conformational changes between NLR domains, in particular involving a movement of the LRR domain away from the NACHT domain, that enable interaction with neighboring NLRs in the oligomer. Based on existing data and our current findings we propose that NAIP5-NLRC4 inflammasomes are formed by the following four-step model (Fig. 4): [I] FliC-$D0_L$ primes NLRC4 by inducing phosphorylation (*21*) and activates NAIP5 by binding to a region within the NAIP5 NACHT domain (*22*). [II] The NAIP5/FliC-$D0_L$ and pre-activated NLRC4 form a complex that [III] nucleates polymerization of NLRC4 upon the NAIP5/NLRC4/FliC-$D0_L$ complex into a helical inflammasome. Finally, the assembled platform of CARDs [IVa] recruits and activates caspase-1 or [IVb] causes dimerization of the particles.

In our model a single molecule of NAIP5, activated by direct recognition of the flagellin $D0_L$ domain, forms a complex with primed NLRC4. Although no structure of dormant NAIP5 exists, we assume that both NLRs undergo similar conformational rearrangements. This NAIP5/NLRC4/FliC-$D0_L$ complex then serves as an initiator or NLRC4 polymerization, allowing formation of a hetero-oligomeric helical complex. Both left and right-handed helices can be formed, although in our study right-handed helices were more prevalent. Several observations suggest that the helices mainly comprise NLRC4: [1] we previously observed that NLRC4 can spontaneously polymerize into helical structures, whereas NAIPs do not self-associate (*13,22*); [2] SDS-PAGE analysis of the purified complexes used in this study showed that NAIP5 is far less abundant than NLRC4 (Fig. 1C); and [3] fitting of CARDs into the central rod of the EM-derived map leaves only limited residual density, suggesting that only occasionally a CARD can be replaced by 3 BIR domains. Since NAIP5 is required to initiate complex formation we assume that it is mainly located at the start of the helices, although we were unable to verify this statement as the final averaged map was of insufficient resolution to discern individual protomers. However, we cannot exclude the possibility that additional but non-adjacent copies of NAIP5 are incorporated in the helical core and/or at the end. Indeed, a recent analysis of NAIP/NLRC4 inflammasomes revealed an average ratio of 5 molecules of NLRC4 for each 2 molecules of NAIP (*22*).

Other NAIP/NLRC4 inflammasomes are likewise formed upon detection of PAMPs that are structurally related to flagellin. This functional similarity combined with the high sequence conservation between different NAIPs suggests that the here proposed structural model for formation of the NAIP5/NLRC4 inflammasome will also be valid for other hetero-oligomeric NAIP/NLRC4 inflammasomes. Whereas NAIPs determine ligand specificity (*13,23,24,25*), induction of downstream caspase-1 activation is thought to be solely dependent on the NLRC4 N-terminal CARD (*26*). Our analysis of complex formation between NLRC4 and NAIP5 N-terminally fused to GFP indicates that NAIP5/NLRC4/FliC-$D0_L$ complexes dimerize via their exposed EBDs. As noted for apoptosomes, dimerization might well be concentration dependent (*15,16*), whereas the physiological relevant, caspase-1 activating inflammasome will be a single complex (Fig. 4 and fig.

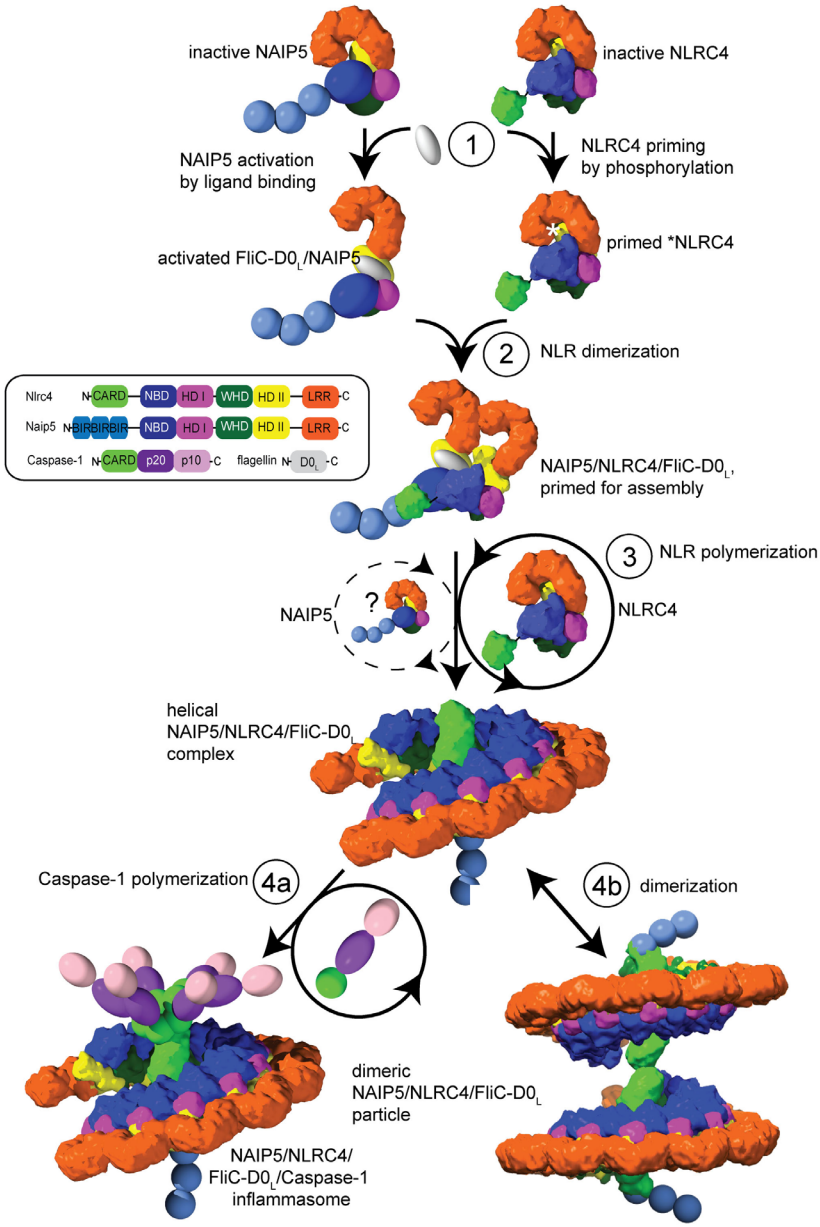

Figure 4: Stepwise NAIP5/NLRC4 inflammasome activation model. 1: Flagellin primes NLRC4 by inducing phosphorylation, and binds and activates NAIP5. The white asterisk indicates the phosphorylation site in NLRC4 2: Activated NAIP5 recruits and activates primed NLRC4 by inducing similar conformational rearrangements to form the NAIP5/NLRC4/FliC-D0$_L$ complex. 3. This complex forms a nucleation site for helical NLRC4 polymerization. Activated NAIP5 might also be incorporated in low frequency. 4a: The CARD exposing side forms a nucleation complex for Caspase-1 multimerization. 4b: Alternatively, the CARD exposing side of the helical complex allows dimerization. In the helical complexes, 11 NAIP5/NLRC4 molecules are shown.

S3). We find the CARDs not only to form a dimerization platform at one side of the NAIP5/NLRC4/FliC-D0$_L$ multimer but also to display a filamentous buildup at the core of the complex. It may well be that NLRC4 polymerization via the NACHT domain forces the CARDs into these filaments. However, as recent studies show that CARDs can polymerize into filaments in the absence of NACHT domains (*27*) an alternative possibility is that exposure of the CARD upon NLRC4 activation induces CARD filament formation, which in turn drives NLRC4 polymerization. In a similar way, PYD polymerization might drive NLRP3 filament formation (*11,12,28*).

We observe substantial variation in filament length between different preparations and constructs. It is known that protein overexpression may lead to self-assembly, therefore we expect that the longer helices that enabled us to determine the NLR-multimer structure only form at high non-physiological concentrations and might not have a biological significance. As NLRs are naturally expressed at a low level, and caspase-1 activation can only occur at the CARD-exposing end of NLR multimers, the biologically relevant particles may well be the shorter helices that we observed in preparations of NAIP5/NLRC4/FliC-D0$_L$ inflammasomes where NAIP5 is not fused to PKG. On the other hand, heterogeneity in particle size has been reported in other studies and may be an inherent characteristic of inflammasomes. Moreover, the particle size of NLR multimers may be affected by the presence of other inflammasome components: hetero-oligomeric NLRP3/NLRC4 complexes formed in vivo in the presence of ASC and caspase-1 assembled into specks of sizes up to 1 µm (*30*). Future work to elucidate why sizes differ between the different inflammasome preparations might include (integrated) cryo-(super-resolution) correlative light and electron microscopy on cell sections to transition from in vitro structural analysis of isolated compounds to in situ imaging of whole assembled inflammasomes. Irrespective of their length and dimensions, the EBD-exposing NLR multimers will be able to nucleate the filament and/or speck formation of downstream signaling molecules as has been described in recent work (*28,29,30*).

Helical prion-like polymerization is an emerging concept that seems to be common to several effector molecules downstream of ASC-dependent and independent inflammasomes (*11,12,28,29*). We now add to this data a high-resolution prion-like structure of NLRs. To our knowledge, the model provided in our study offers the highest resolution information on NLR multimers yet. Importantly, the model is in agreement with other studies showing filamentous structures for inflammasomes, as well as the hypothesis that ligand binding by NLRs induces an activation mechanism that requires conformational changes within the protein, particularly a release of interaction between the LRR and NACHT domain. Based on the similarities with other recent studies, we hypothesize that the model provided here is also relevant for other NLR containing inflammasomes.

EXPERIMENTAL PROCEDURES

All NLR constructs were expressed in HEK293E cells using pUPE vectors (U-Protein Express BV, The Netherlands) and purified using StrepTactin Sepharose beads (GE Healthcare) as described previously (*12,13*). Complexes containing NAIP5-PKG were further purified by gel filtration. Purification and complex formation was evaluated by native and SDS PAGE.

For cryo-EM samples were plunge frozen in liquid ethane/propane. All data was collected at a Titan Krios TEM (FEI) at NeCEN (Leiden, the Netherlands) using either a Falcon I direct electron detector (FEI, single particle) or Quantum energy filter (Gatan, electron tomography). Single particle analysis

was performed with EMAN2 software package (*31*). Tomograms were reconstructed in IMOD (*32*), sub tomograms averaged using PEET (*33*). Pseudo atomic model were created by rigid body fitting using Situs (*34*). Results were visualized in UCSF Chimera (*35*) and IMOD.

AUTHOR CONTRIBUTION

CAD, EFH, EGH and RIK designed experiments. CAD and EFH performed experiments with the help of RIK. CAD, EFH, EGH and RIK drafted the manuscript. All authors commented on the manuscript. AJK, EGH and RIK supervised the studies.

ACKNOWLEDGEMENTS

Cryo-EM data was collected at the Netherlands Centre for Electron Nanoscopy (NeCEN), Leiden, NL; C.A.D. is supported by European Research Council advanced grant 233229; E.F.H. & E.G.H were partly funded by Top Institute Pharma, project D1-101, A.J.K. by NanoNextNL, and R.I.K. by the Dutch Cyttron II project (FES 2009 LSH framework); The cryo-ET average map of right-handed NAIP5-PKG/NLRC4 complex is archived at EMDataBank (entry: EMD-2901).

REFERENCES

1. G. Chen, M. H. Shaw, Y. G. Kim, and G. Nunez, NOD-like receptors: role in innate immunity and inflammatory disease, *Annual Review of Pathological Mechanical Disease* **4**, 365-398 (2009).
2. Z. Hu, C. Yan, P. Liu, Z. Huang, R. Ma, C. Zhang, R. Wang, Y. Zhang, F. Martinon, and D. Miao, Crystal structure of NLRC4 reveals its autoinhibition mechanism, *Science* **341**, 172-175 (2013).
3. E. V. Koonin and L. Aravind, The NACHT family-a new group of predicted NTPases implicated in apoptosis and MHC transcription activation, *Trends in biochemical sciences* **25**, 223-224 (2000).
4. N. Inohara and G. Núñez, The NOD: a signaling module that regulates apoptosis and host defense against pathogens, *Oncogene* **20**, (2001).
5. K. Schroder and J. Tschopp, The inflammasomes, *Cell* **140**, 821-832 (2010).
6. F. Martinon, K. Burns, and J. Tschopp, The inflammasome: a molecular platform triggering activation of inflammatory caspases and processing of proIL-b, *Mol cell* **10**, 417-426 (2002).
7. Canna,S.W., de Jesus,A.A., Gouni,S., Brooks,S.R., Marrero,B., Liu,Y., DiMattia,M.A., Zaal,K.J., Sanchez,G.A.M., and Kim,H, An activating NLRC4 inflammasome mutation causes autoinflammation with recurrent macrophage activation syndrome. *Nature genetics* **46**, 1140-1146.
8. Romberg,N., Al Moussawi,K., Nelson-Williams,C., Stiegler,A.L., Loring,E., Choi,M., Overton,J., Meffre,E., Khokha,M.K., and Huttner,A.J. (2014). Mutation of NLRC4 causes a syndrome of enterocolitis and autoinflammation. Nature genetics 46, 1135-1139.
9. Kitamura,A., Sasaki,Y., Abe,T., Kano,H., and Yasutomo,K. (2014). An inherited mutation in NLRC4 causes autoinflammation in human and mice. The Journal of experimental

medicine 211, 2385-2396.

10. D. R. Mason, P. L. Beck, and D. A. Muruve, Nucleotide-binding oligomerization domain-like receptors and inflammasomes in the pathogenesis of non-microbial inflammation and diseases, *Journal of innate immunity* **4**, 16-30 (2011).
11. X. Cai, J. Chen, H. Xu, S. Liu, Q. X. Jiang, R. Halfmann, and Z. J. Chen, Prion-like polymerization underlies signal transduction in antiviral immune defense and inflammasome activation, *Cell* **156**, 1207-1222 (2014).
12. A. Lu, V. G. Magupalli, J. Ruan, Q. Yin, M. K. Atianand, M. R. Vos, G. F. Schröder, K. A. Fitzgerald, H. Wu, and E. H. Egelman, Unified polymerization mechanism for the assembly of ASC-dependent inflammasomes, *Cell* **156**, 1193-1206 (2014).
13. E. F. Halff, C. A. Diebolder, M. Versteeg, A. Schouten, T. H. Brondijk, and E. G. Huizinga, Formation and structure of a NAIP5-NLRC4 inflammasome induced by direct interactions with conserved N-and C-terminal regions of flagellin, *Journal of Biological Chemistry* **287**, 38460-38472 (2012).
14. E. F. Halff, M. Versteeg, T. H. Brondijk, and E. G. Huizinga, When less becomes more: Optimization of protein expression in HEK29-EBNA1 cells using plasmid titration-A case study for NLRs, *Protein expression and purification* **99**, 27-34 (2014).
15. S. Yuan, X. Yu, M. Topf, S. J. Ludtke, X. Wang, and C. W. Akey, Structure of an apoptosome-procaspase-9 CARD complex, *Structure* **18**, 571-583 (2010).
16. S. Yuan, X. Yu, M. Topf, L. Dorstyn, S. Kumar, S. J. Ludtke, and C. W. Akey, Structure of the Drosophila Apoptosome at 6.9 Å Resolution, *Structure* **19**, 128-140 (2011).
17. J. B. Heymann, M. Chagoyen, and D. M. Belnap, Common conventions for interchange and archiving of three-dimensional electron microscopy information in structural biology, *Journal of structural biology* **151**, 196-207 (2005).
18. D. Acehan, X. Jiang, D. G. Morgan, J. E. Heuser, X. Wang, and C. W. Akey, Three-dimensional structure of the apoptosome: implications for assembly, procaspase-9 binding, and activation, *Molecular cell* **9**, 423-432 (2002).
19. S. J. Riedl, W. Li, Y. Chao, R. Schwarzenbacher, and Y. Shi, Structure of the apoptotic protease-activating factor 1 bound to ADP, *Nature* **434**, 926-933 (2005).
20. M. Proell, S. J. Riedl, J. H. Fritz, A. M. Rojas, and R. Schwarzenbacher, The Nod-like receptor (NLR) family: a tale of similarities and differences, *PloS one* **3**, e2119 (2008).
21. M. Matusiak, N. Van Opdenbosch, L. V. Walle, J. C. Sirard, T. D. Kanneganti, and M. Lamkanfi, Flagellin-induced NLRC4 phosphorylation primes the inflammasome for activation by NAIP5, *Proceedings of the National Academy of Sciences* **112**, 1541-1546 (2015).
22. J. L. Tenthorey, E. M. Kofoed, M. D. Daugherty, H. S. Malik, and R. E. Vance, Molecular Basis for Specific Recognition of Bacterial Ligands by NAIP/NLRC4 Inflammasomes, *Molecular cell* **54**, 17-29 (2014).
23. Y. Zhao, J. Yang, J. Shi, Y. N. Gong, Q. Lu, H. Xu, L. Liu, and F. Shao, The NLRC4 inflammasome receptors for bacterial flagellin and type III secretion apparatus, *Nature* **477**, 596-600 (2011).
24. E. M. Kofoed and R. E. Vance, Innate immune recognition of bacterial ligands by NAIPs determines inflammasome specificity, *Nature* **477**, 592-595 (2011).
25. J. Yang, Y. Zhao, J. Shi, and F. Shao, Human NAIP and mouse NAIP1 recognize bacterial type

III secretion needle protein for inflammasome activation, *Proceedings of the National Academy of Sciences* **110**, 14408-14413 (2013).

26. S. Mariathasan, K. Newton, D. M. Monack, D. Vucic, D. M. French, W. P. Lee, M. Roose-Girma, S. Erickson, and V. M. Dixit, Differential activation of the inflammasome by caspase-1 adaptors ASC and Ipaf, *Nature* **430**, 213-218 (2004).
27. H. Xu, X. He, H. Zheng, L. J. Huang, F. Hou, Z. Yu, M. J. de la Cruz, B. Borkowski, X. Zhang, and Z. J. Chen, Structural basis for the prion-like MAVS filaments in antiviral innate immunity, *eLife* **3**, (2014).
28. A. C. Sahillioglu, F. Sumbul, N. Ozoren, and T. Haliloglu, Structural and Dynamics Aspects of ASC Speck Assembly, *Structure* **22**, 1722-1734 (2014).
29. A. Lu, and H Wu. Structural mechanisms of inflammasome assembly. *FEBS Journal* **27** (2014).
30. S.M. Man, L.J. Hopkins, E. Nugent, S. Cox, I.M. Glück, P. Tourlomousis, J.A. Wright, P. Cicuta, T.P. Monie, C.E. Bryant,Inflammasome activation causes dual recruitment of NLRC4 and NLRP3 to the same macromolecular complex. *Proceedings of the National Academy of Sciences* **111**, 7403-7408 (2014).
31. G. Tang, L. Peng, P. R. Baldwin, D. S. Mann, W. Jiang, I. Rees, and S. J. Ludtke, EMAN2: an extensible image processing suite for electron microscopy, *Journal of structural biology* **157**, 38-46 (2007).
32. J. R. Kremer, D. N. Mastronarde, and J. R. McIntosh, Computer visualization of three-dimensional image data using IMOD, *Journal of structural biology* **116**, 71-76 (1996).
33. D. Nicastro, C. Schwartz, J. Pierson, R. Gaudette, M. E. Porter, and J. R. McIntosh, The molecular architecture of axonemes revealed by cryoelectron tomography, *Science* **313**, 944-948 (2006).
34. W. Wriggers, Using Situs for the integration of multi-resolution structures, *Biophysical reviews* **2**, 21-27 (2010).
35. F. Pettersen, T. D. Goddard, C. C. Huang, G. S. Couch, D. M. Greenblatt, E. C. Meng, and T. E. Ferrin, UCSF Chimera-a visualization system for exploratory research and analysis, *Journal of computational chemistry* **25**, 1605-1612 (2004).

SUPPLEMENTAL EXPERIMENTAL PROCEDURES

Cell culture and transfection. HEK293E cells were cultured in Freestyle medium (Invitrogen), containing 0.2% FCS, 50 µg/ml G418 disulfate at 37°C in a 5% CO_2 humidified atmosphere. The cells were grown in suspension at 120 rpm. Small scale (4 ml) and large scale (400 ml) transfections were performed according to Durocher *et al*. (*36*).

Plasmids. Expression plasmids for murine NAIP5, murine NLRC4 and the Salmonella Typhimurium flagellin $D0_L$ fragment were created as described (*13*). To create the vector expressing bovine cGMP-dependent protein kinase I alpha (PKG) as a C-terminal fusion protein, the coding sequence of PKG was amplified by PCR using a forward primer that introduces a NotI restriction site while omitting the start codon, and a reverse primer that omits the stop-codon and introduces a C-terminal PspOMI restriction site followed by a BsmBI restriction site that creates a PspOMI overhang. At the protein level this procedure results in the introduction of three Ala residues at the N-terminus and a Gly-Ala sequence at the C-terminus of PKG. The PCR product was cloned into a pUPE vector (U-Protein Express BV, The Netherlands) to create a plasmid that encodes a C-terminal TEV-PKG-$StrepII_3$-His_6 tag. Expression vectors for mNLRC4 encoded a C-terminal $Flag_3$-His_6 tag, an N-terminal His_6-GFP-tag, or no tag. Expression vectors for mNAIP5 encoded a C-terminal TEV-$StrepII_3$-His_6, TEV-$StrepII_3$ or TEV-PKG-$StrepII_3$-His_6 tag or a combination of an N-terminal His_6-GFP plus a C-terminal TEV-$StrepII_3$ tag. The FliC-$D0_L$ fragment was expressed without tags.

Protein purification and gel filtration. For small scale purification from 4 ml HEK293E cultures, cells were harvested 48 hours post-transfection by centrifugation at 600 x *g* for 5 min. Cell pellets were stored for 1 hour up to 1 week at -20°C. For purification, pellets were thawed at room temperature. Cytoplasmic extracts were obtained using a method described by Tsai *et al*. (*37*), with omission of the PBS washing step. In short, cell pellets were resuspended in 320 µl cold small scale lysis buffer containing 10 mM HEPES pH 7.6, 5 mM $MgCl_2$, 10 mM KCl , 5 mM DTT, 1 µg/ml DNase and 1 tablet Complete mini, EDTA-free tablets (Roche) per 20 ml buffer. $StrepII_3$-tagged proteins were purified from the cleared cytoplasmic extracts using StrepTactin Sepharose beads (GE Healthcare). After incubation for 1-2 hrs at 4°C, beads were washed in StrepTactin wash buffer (100 mM NaCl, 25 mM HEPES pH 7.5, 5 mM benzamidin, 5% glycerol, 2 mM DTT), and subsequently protein was eluted in wash buffer supplemented with 5 mM *d*-desthiobiotin (Sigma).

For structural analysis by electron microscopy (EM), complexes were purified from 400 ml HEK293E cell cultures co-transfected with murine *NLRC4*-$Flag_3$-His_6, tagless FliC-$D0_L$, and either NAIP5-TEV-$StrepII_3$-His_6 or NAIP5-TEV-PKG-$StrepII_3$-His_6. Cells were harvested 72-96h post transfection by spinning at 600 x *g* for 10 min. Pellets were stored at -80°C until further purification. Affinity purification was performed as described for small scale purifications, scaled up according to the culture volume.

Complexes containing NAIP5-PKG were further purified by gel filtration. Affinity-purified protein was first concentrated on a 50 kDa cutoff filter spin tube (Millipore). The concentrated sample was then injected on a Superose-6 10/300 column (GE Healthcare) equilibrated in gel filtration buffer (100 mM NaCl, 20 mM HEPES pH 7.5, 2 mM Benzamidin, 2 mM DTT). Fractions were pooled as indicated in Figure 2 and protein was concentrated to ~1.2 mg/ml.

Gel electrophoresis and protein detection. Reduced protein samples were separated on standard Laemmli 9% SDS-PAGE gels. Samples for native gel electrophoresis were run on 3-12% NativePAGE Novex Bis-Tris gels (Invitrogen) according to the manufacturer's protocol, using NativeMark Unstained Protein Standard (Invitrogen) as marker. Gels were silver stained, Coomassie stained, or transferred to polyvinylidene difluoride (PVDF) membrane (BioRad). Proteins were detected on Western blot using a mixture of mouse anti-polyHistidine (Sigma) and mouse anti-Penta-His (Qiagen) as primary antibodies and Rabbit-anti-mouse-HRP (Dako) as the secondary antibody. The signal was detected using ECL (GE Healthcare).

Sample preparation for electron microscopy. For cryo-EM, PKG-NAIP5/NLRC4/FliC-D0$_L$ multimers (1.2 mg/ml) were incubated with protein conjugated 10 nm gold beads (donkey anti goat IgG, AURION). 4 µl sample was applied on EM grids, R1.21.3, Cu 200 mesh (Quantifoil), that had been glow discharged for 1 min at 30 mA and negative polarity using a K950X carbon coater (Emitech). After 3 s blotting with filter paper (Whatman 541) the sample was plunge-frozen in a liquid propane/ethane (2:1 v/v) mixture using an EM-GP (Leica) at room temperature and 95% humidity. In a similar way, concentrated poly-NLRC4 (5 mg/ml) was plunge frozen after short incubation with protein A conjugated 5 nm gold beads (UMC).
The NAIP5/NLRC4/FliC-D0$_L$ multimers, at a concentration of 0.3 mg/ml, were incubated with 20 µg/ml (mouse anti-Flag or rabbit anti-StrepII as primary antibody and protein A labeled with 5 nm gold beads for 20 minutes at 4°C and then applied on glow discharged EM grids, CF-2/1-2C (C-flat), blotted for 3 s and plunge frozen in liquid ethane using a Mark IV Vitrobot (FEI) at room temperature and 100% humidity.

Cryo-EM data collection. For all samples, data was collected using a NeCEN Titan Krios (FEI) TEM at 200 kV acceleration voltage and parallel illumination with a GATAN Quantum imaging filter (for single axis ET) or FEI Falcon direct electron detector (for dual axis ET and 2D EM), respectively. All tilt series were acquired with FEI Xplore3D and single projection images with FEI EPU software.

Cryo-ET of NAIP5/NLRC4/FliC-D0$_L$ multimers. Three dual axis tilt series at -7 micron defocus were acquired at an initial magnification of 18.000 x on a unbinned Falcon (FEI) direct electron detector, resulting in images with 4.82 Å pixel size at specimen level. A total electron dose of 50 $e^-/Å^2$ per was distributed over 57 images per half series applying a Saxton tilt scheme with initial increment of 3.

Cryo-ET of NAIP5-PKG/NLRC4FliC-D0$_L$ multimers. 16 low dose single axis tilt series of NAIP5-PKG/NLRC4/FliC-D0$_L$ multimers were acquired at -7 micron defocus using dose distribution and linear continuous tilt scheme with 2° increment between +/-66° resulting in tilt series comprising 67 images at final pixel size of 5.46 Å and a total electron dose of ~100 $e^-/Å^2$.

Single particle data collection of poly-NLRC4. In total 3.641 Images were acquired automatically on two different grid squares of the same grid, 5 images per hole at alternating defocus of -3 and -5 micron and using an electron dose of 10 $e^-/Å^2$. A nominal magnification of 37.000x resulted in a pixel size of 2.34 Å at specimen level.

EM data processing.

Reconstruction of single axis NAIP5-PKG/NLRC4/FliC-D0$_L$ tomograms and sub tomogram averaging. NAIP5-PKG/NLRC4/FliC-D0$_L$ single axis tomograms were reconstructed in IMOD (*32*). Images were aligned by patch tracking and low pass filtered to the first zero of the contrast transfer function (CTF) before applying simultaneous iterative reconstruction algorithm (SIRT) in five iterations. Of 16 tomograms the 7 best were selected for sub tomogram averaging. The CTF of these tomograms was corrected using IMOD *ctfphaseflip* after defocus estimation using TOMOCTF *tomoctffind* (*38*). The averages of central parts of the particles were calculated using the IMOD PEET software (*33*). Initially, 15 longest (seemingly helical) particles were extracted as sub tomograms and rotated in order to prealign the putative symmetry axis of the particles using a script based on IMOD *slicer* and *rotatevol*.

All 15 particles were independently checked for internal symmetry. First, helices were traced along the outer radius resulting in a first estimate for handedness and rise of the helix. Next, internal symmetric averages were created using 100 equally spaced positions along the symmetry axis of the helical particle as a starting model. Internally averages particles were visually inspected to confirm the handedness of the particle. We found 9 particles to be right handed, and 6 particles left handed. Although left and right-handed particles occurred in same tomograms, we confirmed reliability of all data processing steps to exclude the possibility of artificially introduced flipping of handedness. This was done by reconstruction of co-purified actin filaments imposing known symmetry parameters (fig. S1; (*39*)).

Left- or right handed class averages were calculated using PEET. For each particle an initial motive list with 100 reference coordinates –equally spaced along the symmetry axis- was produced with the program *stalkInit*. Before averaging each sub particle represented by these coordinates was randomly rotated around the putative symmetry axis, in order to reduce missing wedge bias. Averaging was performed in 10 iterations with decreasing translational and rotational step sizes (down to 1°) using a randomly chosen initial reference position, a disc shaped binary mask with 22 pixel height and 40 pixel radius which was created in SPIDER (*40*) and missing wedge compensation. For each new iteration, particles were aligned against an average comprising 5-10% of the best correlating particles. After three iterations without imposing symmetry, the symmetry axis was realigned and helical symmetry parameters were assessed for the right handed average (H5.57 Å,+30.9°,2,1) and imposed for all further iterations by creating a symmetrically averaged reference using a script based on Imod programs *rotatevol*, *newstack* and *clip*. The last iteration was guided by principle component analysis and unsupervised classification by k-means clustering. The final right handed average represented a cluster 50 protomers. Helix parameters could not be determined for the left handed class. Instead, mirrored right handed parameters (H5.57 Å,-30.9°,2,1) were assumed during refinement.

Averages of dimerizing NAIP5-PKG/NLRC4/FliC-D0$_L$ ends were calculated in a similar manner but without symmetry constraints. The final average after principle component analysis an k-means clustering comprised 53 particle ends.

Fourier shell correlation of two averages obtained by even-odd splitting of particles was performed for all unsymmterized averages (fig. S2-4). Additionally, resolution of symmetrized average of the right handed NAIP5-PKG/NLRC4/FliC-D0$_L$ was estimated after modeling by correlating this map with different down-sampled simulated density maps of the pseudo atomic model (fig. S7).

Reconstruction of dual axis NAIP5/NLRC4/FliC-D0$_L$ tomograms. Dual axis cryo-electron tomograms of NAIP5/NLRC4/FliC-D0$_L$ were reconstructed and merged in IMOD. Tilt series were locally aligned using fiducial tracking. Before tomogram reconstruction using five SIRT iterations, gold beads were removed from aligned tilt series and CTF was corrected by phase flipping after defocus estimation in TOMOCTF. The tomogram was low pass filtered and isosurfaces of representative particles were extracted and visualized using UCSF Chimera (*35*).
Averaging of dimerizing particle ends was carried out similarly as for NAIP5-PKG/NLRC4/FliC-D0$_L$, yielding in a final average comprising 44 particle ends.

*Modeling of the helical NAIP5-PKG/NLRC4/FliC-D0$_L$ multimer***.** Based on the final right handed helical average map of NAIP5-PKG/NLRC4/FliC-D0$_L$ and a manually fitted model of a complex-incorporated NLRC4 monomer, an optimized model for a helical NLRC4 polymer was created by iterative, symmetry imposed, simultaneous multi fragment docking using Situs (*34*) and UCSF Chimera. As input for the refinement, we created 25 additional, symmetry related protomers using the Chimera *sym* command and superposed this model with the ET average map. The NBD-HD1, WHD-HD2, and LRR fragments of each of the 26 symmetry-related molecules were locally refined as separate rigid bodies in one round of off-lattice Powell optimization using Situs *collage*. The central rod was masked out as the EBD was omitted from the refinement. Repeatedly a single protomer was selected, a new set of symmetry related NLRC4s created and refined in *collage*. After five iterations we obtained a model with an overall correlation of 78.5% in absence of the CARD domains.

SUPPLEMENTAL REFERENCES

36. Y. Durocher, S. Perret, and A. Kamen, High-level and high-throughput recombinant protein production by transient transfection of suspension-growing human 293-EBNA1 cells, *Nucleic acids research* **30**, e9 (2002).
37. A. Tsai, and R. P. Carstens, An optimized protocol for protein purification in cultured mammalian cells using a tandem affinity purification approach, *Nature protocols* **1**, 2820-2827 (2007).
38. J. J. Fernandez, S. Li, and R. A. Crowther, CTF determination and correction in electron cryotomography, *Ultramicroscopy* **106**, 587-596 (2006).
39. R. Dominguez, and K. C. Holmes,K.C., Actin structure and function, *Annual review of biophysics* **40**, 169 (2011).
40. J. Frank, M. Radermacher, P. Penczek, J. Zhu, Y. Li, M. Ladjadj, and A. Leith, SPIDER and WEB: processing and visualization of images in 3D electron microscopy and related fields, *Journal of structural biology* **116**, 190-199 (1996).
41. S.J. Ludtke, P.R. Baldwin, and W. Chiu. EMAN: semiautomated software for high-resolution single-particle reconstructions. *Journal of structural biology* **128**, 82-97 (1999).
42. M. A. Larkin, G. Blackshields, N. P. Brown, R. Chenna, P. A. McGettigan, H. McWilliam, F. Valentin, I. M. Wallace, A. Wilm, and R. Lopez, Clustal W and Clustal X version 2.0, *Bioinformatics* **23**, 2947-2948 (2007).

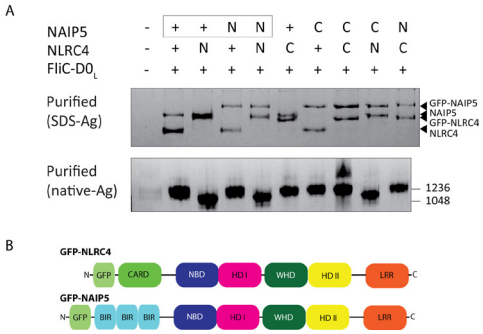

Fig. S1: NLR multimer formation in HEK293E cells transfected with the proteins indicated. A: Boxed proteins carry a StrepII$_3$-His$_6$ purification handle; "N" indicates that the protein is fused to GFP at its N-terminus, "C" indicates that the protein is fused to the GFP at its C-terminus. Purified protein was analysed by SDS-PAGE (top panel) or native PAGE (bottom panel, size markers on the right in kDa) followed by silver staining. Reduced weight of GFP-NLRC4 fusion constructs indicates impaired dimerization. B: Schematic of NLR constructs used in this experiment.

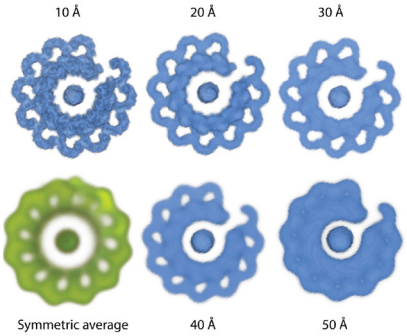

Fig. S2: Resolution estimation of right-handed helical NAIP-PKG/NLRC4/FliC-D0$_L$ sub tomogram average map. The final sub tomogram average map (volume rendering in green) is compared to our pseudo atomic model (blue), for which density maps were simulated at different resolution varying from 10 Å to 50 Å resolution. The average map correlates best with the 40 Å simulation. Maps were simulated using the UCSF chimera tool molmap which is based on EMAN program pdb2mrc (*41*).

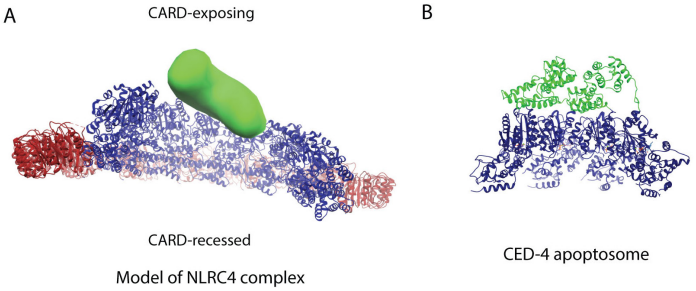

Fig. S3: Comparison of refined helical NLRC4 model and assembled CED-4 apoptosome reveals position of the CARD domains. Cartoon representation of half a turn of our optimized NLRC4 model (A) and the CED-4 apoptosome (B). LRRs are colored red, NACHT domains blue, and CED-4 CARD domains green. The approximate location of the CARDs with respect to our model of the NACHT and LRR domains is indicated by a green surface. This was created by positioning the Apaf-1 CARD domain (PDB ID 1Z6T) near the N-terminus of the NACHT domain of one protomer, generating the symmetry related CARDs for the other protomers, and finally calculating a density map at 20 Å resolution using UCSF Chimera.

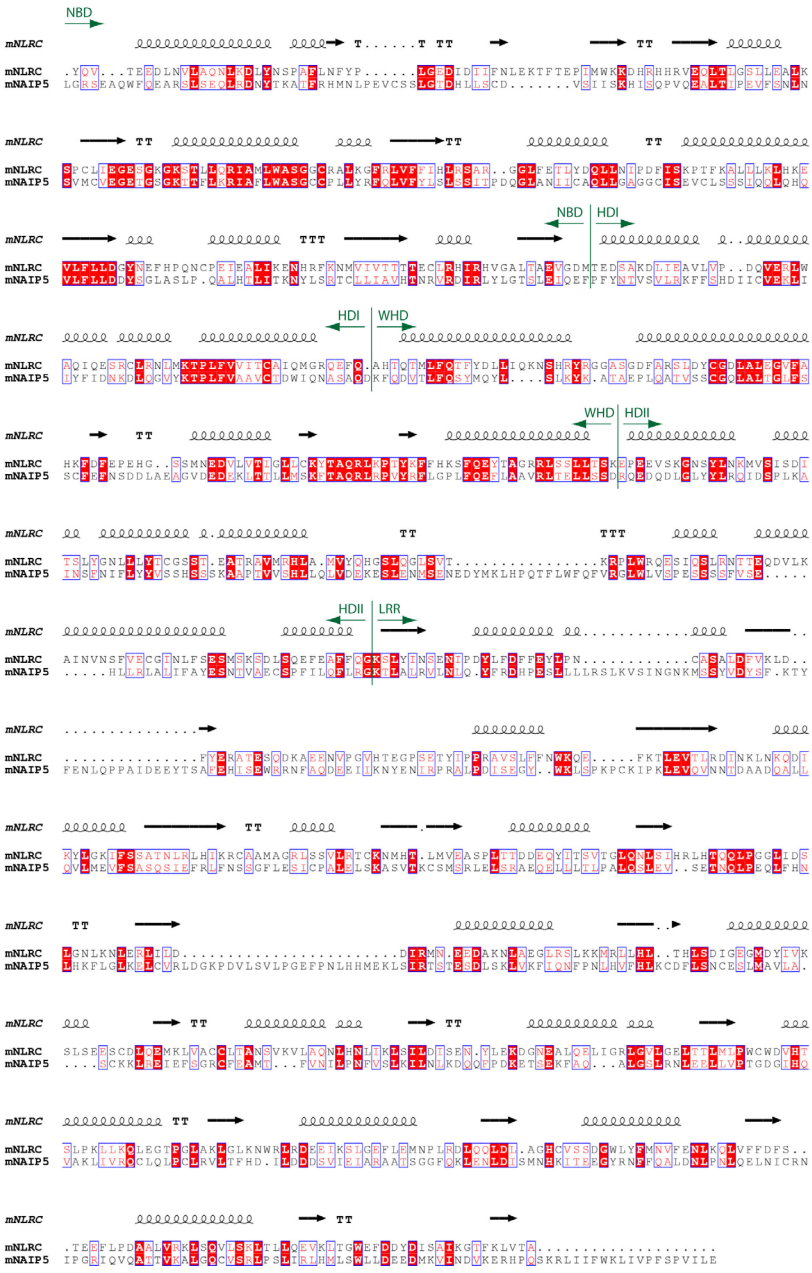

Fig. S4: Protein sequence alignment of murine NAIP5 and NLRC4. Sequences of the NACHT and LRR domains of murine NAIP5 (UniProt entry Q9R016) and murine NLRC4 (Q3UP24) were aligned using ClustalW2 (*42*). The secondary structure of NLRC4 is indicated at the top (PDB ID 4KXF). (Sub)domain boundaries on the basis of the NLRC4 crystal structure are indicated in dark green. The threshold for coloring is set to a similarity score of 0.7 based on the Risler matrix. On the amino acid level, the identity between NAIP5 and NLRC4 is 24.7% and the similarity is 34.2% based on the BLOSUM62 matrix.

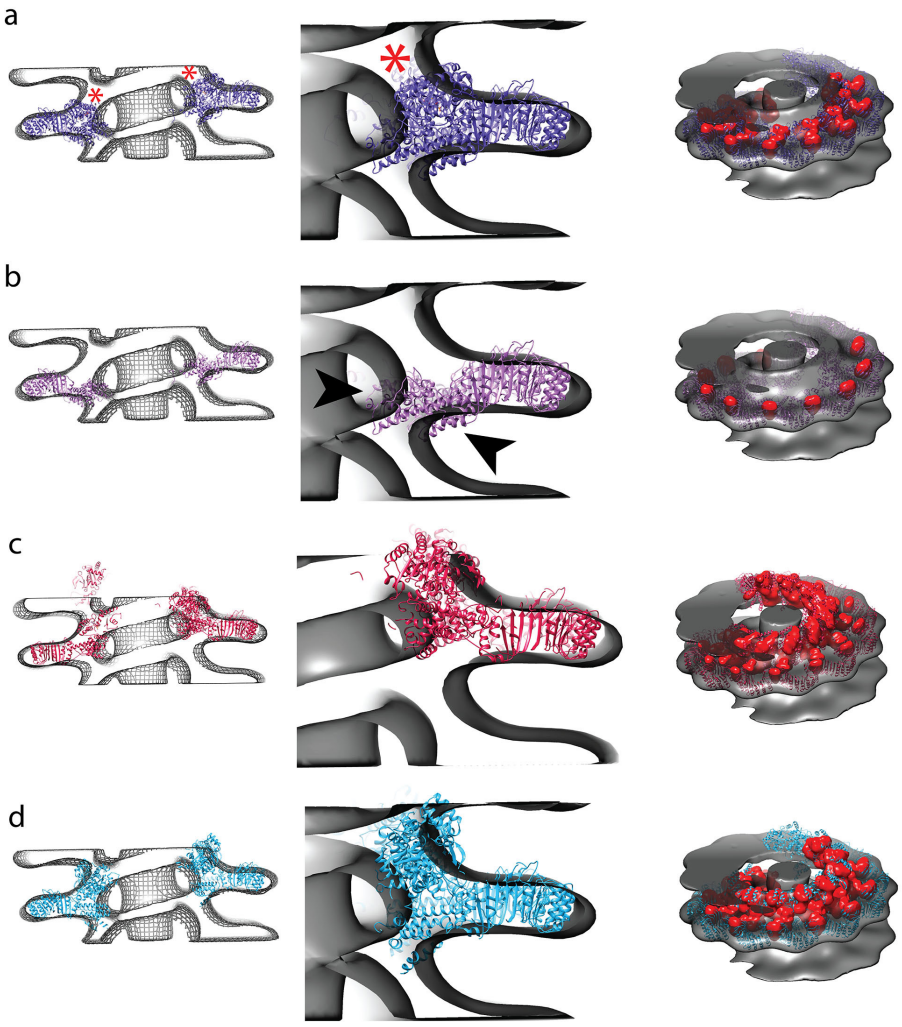

Fig. S5: Fitting attempts. Sagittal sections (left columns) and three-dimensional maps (right column) of several attempts of it the crystal structure of inactive NLRC4 into the EM density map. Red areas in the right column represent steric clashes. A: Fitting of the inactive NLRC4 structure (blue surfaces) into the EM density (meshed surface) guided by the placement of the LRR domains shows severe clashing at the NLRC4 interfaces (right, red surfaces) as well as unoccupied density in the EM map (red asterix). B: Fitting of the WHD-HD2-LRR fragment only already shows steric clashing (red surfaces) and the HD2 part protruding from the EM density (black arrowheads). C: Fitting of NLRC4 in which the WHD-HD2 and NBD-HD1 fragment have been rearranged into the same conformation as in apoptosome incorporated Apaf-1. D: Optimized fit of the NLRC4 with the WHD-HD2, LRR and the NDB-HD1 treated as separate rigid body fragments.

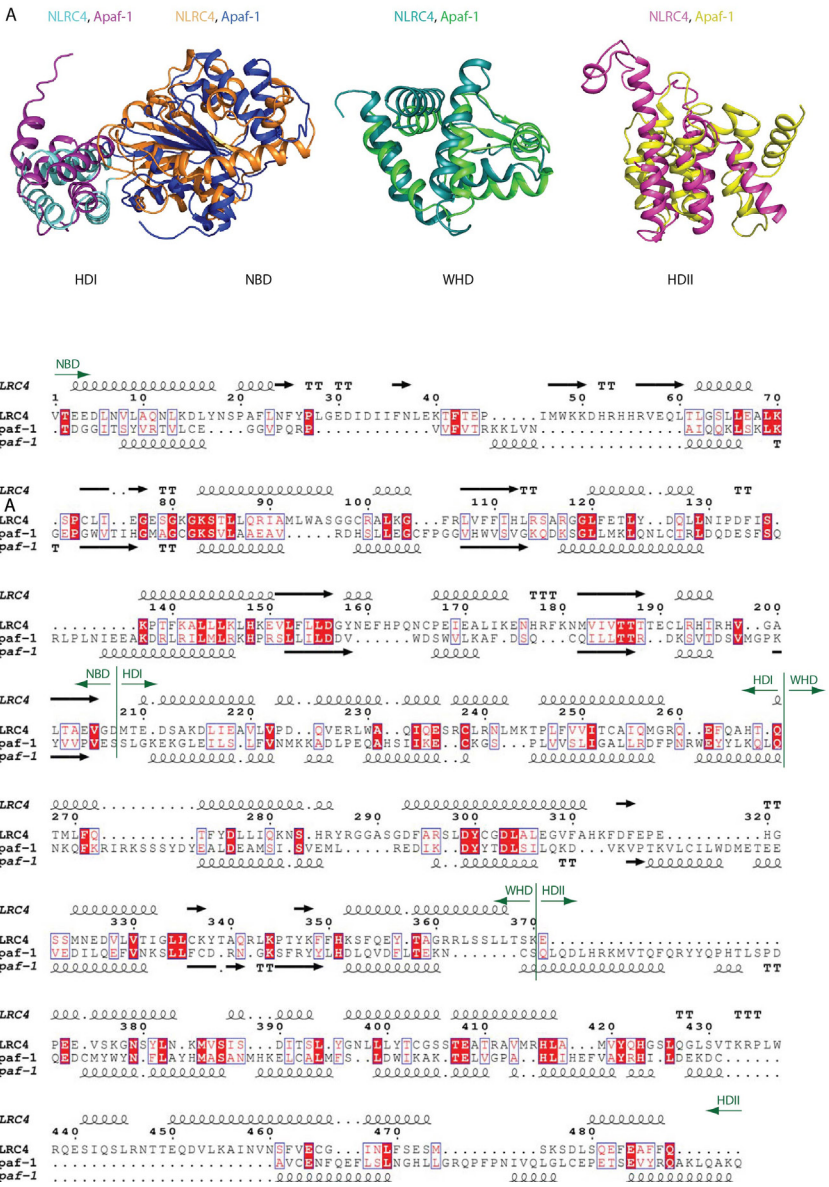

Fig. S6: Structure and sequence comparison of NLRC4 and Apaf-1 NACHT subdomains. A: Cartoon representation of superposed fragments of murine NLRC4 and human Apaf-1 NACHT domains (PDB ID 4KXF and 1Z6T, respectively). Color-coding is indicated at the top. B: Structure based protein sequence alignment of NACHT domains of murine NLRC4 (UniProt entry Q3UP24) and human Apaf-1 (UniProt entry O14727). The structures of the NACHT domains were manually aligned per domain in UCSF Chimera and the resulting sequence alignment was manually edited. The secondary structures of human murine NLRC4 and human Apaf-1 are indicated at the top and bottom, respectively. Subdomain boundaries as derived from the superposed crystal structures are indicated in dark green. The threshold for coloring was set to a similarity score of 0.7 based on the Risler matrix.

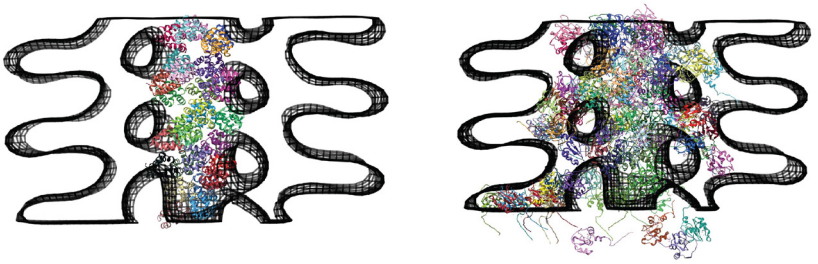

Fig. S7: Visualization of the fit of effector binding domains to the right-handed average map of NAIP5-PKG/NLRC4/FliC-D0$_L$. Central vertical cross sections through the helically symmetrized average map (meshed surface) with optimized fit of CARDs (A) of BIR domains (B) to the central rod density. The CARD and BIR domains were fitted without imposing helical symmetry. While CARDs can be accommodated in the central rod density, BIR domains are placed outside the rod. The figure was created using UCSF Chimera.

CHAPTER 4

Pushing the resolution limits in cryo-electron tomography of biological structures

Christoph A. Diebolder[1,2], Abraham J. Koster[2], and Roman I. Koning[2,*]

Journal of Microscopy, Vol **248**, 1-5 (2012)

[1]Crystal and Structural Chemistry, Bijvoet Center for Biomolecular Research, Department of Chemistry, Faculty of Science, Utrecht University, 3584 CH Utrecht, The Netherlands

[2]Department of Molecular Cell Biology, Section Electron Microscopy, Leiden University Medical Center, 2300 RC Leiden, The Netherlands

*Corresponding author

SUMMARY

Cryo-electron tomography is a three-dimensional imaging technique that is suitable for imaging snapshots of the structural arrangements of biomolecular complexes and macromolecules, both in vitro and in the context of the cell. In terms of attainable resolution, cryo-electron tomographic reconstructions now show resolvable details in the 5–10 nm range, connecting optical microscopy with molecular imaging techniques. In view of the current developments in super-resolution light microscopy and correlative light and electron microscopy, cryo-electron tomography will be increasingly important in structural biology as a tool to bridge light microscopy with molecular imaging techniques like NMR, X-ray diffraction, and single particle electron microscopy. In cell biology, one objective, often referred to as visual proteomics, is the molecular mapping of whole cells. To achieve this aim and to link cryo-electron tomography to these high-resolution techniques, increasing the attainable resolution to 2–5 nm is vital. Here, we provide an overview of technical factors that limit the resolution in cryo-electron tomography and discuss how, during data acquisition and image processing, these can be optimized to attain the highest resolution possible. Besides, existing resolution measurement approaches and current technological developments that potentially increase the resolution in cryo-electron tomography are discussed.

INTRODUCTION

Cryo-electron tomography (cryo-ET) is a three-dimensional imaging technique that is suitable for imaging biological structures with a resolution in the order of nanometres. With cryo-electron tomography, the three-dimensional shape of single and unique structures, such as macromolecular complexes, pleomorphic viruses, small bacteria and slices or thin areas of cells can be visualized (*1*, *2*). Cryo-electron tomography bridges the resolution gap between light microscopy and molecular imaging techniques, e.g. X-ray crystallography and single particle cryo-electron microscopy (Figure 1). In fluorescence light microscopy, fluorescently labelled molecular structures can be localized with high resolution, though the information about underlying structural arrangements and the cellular context is limited.

A powerful emerging application of cryo-electron tomography in the field of structural cell biology is the localization and direct visualization of vitrified macromolecular structures in a snapshot of their cellular context. In principle, this approach would enable the three-dimensional spatial mapping of molecules in the cell's interior. This application is sometimes referred to as visual proteomics (*3*). The basic idea is that available molecular models, which are determined by other techniques such as single particle electron microscopy, X-ray crystallography, NMR, are placed into the cryo-electron tomogram of the cell. The correct spatial location and orientation of these molecular models in the cellular context is determined by computational procedures, some of which are referred to as template matching or docking. From both experimental and theoretical work, it is concluded that the reliability and robustness of docking approaches becomes significantly higher when the resolution of the cryo-electron tomograms is sufficient to provide unambiguous structural clues. Some experimental data have shown that a resolution of 0.8 nm is sufficient to resolve the presence of α-helices in cryo-electron reconstructions providing sufficient information for high-resolution docking of macromolecules. Although that resolution cannot be obtained in cryo-ET for most

specimens, it is clear that technological developments are geared toward the highest possible resolution.

To obtain the highest possible resolution in electron tomography, it is essential to optimize the image acquisition parameters and image processing tools. In data acquisition, the most important factors are radiation damage, total electron dose, sample thickness and the the used tilt scheme. Of the required tomographic image processing steps, the alignment of the tilt series is crucial, whereas CTF correction and noise filtering are powerful tools to increase the contrast in noisy tomographic reconstructions. High-resolution models of in situ macromolecular complexes can be obtained by sub-tomogram averaging of identical structures, implicitly increasing the signal-to-noise ratio by averaging. Current technological approaches that are undertaken and have a positive effect on the attainable resolution are dual-axis tilt cryo-electron tomography, the use of direct electron detectors and the adaptation of the image formation process by incorporating phase plates. In

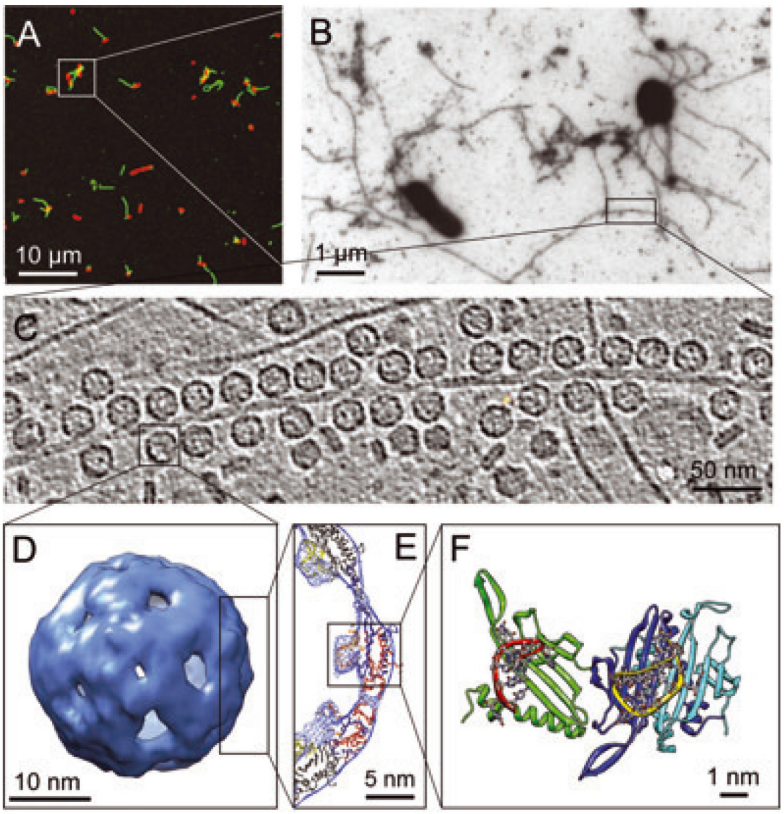

Figure 1. How cryo-electron tomography bridges the resolution gap between light microscopy and molecular imaging. A: Light microscopy image of fluorescently labelled *E.coli* cells (red) and pili covered with phages (green). From Daehnel *et al.*, (*4*). B: Low-magnification TEM image of negatively stained *E.coli*. C: Virtual section through a cryo-electron tomogram showing the F-pilus decorated with MS2 bacteriophages. D: Isosurface of the MS2 capsid after averaging of sub-tomograms in C. E: Docking of MS2 capsid X-ray structure (PDB 1ZDI) into an icosahedral single particle reconstruction. F: Closer view of the crystal structure showing genomic RNA (red and yellow) connected to capsid protein.

order to assess the quantitative effects these methodological and instrumentation developments have on resolving structural features, it has become increasingly important to define a quantitative measure for the resolution of cryo-electron tomograms and define a numerical indicator for their quality.
Here we give an overview of the parameters that affect resolution during data collection, point to some key topics in image processing and describe current approaches and methodologies to measure the resolution of cryo-electron tomograms.

PARAMETERS THAT INFLUENCE THE RESOLUTION DURING DATA ACQUISITION

Radiation damage, total electron dose and magnification. The main resolution limiting factor in cryo-electron tomography is the total electron dose that is used to acquire a tilt series. Increasing exposure of vitrified biological samples to the electron beam causes the breakage of covalent bonds that progressively leads to structural degradation. Therefore, the total electron dose that can be used for imaging is limited. Realizing that for high-resolution electron tomography the number of images composing the tilt series needs to be large to cover a wide angular range as finely as possible, the limited dose will have the inevitable consequence that the individual images in the tilt series are very noisy. For an optimal resolution, the total electron dose that is available to acquire a tilt series is a trade-off between an increase of the signal-to-noise ratio in the individual images and an increase of physical deterioration of the specimen.

The optimal magnification at which cryo-electron tomograms are recorded is determined by the desired resolution. At low magnification the field of view is larger, and when the electron dose to which the specimen is exposed is kept constant more electrons hit the detector, resulting in a higher signal-to-noise ratio per pixel. The minimal magnification is determined by the required image resolution. The magnification should be chosen such that the pixel size on the specimen level is small enough to properly sample the desired structural detail that needs to be resolved. Lower magnifications will lead to resolution loss due to undersampling, whereas oversampling will result in increased beam damage without any increase in resolvable detail. It should also be taken into account that the modulation transfer function (MTF) of detectors falls off at high spatial frequencies and that it can be more effective to acquire images with the individual pixels of the camera software or hardware binned into larger pixels, e.g. that four pixels contribute to one binned pixel that result in a more favourable signal-to-noise ratio. In practice, the pixel size at the level of the specimen should be chosen at least 4× smaller than the desired resolution.
The sensitivity of biological specimens to the electron beam depends on several other factors. Lower accelerating voltages increase electron-specimen interactions, leading to faster sample damage and simultaneously increase image contrast. To a minor extend, lower electron radiation dose rates, short exposure times and lower sample temperatures were reported to be advantageous for imaging. Also, biological structures with different composition and chemical bonds (e.g. proteins and RNA) can have different sensitivity to the electron beam, which can be observed by differences in radiation damage as a function of electron dose. In most cases, the total electron dose that is chosen depends on a combination of the biological structure and the desired resolvable details. To image structures that maintain their molecular integrity, the electron dose should not exceed

10^3 e/nm^{-2}. An electron dose in the order of 10^4 e/nm^{-2} can be used for imaging cellular structures, whereas 10^5 e/nm^{-2} can be used for membranous structures (*5*).

Sample thickness. The sample thickness is an important resolution determining factor in cryo-electron tomography. Upon increasing sample thickness, the relative amount of inelastically scattered electrons – which do not contribute to the high-resolution information in the image of the sample but add to the noise level in the image – increases, leading to lower signal-to-noise ratios (*6*). Therefore, the maximal achievable resolution in thick specimens is worse than in thin samples.

It is useful to express the sample thickness in terms of the mean free path of an electron transiting through the sample since it depends on the used acceleration voltage of the electron microscope and the material of the sample. The mean free path is described as the average distance between two consecutive scattering events of one electron. The mean free path of amorphous ice is about ~200 nm for 120 kV, ~270 nm for 200 kV and ~350 nm for 300 kV. Note that upon tilting an electron microscopy sample, typically having a slab geometry, the effective sample thickness increases with 1/cos (tilt angle) and the thickness increases up to 3× at 70°. In practical terms, cryo-electron tomography can be used for samples with a thickness up to 500 nm.

An electron energy filter can remove inelastically scattered electrons, allowing only elastically scattered electrons to pass through to the detector (zero-loss imaging). This will effectively increase the signal-to-noise level in the images. Zero-loss imaging is very useful in cryo-electron tomography, especially when thick samples are imaged. Although in theory resolutions can be achieved ranging from 2 nm in samples that are not thicker than ~100 and 10 nm in ~500 nm thick samples, in practice the resolution appears to be a factor of 2–5 worse.

Data collection tilting geometry and number of images. The data collection tilting geometry is an important factor that influences the resolution. It has been determined that a minimal number of projection images is needed to fully sample an object in Fourier space to achieve a certain resolution (*7*). For noise-free images of a spherical sample, the maximal resolution (r) that can be attained is determined by a combination of the sample thickness (D) and the angular tilt increment (α_0, in radians) and is given by $r=D\alpha_0$. In practice, for electron tomography the resolution will be worse since images of vitrified samples are noisy, samples have slab geometry and the effective thickness of the sample increases with tilt angle. To overcome this latter effect, tilt geometries with decreasing angular increments at higher tilts were developed (*8*).

Since vitrified samples that have slab geometry are supported by a metal grid and are mounted inside a cryo-holder, they cannot be imaged over the full angular range, but instead are imaged over a smaller range, typically ranging from +60° to −60°. This implies that the object is not completely sampled in Fourier space and a missing data wedge exists. The combination of incomplete sampling and rotation along one axis results in an anisotropic resolution within the tomographic reconstruction, being worst in the direction of the electron beam and best along the tilt axis.

To reduce this anisotropy, a second tomographic tilt series can be recorded of the feature of interest along an axis perpendicular to the first tilt series. The combination of the two series reduces the missing data wedge in Fourier space into a missing data pyramid and improves the resolution in the direction orthogonal to the primary tilt axis. The application of dual tilt cryo-tomography will require that the total electron dose per tilt series is halved. In addition, the quality of the combined tomogram will rely on how well the two tomograms can be combined (e.g. aligned to each other).

GETTING THE BEST RESOLUTION FROM IMAGE PROCESSING

Image alignment. The alignment of the individual images in the tilt series is crucial for a high quality three-dimensional reconstruction. Inaccurate alignment will result in the blurring of features and in lower signal-to-noise levels and lower resolution of the final tomogram. The image contrast, generated by the electron-beam interaction with frozen hydrated cellular structures that are composed of light elements, in the individual images of a tilt series will be very low. Therefore, in many cases, to facilitate the alignment of the tilt series strongly electron-scattering nano-sized gold particles are added to the sample prior to vitrification, that are used as fiducial markers. Fiducials are generally used in cryo-electron tomography and result in good alignments. The alignment and distortion corrections are performed by three-dimensional modelling of the fiducial positions. The use of fiducials also allows refinement and correction of a variety of image distortions, including image rotations, changes in magnification and tilt angle. Besides, fiducial-less alignment procedures are used which are based on cross-correlation between the individual images of the tilt series. It should be stressed that the fiducials, and not the sample itself, are used for the alignment and that their proximity to the reconstructed object is of influence to the alignment accuracy.

CTF correction. Image formation in cryo-electron microscopy on frozen-hydrated biological specimens can be mathematically described by the contrast transfer function (CTF), which includes a number of parameters such as defocus, astigmatism, beam coherence and energy spread. This is of importance as in tomographic tilt series the defocus value varies largely, both within one (tilted) image and between the different images of the tilt series. The defocus will increasingly vary in areas further away from the tilt axes, whereas on the tilt axis it will remain constant. The shape of the CTF depends on the actual defocus. Identical structural features can exhibit a different appearance when imaged at a different defocus. In most cases, lower resolution features are much less affected. To recover higher resolution structural information correctly from the acquired images, it is essential to correct for the defocus-dependent contrast changing effects of the CTF (9). Therefore, the CTF correction process is very important for high-resolution imaging, e.g. when sub-tomogram averaging methods are applied.

Denoising/Filtering. Noise reducing filtering is frequently used in a cryo-electron tomogram to increase the signal-to-noise ratio for visualization and segmentation purposes. Low pass filtering, for a frequency range higher than the attained resolution, can be applied to reduce the noise level in the tomogram for improved visualization of structural features. Furthermore, non-linear anisotropic diffusion filters are used that incorporate the local shape of the structural element in

the reconstruction into account. Local features that show high contrast will be enhanced and areas that exhibit low contrast will be blurred. The extend of filtering depends heavily on the sample, the biological question and on the resolution of the tomogram. When used properly, this might lead to a slight improvement of resolution due to the increase of contrast, though comparison with the unfiltered tomogram remains essential to avoid drawing conclusions from filtering artefacts.

Sub-tomogram averaging. Although cryo-electron tomography is most suitable for imaging unique structures, it can also be applied to samples that contain multiple copies of (nearly) identical sub-structures, e.g. ribosomes in a cell. The resolvable details of these sub-structures can be improved by averaging, which improves the signal-to-noise ratio and isotropy of the data and therefore the resolution. The resulting resolution depends on the number of particles and on the particle alignment and classification quality prior to averaging. For cryo-electron tomography applications where sub-tomogram averaging is not envisioned, a relatively large defocus is chosen (~8 µm) to emphasize the spatial frequency range of 4 nm and less. For sub-tomogram averaging, in most cases, a higher resolution is aimed for and a lower defocus value has to be chosen (~2 µm). Low defocus values result in higher resolutions in non CTF corrected sub-tomogram averaged reconstructions.

MEASURING THE RESOLUTION IN CRYO-ELECTRON TOMOGRAMS.

Despite much progress in cryo-ET, quantitative assessment of the attained resolution in tomograms has remained a challenging issue. In electron tomography, the resolution is not limited by the resolving power of the imaging system (the transmission electron microscope lenses and the imaging detector) but more by the nature and characteristics of the specimens, the signal-to-noise level, the precision and robustness of the alignment as well as sub-tomogram averaging procedures. Therefore, in electron tomography, resolution measurements are not based on the Rayleigh criterion, as used in light microscopy, but rather are self-consistency measurements of noisy electron microscopy datasets. In addition, compared to resolution measurement approaches developed for single particle electron microscopy, the situation for electron tomography is less straightforward. One of the recurring limitations is that tomography data is non-redundant, since there is only one projection available per tilt angle. Another limitation lies in the fact that the data is incomplete, due to the missing wedge and the limited amount of angular increments leading to both anisotropic data coverage and resolution in the dataset.

Several methods and theories have been put forward to assess the resolution in cryo-electron tomography – with theirs own advantages and disadvantages. Some theoretical approaches are based on the estimation of the spectral signal-to-noise ratio (*10*,*11*). In practice, there are two criteria that can be used to assess the quality of a tomographic reconstruction (*12*).

The first method computes the Fourier shell correlation of two tomograms that are generated from the even and odd split images of one tilt series ($FSC_{e/o}$). This method resembles the resolution measurements that are applied in single particle electron microscopy. The disadvantage is that only half of the dataset is used for comparison and hence, the signal-to-noise ratio is decreased. When the number of projections is the resolution limiting factor, the resolution is underestimated with a factor of two.

The other method is the noise compensated leave-one-out (*NLOO*) method that compares one of the original images from the tilt series with the appropriate reprojection from the tomogram that is computed from the remaining images of the tilt series, using Fourier ring correlation. Since the noise levels in one individual image from the tilt series is different from the calculated projection from the rest of the tomograms (minus the one image), the noise levels have to be compensated for this. When the tomograms are noise limited, both methods are mutually consistent. However, *NLOO* provides a more reliable criterion when the tilt increment becomes a significant factor. The *NLOO* is computationally more expensive than the $FSC_{e/o}$, but has the advantage that the resolution can be assessed as a function of the tilt angle.

THE PROSPECTS OF FUTURE INSTRUMENTATION

Currently, the two promising instrumentation developments – with a potentially vast impact on the resolution in cryo-electron tomography – are direct electron detectors and phase plates. The detectors used on electron microscopes are CCDs (charge coupled devices) that detect photons, which are generated by electrons that hit a scintillator on top of the CCD. The detection of electrons is indirect and less efficient. Direct electron detectors detect electrons more efficiently and will improve the signal-to-noise ratio per image.

Another development is geared towards the incorporation of phase plates in electron microscopes to overcome the resolution limiting effects described by the contrast transfer function. Their implementation into cryo-electron microscopy has been reported, but is not commercially available yet. A phase plate is a device that shifts the phase of the scattered electron beam compared to the unscattered beam. Consequently, the intensity of the image is related to the phase of the wave. As a result, with a phase plate incorporated, images can be recorded in focus, phase changes due to the defocus of the objective lens are absent, and the contrast transfer over the whole resolution range is more uniform. The use of phase plates in tomography EM will allow imaging at low defocus values without the need of CTF correction, resulting in images that contain both high-resolution information as well as low-resolution information that is required for the alignment of a tilt series (*13*).

Furthermore, resolution improvements can also be obtained by new single particle reconstruction approaches for studying single particles using cryo-electron tomography (*14*) and by improving the yield of tomographic acquisition by software automation (*15*) in combination with suitable high-end electron microscopes. The prospect of imaging biological specimens with a combination of an energy filter, direct electron detector and a phase plate with current high-end electron microscopes provides a positive prospect on improving the resolution in cryo-electron tomography that will result in sufficient structural information to dock high-resolution models of macromolecular structures within cryo-tomograms of cellular structures.

REFERENCES

1. O. Medalia, I. Weber, A. S. Frangakis, D. Nicastro, G. Gerisch, and W. Baumeister, Macromolecular architecture in eukaryotic cells visualized by cryoelectron tomography, *Science* **298**, 1209–1213 (2002).
2. R. I. Koning, and A. J. Koster, Cryo-electron tomography in biology and medicine, *Ann. Anat.* **121**, 427–445 (2009).
3. S. Nickell, C. Kofler, A. P. Leis, and W. Baumeister, A visual approach to proteomics, *Nat. Rev. Mol. Cell Biol.* **7**, 225–230 (2006).
4. K.Daehnel, R. Harris, L. Maddera, and P. Silverman, Fluorescence assays for F-pili and their application, *Microbiology* **151**, 3541–3548 (2005).
5. JR. Grimm, H. Singh, R. Rachel, D. Typke, W. Zillig, and W. Baumeister, Electron tomography of ice-embedded prokaryotic cells, *Biophys. J.* **74**, 1031–1042 (1998).
6. A. J. Koster, R. Grimm, D. Typke, R. Hegerl, A. Stoschek, J. Walz, and W. Baumeister, Perspectives of molecular and cellular electron tomography, *J. Struct. Biol.* **120**, 276–308 (1997).
7. R. A. Crowther, D. J. DeRosier, and F. R. S. Klug, The reconstruction of a three-dimensional structure from projections and its application to electron microscopy, *Proc. Roy. Soc. Lond. A.* **317**, 319–340 (1970).
8. W. O. Saxton, and W. Baumeister, Three-dimensional reconstruction of imperfect two-dimensional crystals, *Ultramicroscopy* **13**, 57–70 (1984).
9. J. J. Fernández, S. Li, and R. A. Crowther, CTF determination and correction in electron cryotomography, *Ultramicroscopy* **106**, 587–596 (2006).
10. P. A. Penczek, Three-dimensional spectral signal-to-noise ratio for a class of reconstruction algorithms, *J. Struct. Biol.* **138**, 34–46 (2002).
11. M. Unser, C. O. S. Sorzano, P. Thévenaz, S. Jonić, C. El-Bez, S. DeCarlo, J. F. Conway, and B. L. Trus, Spectral signal-to-noise ratio and resolution assessment of 3D reconstructions, *J. Struct. Biol.* **149**, 243–355 (2005).
12. G. Cardone, K. Grunewald, and A. C. Steven, A resolution criterion for electron tomography based on cross-validation, *J. Struct. Biol.* **151**, 117–129 (2005).
13. R. Danev, S. Kanamaru, M. Marko, and K. Nagayama, Zernike phase contrast cryo-electron tomography, *J. Struct. Biol.* **171**, 174–81 (2010).
14. L. Zhang, and G. Ren, IPET and FETR: experimental approach for studying molecular structure dynamics by cryo-electron tomography of a single-molecule structure, *PLoS One* **7**, e30249 (2012).
15. C. Suloway, J. Shi, A. Cheng, J. Pulokas, B. Carragher, C. S. Potter, S. Q. Zheng, D. A. Agard, and G. J. Jensen G.J., Fully automated, sequential tiltseries acquisition with Leginon, *J. Struct. Biol.* **167**, 11–18 (2009).

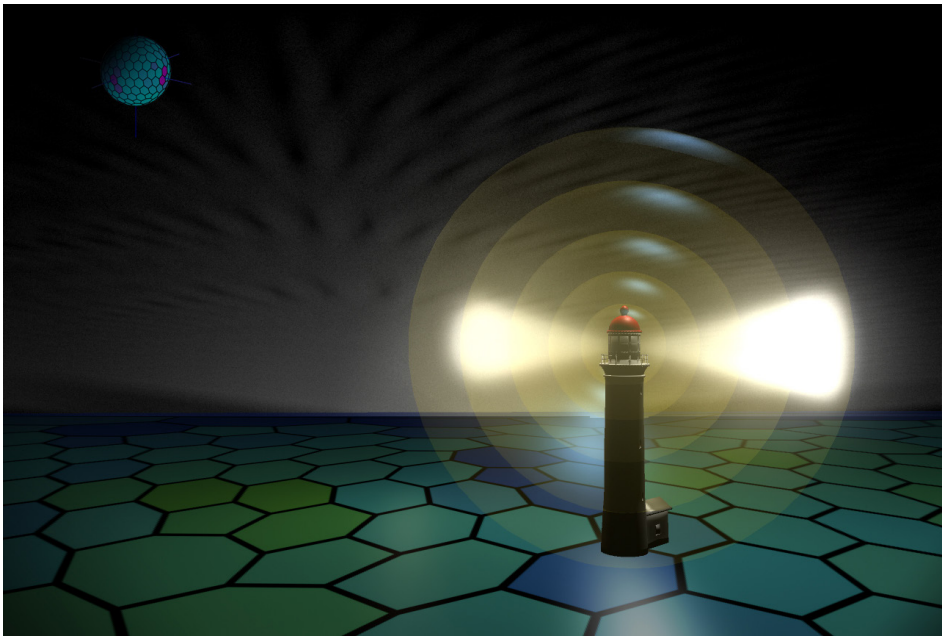

(C) R.I.Koning

CHAPTER 5

Conical Fourier Shell Correlation Applied to Electron Tomograms

Christoph A. Diebolder[1,2], Frank G.A.Faas[2], Abraham J. Koster[2], and Roman I. Koning[2,*]

Journal of Structural Biology, Vol **190**, 215-223 (2015)

[1]Crystal and Structural Chemistry, Bijvoet Center for Biomolecular Research, Department of Chemistry, Faculty of Science, Utrecht University, 3584 CH Utrecht, The Netherlands.

[2]Department of Molecular Cell Biology, Section Electron Microscopy, Leiden University Medical Center, 2300 RC Leiden, The Netherlands.

*Corresponding author

ABSTRACT

The resolution of electron tomograms is anisotropic due to geometrical constraints during data collection, such as the limited tilt range and single-axis tilt series acquisition. Acquisition of dual axis-tilt series can decrease these effects. However, in cryo-electron tomography, to limit the electron radiation damage that occurs during imaging, the total dose should not increase and must be fractionated over the two tilt series. Here, we set out to determine whether it is beneficial to fractionate electron dose for recording dual-axis cryo-electron tilt series or whether it is better to perform single-axis acquisition. To assess the quality of tomographic reconstructions in different directions, we introduce conical Fourier shell correlation ($cFSC_{e/o}$). Employing $cFSC_{e/o}$, we compared the resolution isotropy of single-axis and dual-axis (cryo-)electron tomograms using even/odd split data sets. We show that the resolution of dual-axis simulated and cryo-electron tomograms in the plane orthogonal to the electron beam becomes more isotropic compared to single-axis tomograms and high-resolution peaks along the tilt axis disappear. $cFSC_{e/o}$ also allowed us to compare different methods for the alignment of dual-axis tomograms. We show that different tomographic reconstruction programs produce varying anisotropic resolution patterns in dual-axis tomograms. We anticipate that $cFSC_{e/o}$ can also be useful for comparisons of acquisition and reconstruction parameters, and different hardware implementations.

INTRODUCTION

Electron beam damage and total electron dose are limiting the resolution in cryo-electron tomography. Cryo-electron microscopy (cryo-EM) has the primary advantage that vitrification, the fixation technique being used for specimen preparation, excellently preserves biological structures and consequently enabling atomic resolution data to be obtained (*1*,*2*). Though preservation is excellent, its main limitation is that vitrified biological specimens are highly sensitive to electron beam exposure, which increases radiation damage leading to the loss of structural integrity. Therefore, images are therefore recorded using a limited total electron dose, resulting in data with low signal-to-noise ratio (SNR). The total dose used during data collection ultimately limits the resolution of cryo-EM reconstructions. In single particle analysis (SPA) as well as in electron crystallographic techniques, data, resulting from a large number of identical objects, are averaged, which increases the resolution of the final reconstructed object without increasing electron beam induced radiation damage. Electron tomography (ET) generally targets uniquely shaped objects for which averaging is not possible. In practice, the total electron dose used to expose the targeted object in a tomographic tilt series is ~5 times higher than that of an individual image used in SPA. Therefore, electron radiation damage is often the main resolution limiting factor (*3*).

Fourier shell correlation for resolution estimation in cryo-EM. In SPA, Fourier shell correlation (FSC) is often used as a measure for the resolution. In short, datasets are split in two and subsequent shells in Fourier space, from each normalized half, are correlated with each other (*4*,*5*). FSC resolution measurement, which is rather an internal consistency assessments of reconstructions, is the 3D equivalent of the Fourier Ring correlation (FRC; *6*,*7*):

$$FSC_{1,2}(r_i) = \frac{\sum_{r_i} F_1(r_i) * F_2(r_i)^*}{\sqrt{\sum_{r_i} F_1^2(r_i) * \sum_{r_i} F_2^2(r_i)}} \qquad \text{(I)}.$$

Where r_i is the voxel element in Fourier space at radius r, $F_1(r_i)$ the complex structure factors of volume 1, and $F_2(r_i)^*$ the complex conjugate of the structure factor of volume 2. FSC is directly linked to the spectral signal-to-noise ratio (SSNR; *8*)

$$SSNR \cong \frac{FSC}{1 - FSC} \qquad \text{(II)}$$

and widely used for resolution estimation of SPA reconstructions (*9*). For the FSC measurement, the reconstructed volumes from two half sets are compared. Assuming a 50% decrease of the SNR for each half set compared to the full data set, it can be compensated for the resulting underestimation of resolution by defining a modified "ideal" FSC' (*10*) which has following relation to the measured $FSC_{measured}$:

$$FSC' = \frac{2FSC_{measured}}{FSC_{measured} + 1} \qquad \text{(III)}.$$

In practice, a number for the attained resolution of a reconstructed volume is often defined as the highest frequency for which the correlation coefficient remains above a certain threshold value. For instance, SSNR=2.0, according to (II) and (III), would correspond to a measured $FSC_{measured}$=0.5 and a FSC'=0.66, although other criteria are also used and discussed (*11,12*). This FSC was implemented for quality estimation of single-axis cryo-electron tomograms in the software package *ELECTRA* (*13*), assuming that Eq. (III) stays valid when splitting a tomographic tilt series into two (even and odd) half series:

$$FSC_{e/o} = \frac{2FSC_{measured}}{FSC_{measured} + 1} \qquad \text{(IV)}.$$

However, due to high noise levels and restricted geometry of data acquisition, interpreting measurements on tomograms is challenging.

Electron tomography data acquisition geometry influences resolution isotropy. The angular range for collecting images of the object of interest is inherently limited in electron tomogrpahy. The restricted data acquisition geometry leads to anisotropic resolution, as it causes inhomogeneous sampling of the object in the frequency domain. In many cases, the restricted geometry is due to the slab-like shape of the transmission electron microscope specimen that contains the object which limits the maximal angular tilt range for which images can be acquired. The number of views within that tilt range is limited because of the maximal allowable electron dose. For practical reasons, cryo-ET is usually performed by restricted tilting along a single fixed rotation axis, resulting in a missing data wedge in Fourier space (Fig. 1A). As a consequence, the resolution that can be obtained by single-axis tilt electron tomography is not isotropic and deteriorates in the

direction of the electron beam and, to a lesser extent, in the direction orthogonal to the tilt axis and the electron beam (*3*). Dual-axis tomography (*14*) and conical tomography (*15*) were proposed to increase isotropy by reducing the missing wedge of a single tilt tomogram to a missing pyramid or a missing cone, respectively (Fig. 1B and 1C). The latest generation of transmission electron microscopes and sample grid holders allow recording of tilt series with dual-axis tomographic geometries (*16*), but these methods are rarely applied to vitrified samples (*17*,*18*,*19*,*20*). One of the reasons is closely linked to the electron dose sensitivity of the specimen. For vitrified specimens, the total electron dose to which a specimen can be exposed without inducing radiation damage in the resolution range aimed for by the experiment is limited. Therefore, when recording a second perpendicular tilt series, the total electron dose has to be divided over two tilt series. For choosing the optimal data collection geometry a number of questions arise: Given that dual-axis reconstruction requires additional alignment of the two halve datasets, is recording a dual-axis tilt series more advantageous than recording a single tilt tomographic series (*21*, *22*)? Also, what is the most advantageous way to reconstruct dual-axis tilt series into a single tomogram? Should schemes be used based on independent single-axis tilt series alignments followed by merging of the reconstructed single-axis tomograms (*23*,*24*), or is common alignment of all projection images of both tilt series prior to back projection more advantageous (*25*,*26*)?

Estimation of resolution isotropy. Several methods are described that provide means to assess the quality of cryo-electron tomograms. In the *ELECTRA* software suite, a method called *NLOO*, is implemented which is based on FRC between a projection image of a tilt series and the corresponding re-projection that is obtained from a reconstruction omitting this projection. This leads to resolution measurements for the individual tilt angles in a data set. Two other methods exist that are based on measurement of the three-dimensional spectral signal-to-noise ratio (3D SSNR; *27*,*28*). Real space estimation of the point spread function has also been implemented (*29*). Nevertheless, FSC is still used for comparison of overall resolution for the different tomography geometries (*13*,*15*,*26*).

In order to assess resolution in a directional way, segmentation of the Fourier space has been introduced. Fourier space can be split into "sectors" as a function of elevation from the horizontal plane (Fourier sector correlation; *23*), and Penczek and Frank (*30*) defined a "resolution cone" along the tilt axis which contains redundant information and consequently can be used for SSNR measurement.

In this study, we investigate to what extent the use of dual-axis geometry increases the isotropy and the resolution of cryo-electron tomograms. Therefore, we developed "conical Fourier shell correlation of even-odd split tomograms" ($cFSC_{e/o}$). $cFSC_{e/o}$ is based on a modified even-odd Fourier shell correlation ($FSC_{e/o}$) and – besides general resolution estimation – allows directional resolution assessment in an electron tomogram. The $cFSC_{e/o}$ is computed within double-sided cones that have distinct orientation, sampling the entire Fourier space (Fig. 1D-F). We applied $cFSC_{e/o}$ as a directional measure for the resolution in single- and dual-axis electron tomograms of vitrified lipid vesicles with bound antibodies, and compare these with simulations of similar data acquisition geometries. We also used dual-axis tomograms of stained plastic sections to evaluate different reconstruction programs. Our results show that the isotropy of the resolution in the *XY*-plane (in directions orthogonal to the electron beam) in dual-axis tomograms is clearly enhanced

compared to single-axis counterparts, recorded using the same total electron dose. Comparison of various commonly used software implementations for tomographic data reconstruction shows that the implementation of the merging procedures for dual-axis tilt series influences the resolution isotropy as well as the achieved maximum resolution.

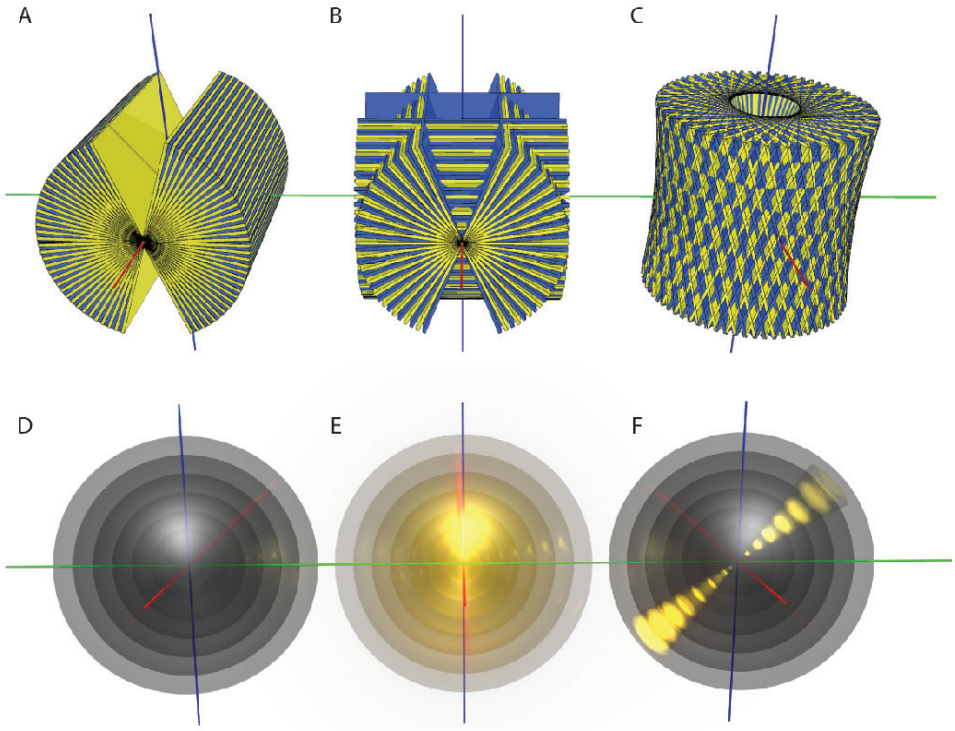

Figure 1: Tilt geometries and directional resolution estimation in electron tomography. Filling of Fourier space with projection planes for (A) single-axis, (B) dual-axis, and (C) conical tilt geometry. The geometries show differences in shape and size of missing areas (wedge, pyramid, and cone) and differences in plane spacing (smallest close to a tilt axis, most regular for conical geometry). The coordinate axes indicate the electron beam direction (blue) and – if applicable – the primary (red) and secondary tilt axis (green). Alternating coloring (blue and yellow) of planes indicates "even" and "odd" data splitting for FSC based resolution estimation. (D) Division of Fourier space into shells, representing different frequencies. (E) $FSC_{e/o}$ measures the correlation between even and odd data sets within each frequency shell and allows global resolution estimation. (F) $cFSC_{e/o}$ measures directional resolution by sampling Fourier space in conical sub volumes (yellow beam cone).

MATERIALS AND METHODS

Sample preparation. Outer membrane vesicles of the bacterium Neisseria meningitidis were purified as described previously (*31*) and incubated with IgG antibodies against PorA. Protein A-labeled gold beads (UMC Utrecht) of 5 nm diameter were added as fiducial markers. After incubation for 150 min at RT the sample was applied to glow-discharged 300 mesh Cu grids with a lacey Formvar/carbon support film (TedPella, #01883) and immediately vitrified by plunge freezing in liquid ethane using the FEI Vitrobot Mark IV (95% humidity, RT, 2 s blotting time, Whatman No.4 blotting paper).

Tomogram data collection and simulation. Dual-axis cryo-ET was performed on a FEI Titan Krios electron microscope being equipped with an FEG and operated at 200 kV and liquid nitrogen temperature. Images were recorded using a 4k x 4k Eagle CCD camera. Tomographic tilt series were collected under low dose conditions at nominal -5 micron defocus using FEI Explore3D with a nominal magnification of 14,000 x resulting in a pixel size of 0.63 nm at the specimen level. The images were recorded using an electron dose rate of 1 $e^-/(Å^2s)$, exposure times of 1 s per image and a linear tilt scheme ranging from 70° to -70° with constant 1° increment and dose distribution, resulting in a total electron dose of 282 $e^-/Å^2$. Simulated dual tilt series were generated using the MATLAB toolbox DIPimage (*32*) by projecting model samples (spherical vesicles and fiducial markers) and by adding Gaussian noise (σ=10) to each projection. Dual-axis tilt series of insect flight muscle were used as provided by the *Protomo* dual-axis reconstruction tutorial (version 2.3.1; *25*,*33*).

Tilt series alignment and tomogram reconstruction. Single- and dual-axis tomograms of simulated and recorded tilt series of vitrified liposomes were reconstructed with *IMOD* (*34*). With *IMOD*, the tilt series were locally aligned using ~100 gold beads per tomogram. For CTF correction by phase flipping, defoci were estimated by strip-based periodogram averaging using TOMOCTF (*35*). Gold beads were removed from aligned image stacks. After weighted back projection of the separate single tilt series, the two resulting tomograms were merged based on models of corresponding gold fiducials as well as patch correlation (*23*). The merged tomogram was denoised by nonlinear anisotropic diffusion filtering (*36*) in order to create sufficient contrast for manual selection of areas suitable for directional resolution measurements.
Tomograms of insect flight muscle were initially reconstructed in three independent workflows for comparison of dual-axis alignment procedures. (i) Tomograms were generated by *IMOD* using separate single-axis alignment by patch tracking, reconstruction by weighted back-projection and subsequent merging based on matching models (Supplemental Fig.S1C). (ii) The same single-axis tomograms were merged in real space using the FEI *Inspect3D* software (version 3.0; *24*). (iii) The dual-axis tomogram was reconstructed with the *Protomo* software package (version 2.4.1; *25*) using marker free simultaneous dual-axis tilt series alignment (Supplemental Fig. S1E).
The *IMOD* and *Protomo* workflows were subjected to in-depth comparison by introduction of hybrid reconstruction approaches. For this, tilt series alignments were carried out in *Protomo* omitting corrections for specimen orientation and beam tilt. Subsequently, reconstructions were

completed in *IMOD* in three different ways. (i) Single-axis tomograms were aligned to each other using matching model based tomogram registration and warping of the secondary to the primary tomogram. Following this, tomograms were merged using default *IMOD* weighting parameters. (ii) Alternatively, tomogram registration and warping were omitted, enforcing transformations known from simultaneous *Protomo* alignment. Again, default merging parameters were used. (iii) Lastly, warping was omitted and merging parameters were adapted in order to allow full amplitude weighting during averaging.

Estimation of resolution isotropy by cFSC$_{e/o}$. For resolution measurements of the single and dual-axis tomograms, tilt series were split in two halves, containing the even or odd numbered projection images. The tomograms were subsequently reconstructed, creating two reconstructions ("even" and "odd") from one tilt series with the same total electron dose and similar sampling of Fourier space (Supplemental Fig. S1B, D and F). In order to obtain comparable dose levels between a single-axis and the combined dual-axis tomograms, every second image was omitted in the dual-axis reconstructions.
Here, we define the Fourier shell correlation as

$$FC_i = \frac{\sum \hat{\omega}_i F_1 F_2^*}{\sqrt{\sum \hat{\omega}_i F_1 F_1^* \sum \hat{\omega}_i F_2 F_2^*}} \qquad \text{(V)},$$

where F1 and F2 are the Fourier transforms of their respective volumes and ŵi gives the contributing weight for each voxel for the ith measurement. Where $\hat{w}$ is the normalized version of the weight function *w*. Equation (V) reduces to the well-known FSC for the weight function:

$$\omega_i(f) = \begin{cases} 1, & if \quad f_i^- < f \le f_i^+ \\ 0, & otherwise \end{cases} \qquad \text{(VI)}.$$

Here, f_i^- and f_i^+ respectively, specify the minimum and maximum frequency to contribute to the ith shell and *f* denotes the radial spatial frequency. To minimize discretization errors, we replaced the box like function with a Gaussian sampling profile:

$$\omega_i(f) = e^{-\frac{(f-f_i)^2}{2\sigma_f^2}} \qquad \text{(VII)}$$

where σ_f controls the width of the profile and is chosen to coincide with the distance between the subsequent rings. From this point, we generalized to a cone based FSC by introducing an angular dependence in the weight function:

$$\omega_i(f,\dot{\phi}) = e^{-\frac{(f-f_i)^2}{2\sigma_f^2}} e^{-\frac{(\angle(\dot{\phi},\dot{\phi}_i))^2}{2\sigma_c^2}} \qquad \text{(VIII)}.$$

In (VIII) the first term selects the radial frequency band, whereas the second term selects a double

cone with orientation Φ_i and an angular Gaussian profile. The control parameter σ_c is set to the average distance between neighboring sample orientations. The reasons for setting the values for σ_f and σ_c as chosen are to make sure that every voxel is contributing with the same weight to the final result and to assure minimal smoothing. The sample orientations are chosen for a given number by the spiral point algorithm (*37*). Each $cFSC_{e/o}$ was performed on cubic sub-volumes varying in size between 64^3 and 128^3 voxels and using 200 orientations for uniform sampling. A fixed correlation cut-off of 0.5 was used as the resolution criterion.

Artificial data sets were created to test the $cFSC_{e/o}$ implementation for its susceptibility to artifact generation, to check the influence of noise levels and alignment quality on the measurements, and for its ability to detect missing data areas (wedge and pyramid) in Fourier space and directional signals (Supplemental Fig. S3 to S5).

We started by computing the $cFSC_{e/o}$ of single- and dual-axis tomograms of both simulated and acquired data sets. Next, $cFSC_{e/o}$ was used to compare generated dual-axis tomograms of stained insect flight muscle that were merged and reconstructed using three different stand-alone software implementations (*IMOD*, *Inspect3D*, and *Protomo*) as well as using the three *Protomo*/*IMOD* hybrid approaches.

As a control, $FSC_{e/o}$ measurements were performed using the *ELECTRA* program et-fsceo. In these measurements missing areas in Fourier space were omitted using Fourier space masks created in the *bmissing* utility of the Bsoft software suite (version 1.5.4; *38*).

For all $cFSC_{e/o}$ measurements, it was ensured that the measured resolution perpendicular to the primary tilt axis was below a critical resolution $r_{crit} = 2\Delta\theta D$ (*39*), where $\Delta\theta$ is the angular increment of the full tilt series in rad and D is the measured thickness of the sample. At higher frequencies the diverging planes in Fourier space do not overlap anymore, which causes errors in the calculation of correlation coefficients for these volume elements.

RESULTS

$cFSC_{e/o}$ of single- and dual-axis electron tomograms. To measure the resolution isotropy of electron tomograms with single- and dual-axis tilt geometry, two different datasets were reconstructed in *IMOD*. First, we reconstructed a tilt series of simulated projection images of vesicular objects (Fig. 2A, left panels). These simulated tomograms were used to evaluate noise levels and can also be used for the evaluation of different parameters such as sample thickness and tilt schemes, which is useful since these parameters are fixed and cannot be varied in experimentally acquired data. Second, for real data measurements, a dual-axis low-dose cryo-electron tomogram of vitrified antibody cross-linked lipid vesicles was recorded (Fig. 2A, right panels). Real space and Fourier space sections perpendicular to all principal axes are shown to compare the main characteristics of the datasets. Differences between single- and dual-axis tomograms were most apparent when comparing sections through the Fast Fourier Transforms (FFT) perpendicular to the electron beam. In the single-axis section, a missing data wedge is clearly visible, whereas using dual-axis geometry this missing area is reduced from a wedge to a pyramid. This causes the real space images to appear visually more isotropic in sections perpendicular to the electron beam and less elongated parallel to it.

Next, $FSC_{e/o}$ as implemented in *ELECTRA* was calculated for all four tomograms to obtain initial

comparative values for the overall resolution. The $FSC_{e/o}$ showed that the resolution of the dual-axis tomograms was slightly lower than the one of the single-axis counterparts, both for simulated (9.2 vs. 8.0 pixels) and real (9.2 vs. 8.5 pixels or 6.1 vs. 5.9 nm) data (Fig. 2B and Supplemental Fig. S2). To understand this difference in resolution between the two data collection geometries, $cFSC_{e/o}$ was implemented to provide a measure for resolution isotropy (Supplemental Fig. S3 to S5). Correlations between even/odd split data sets were calculated within smooth double-sided cones directing in 200 different directions in Fourier space, originating from the center. The frequencies for correlation coefficient equal to 0.5 of the $cFSC_{e/o}$ were projected onto the surface of a sphere and flattened into a cone resolution map for easy visualization (Fig. 2C). $cFSC_{e/o}$ was applied to sub-volumes of all four tomograms (Fig. 2D and 2E). Comparable total electron dose levels in single-

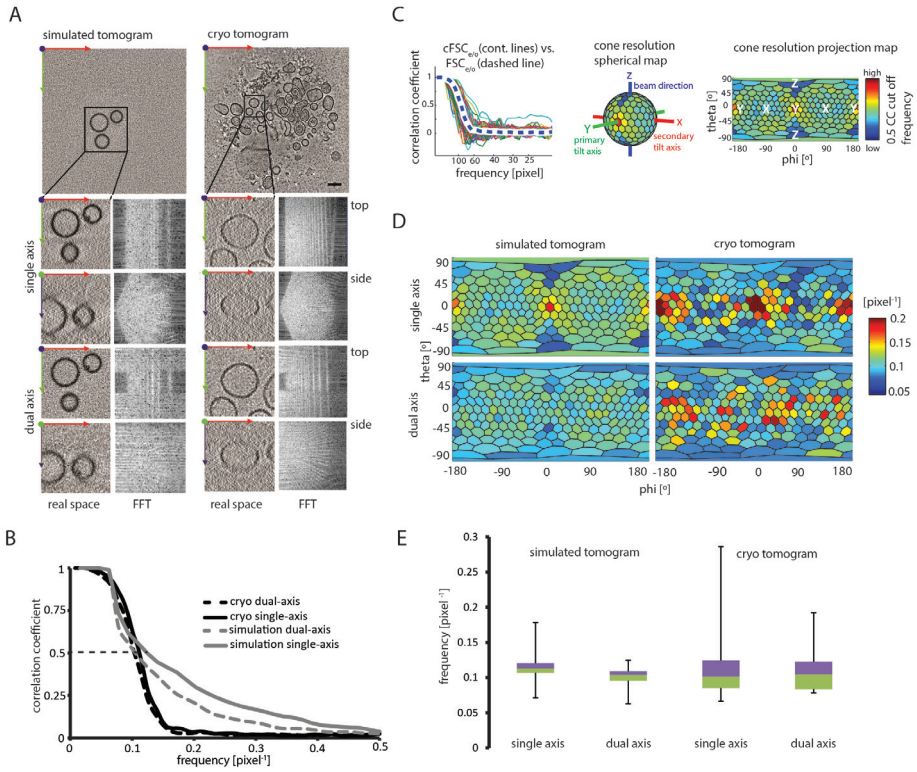

Figure 2: Isotropy estimation in single and dual-axis electron tomograms. A: Sections through single and dual-axis tomographic reconstructions of simulated hollow spheres (left) and a cryo sample of immuno-precipitated liposomes (right). Lower panels show sections through sub-volumes perpendicular and parallel to the electron beam as well as through the corresponding 3D Fourier transforms. Scale bar represents 100 nm. B: $FSC_{e/o}$ for sub-volumes shown in (A). 0.5 correlation coefficient threshold is indicated as overall resolution criterion. C: Visualization of $cFSC_{e/o}$ measurements. Per sub-tomogram 200 correlation curves are computed (left) corresponding to 200 cone positions covering a full sphere. 0.5 Correlation values are blotted onto a spherical cone resolution map (center) which is projected into a two-dimensional map (right). Color coding is from blue=low resolution to red=high resolution. D: Cone resolution maps of simulated (left) and experimentally acquired (right) single-axis (upper) and dual-axis (lower) cryo-electron tomograms. The single-axis plots show the highest resolution peaks at the tilt axes, while these are absent in the dual axis. E: Tukey box plot of cone resolution measurements indicating the degree of resolution isotropy.

and-dual axis tomograms were ascertained by selecting the angular tilt increment twice as large for the dual-axis reconstructions compared to the single-axis reconstructions. Conical resolution maps of the acquired and simulated single-axis tomograms (Fig. 2D, top panels) both showed the highest correlation in the direction of the tilt axis (Y-axis). This is expected given the high redundancy of data on the common line in Fourier space. The most prominent difference between the acquired and simulated data is that the missing wedge is distinctly visible in the $cFSC_{e/o}$ measurement of the simulated tomograms where the area in Fourier space with less resolution extends along the tilt axis and expands in direction of the electron beam (Z-axis). These distinct regions with low correlation (Fig. 2D, upper left panel) are apparent only in simulated datasets given their higher SNR (Supplemental Fig. S5) compared to the experimentally acquired data (Fig. 2D, upper right panel). For similar reasons, analysis of dual-axis tomograms showed that the reduction of the missing area from a wedge to a pyramid is visible in the simulated datasets (Fig. 2D, lower left panel; see Supplemental Fig. S4), and less clearly in the experimentally acquired datasets (Fig. 2D, lower right).

Remarkably, comparison of the $cFSC_{e/o}$ maps of single- and dual-axis tomograms showed that the high correlation peaks that were present along the tilt axis in single-axis tomograms (along Y) (Figure 2D, upper two panels), were not present on the tilt axis positions in the dual-axis tomograms (along Y and X) (Figure D, lower two panels). Instead, for the dual-axis cryo-ET (Figure 2D, lower right panel), the highest resolution peaks appeared in between the X and Y tilt axes.

To better understand how the isotropy of the resolution and the overall resolution was affected by the different data acquisition geometries, we computed Tukey box plots of the $cFSC_{e/o}$ as produced by all cones, omitting cones in the directions where no data was acquired. The results show that for both simulated and cryo dual-axis tomograms the resolution becomes more isotropic compared to their single-axis counterparts (Fig. 2E). The overall resolution of the dual-axis reconstructions of simulated data decreased compared to the single axis reconstruction, while there was no observed difference for the cryo dataset (Fig. 2E). This was in agreement with control measurements using conventional $FSC_{e/o}$ as implemented in the *ELECTRA* program et-fsceo (Fig. 2B).

Comparison of sequential and simultaneous dual-axis alignment. We hypothesized that the reduced resolution of dual-axis electron tomogram reconstructions, in particular along the tilt axes, might result from the method used for combining dual-axis tilt series into a single tomogram. Therefore, we compared different dual-axis reconstruction methods. We performed reconstructions as implemented in *IMOD* (which was used for all data shown in Fig. 2), *Protomo*, and the *Inspect3D* software packages. *IMOD* combines individually aligned and back-projected tilt series in Fourier space by warping the secondary tilt axis tomogram to fit the primary reference volume. *Inspect3D* follows a similar approach; however, we selected the real-space merging option to combine the unwarped reference tomogram with the warped tomogram. In *Protomo*, all projection images of both tilt series are aligned simultaneously and subsequently back-projected in a single reconstruction step.

For the comparison, we used a validated reference dual-axis tilt series of a stained insect flight muscle section (Fig. 3). No significant differences between the packages were observed in tomographic XY-sections nor in their respective FFTs (Fig. 3A, upper panels). XZ sections through the three dimensional FFTs show distinct intensities around the secondary tilt axis for the *Protomo*

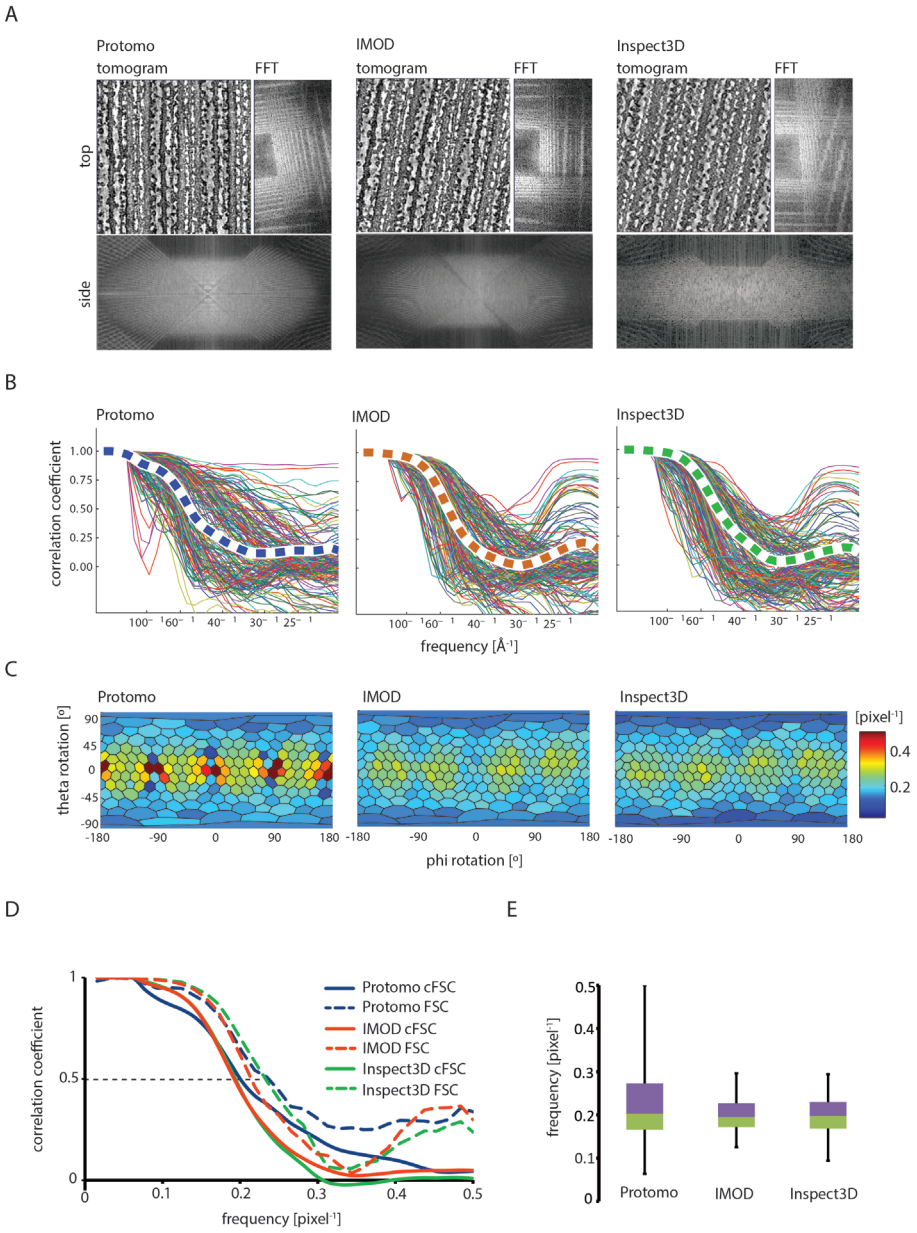

Figure 3: Influence of dual-axis reconstruction approach on the resolution isotropy. Sections through dual-axis tomograms of stained sample of insect flight muscle and the corresponding sections through their FFTs perpendicular (upper) and parallel (lower) to the electron beam direction; tomograms were reconstructed using *Protomo* (left), *IMOD* (center), or *Inspect3D* (right) software packages. B-E: $cFSC_{e/o}$ analysis of dual-axis tomograms: Individual cone correlation curves (B), cone resolution maps (C), averaged $cFSC_{e/o}$ and conventional FSC curves (D), and Tukey box plots as measures for overall resolution and isotropy (E) for each reconstruction method.

reconstruction, while these are absent in the corresponding section of *Inspect3D* and *IMOD* FFTs (Fig. 3A, lower panels).

Next, both the directional and overall resolution of the three reconstructions were estimated using $cFSC_{e/o}$ and $FSC_{e/o}$ (Fig. 3B to 3E). The $cFSC_{e/o}$ map of the *Protomo* reconstruction showed discernable high correlation peaks along the primary and secondary tilt axis (Y and X direction) and low resolution peaks immediately above and below these tilt axes (Fig. 3C, left panel).These characteristic features were absent in $cFSC_{e/o}$ maps of *IMOD* (center panel) as well as *Inspect3D* reconstructions (right panel). As a result, the overall resolution of the *Protomo* reconstruction (Fig. 3C and 3E), was significantly higher and less isotropic compared to that of *IMOD* or *Inspect3D* reconstructions (Fig. 3D and E).

To investigate whether the absence of the high-resolution peaks along the tilt axes in the dual axis *IMOD* reconstructions (Fig. 4 A, column 1) was caused by differences in tilt series alignment (separate in *IMOD* vs simultaneous in *Protomo*), we used the *Protomo* alignments for further processing in *IMOD*. $cFSC_{e/o}$ measurements showed that the simultaneous alignment of *Protomo* did not recover the high-resolution peaks in the direction of the tilt axes (Fig. 4 A, column 2). Moreover, the overall resolution decreased (Fig. 4 B), indicating that the alignments in *IMOD* might be better. We noticed that the initial transformation matrix (that is needed for the combination

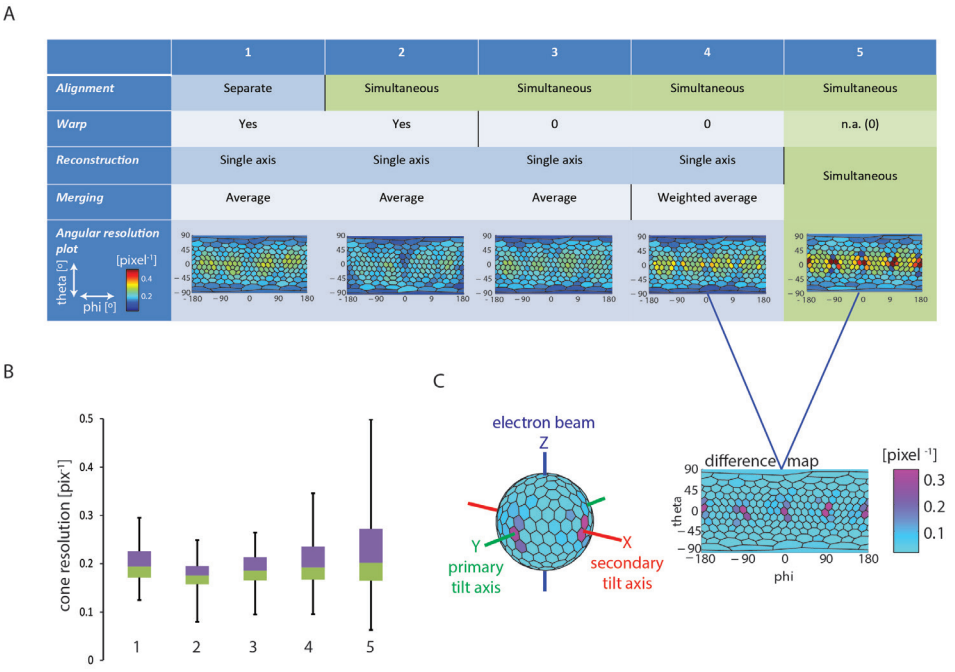

Figure 4: $cFSC_{e/o}$ analysis of dual axis tomography reconstructions using hybrid *IMOD/Protomo* approaches. A: Tabular overview of five different hybrid workflows: Full *IMOD* reconstruction (column 1), *Protomo* alignment followed by *IMOD* reconstruction as in column 1 (column 2), same workflow as in column 2 without warping (column 3), same workflow as in column 3 with additional amplitude weighting during volume averaging (column 4), full *Protomo* alignment and reconstruction (column 5). B: Tukey box plots of $cFSC_{e/o}$ measurements shown in (A). C: Spherical and planar difference map between simultaneously aligned, non-warped, and weighted averaged *IMOD* reconstruction (4) and full *Protomo* reconstruction (5) as shown in (A).

of the single axis tomograms in *IMOD*) for the two separate volumes of the *Protomo* alignment changed significantly, apart from the expected 90º rotation a significant squeezing in Z-direction was applied. Therefore, we disabled volume warping (enforcing the transformation from the *Protomo* alignment), which indeed improved the results, although the high resolution at the principle axis was not recovered (Fig. 4 A, column 3).
Since the alignment does not appear to be the cause of the resolution discrepancies, we reasoned that averaging of amplitudes (which is default in *IMOD*) of oversampled and undersampled data (along the principle tilt axis of series A with the perpendicular axis of series B and vice versa) is not optimal for getting the highest resolution. Full amplitude weighting, indeed, enabled us to improve the resolution, specifically near the axis, but not on the axis (Fig. 4 A, column 4), which is clearly shown by a difference resolution isotropy map (Fig. 4 C) with the full *Protomo* reconstruction (Fig. 4 A, column 5).

DISCUSSION

The resolution of both single- and dual-axis electron tomograms is highly anisotropic, given that the reconstructions are generated from a geometrically restricted tilt series. Our goal was to assess these geometrical effects using directional resolution measurements by comparing tomograms recorded with single-axis and dual-axis tilt schemes, with identical total electron doses. Therefore, we developed and used $cFSC_{e/o}$, a directional resolution measurement based on $FSC_{e/o}$.
As highlighted by Penczek and Frank (*30*), FSC in electron microscopy is not a direct measure of 'resolution' as it is understood in optics. In optics, the resolvability of two objects depends on the wavelength and point-spread function, whereas the FSC rather represents a 'phase consistency measure'. Also, the choice of resolution criterion, e.g., a fixed correlation threshold, remains a matter of discussion. $cFSC_{e/o}$ should therefore be seen as a qualitative tool for comparison of resolution isotropies rather than a quantitative method that yields absolute resolution values. Additionally, it is difficult to assess resolution with Fourier correlation, since measurements might rather reflect the spatial sampling of the tilt series geometry than the statistical reproducibility of the data.
Initial $cFSC_{e/o}$ measurements in single-axis tomograms indeed showed that higher resolution (higher correlation values) coincides with expected directions of higher SNR in the data. The highest resolution is measured along the tilt axis, as this is the common line of all projection planes in Fourier space. Surprisingly, this did not apply to dual-axis (*IMOD*) reconstructions which resulted in a lower resolution along the tilt axes than could be expected from spatial sampling. This loss of resolution could potentially arise during tilt series alignment, dual axis data merging or during tomographic reconstruction.
Therefore, we compared different programs that use varying dual-axis alignment, merging and reconstruction procedures. Initially, $cFSC_{e/o}$ was developed to investigate the validity of recording dual axis tilt series for cryo-ET. However, it appeared that due to the low signal-to-noise ratio, cryo-electron tomograms did not show these features unambiguously enough for further investigation. Therefore, we used stained sections data with high SNR. This showed that the specific dual-axis reconstruction schemes affect the overall resolution as well as its isotropy. The simultaneous dual-axis alignment and reconstruction approach, as currently implemented in *Protomo*, was found to

preserve high resolution along both tilt axes and resulted in a high overall resolution. Since both *IMOD* and *Inspect3D* packages, which use merging of separate tilt series either in Fourier or real space, did not preserve these high-resolution data along the tilt axes, we suspected that either the simultaneous tilt series alignment, without warping, or differences in the averaging algorithms might be beneficial for preservation of the high resolution.

To find out at which steps these differences arise during reconstruction, we devised different tomographic reconstruction schemes, combining the simultaneous tilt series alignment procedure of *Protomo* with the tomogram volume reconstruction from *IMOD*. Angular resolution plots of different dual-axis resolution schemes showed that the simultaneous tilt series alignment of *Protomo* was not responsible for the conservation of the high resolution along the tilt axis. In fact, meging the combination of dual tilt series alignment and further reconstruction in *IMOD* resulted in a worse reconstruction than using the separate tilt series alignment approach, which for unknown reasons could be improved by not warping volumes during merging or additionally use weighted averaging of amplitudes during merging. Instead, it seemed that *Protomo*'s (simultaneous) reconstruction and merging was responsible for maintaining the strong SNR along the tilt axes. This also explains that averaging of sub-tomograms reconstructed using this scheme in *Protomo* resulted in higher resolution maps compared to those reconstructed by non-simultaneous reconstruction schemes (as currently implemented in *IMOD*) (*25*). Additionally, our results suggests that sub-optimal merging (averaging instead of weighted averaging based on SNR) of the oversampled data along the tilt axis in the first series with sparsely sampled data in the direction perpendicular to the tilt axis of the second series (and vice versa) results in a suboptimal resolution along the tilt axes.

The datasets we used for investigating the different schemes and resolution measurements – the simulated, cryo, and *Protomo* test datasets – are expected to show little distortions and indeed required minimal corrections for distortions (data not shown). A simultaneous alignment approach as used by *Protomo*, which does not locally warp the individual images, produces tomograms with higher resolution if the two tilt series have fewer distortions to begin with. It should be noted that *IMOD* will be particularly beneficial for samples that suffer from distortions, as it allows for distortion corrections during tomogram merging (*23*). The $cFSC_{e/o}$ measurement that we developed for our analysis is based on an accepted and widely used approach for resolution estimation, Fourier shell correlation. While $cFSC_{e/o}$ is therefore suitable for comparisons of alignment and reconstruction methods, it is important to consider that FSC curves calculated for electron tomograms have several inherent properties (Fig. 3.4 in *40*) that can lead to uncertainty over resolution assignment using the FSC=0.5 criterion (see, e.g., Fig. 3B). In conclusion, we developed conical Fourier shell correlation of even-odd tomographic datasets, based on existing $FSC_{e/o}$ methods, which can be used to compare resolutions in different directions. We applied $cFSC_{e/o}$ to single- and dual-axis tomographic datasets and showed that the isotropy in dual-axis electron tomograms is increased, and that the overall resolution can also increase, depending on the used reconstruction approach. We anticipate that $cFSC_{e/o}$ can also be useful for comparisons of acquisition and reconstruction parameters, and different hardware implementations, including phase plate and detectors. Furthermore, the method is applicable for any tomographic recording technique.

ACKNOWLEDGEMENTS

We thank Peter van der Ley (NVI) for vesicles and antibodies, Jason Pearson and Matthijn Vos (FEI Company) for help with data collection at the FEI nanoport, Giovanni Cardone (NIH) for discussion and Charlotte Melia (LUMC) and Philipp Diebolder (WUSTL) for critically reading the manuscript. FGAF is financed through NanoNextNL and CAD through ERC grant 233229.

REFERENCES

1. X. Zhang, L. Jin, Q. Fang, W. H. Hui, and Z. H. Zhou, 3.3 Å cryo-EM structure of a nonenveloped virus reveals a priming mechanism for cell entry, *Cell* **141**, 472-482 (2010).
2. A. Amunts, A. Brown, X. c. Bai, J. L. Llacer, T. Hussain, P. Emsley, F. Long, G. Murshudov, S. H. Scheres, and V. Ramakrishnan, Structure of the yeast mitochondrial large ribosomal subunit, *Science* **343**, 1485-1489 (2014).
3. C. A. Diebolder, A. J. Koster, and R. I. Koning, Pushing the resolution limits in cryo electron tomography of biological structures, *Journal of Microscopy* **248**, 1-5 (2012).
4. M. van Heel and G. Harauz, Resolution criteria for three dimensional reconstruction, *Optik* **73**, 119-122 (1986).
5. G. Harauz and M. van Heel, Exact Filters for general geometry three dimensional reconstruction, *Proceedings of the IEEE Computer Vision and Pattern Recognition Conf* **73**, 146-156 (1986).
6. W. O. Saxton and W. Baumeister, The correlation averaging of a regularly arranged bacterial cell envelope protein, *Journal of Microscopy* **127**, 127-138 (1982).
7. M. van Heel, Detection of objects in quantum-noise-limited images, *Ultramicroscopy* **7**, 331-341 (1982).
8. J. Frank and L. Al-Ali, Signal-to-noise ratio of electron micrographs obtained by cross correlation, *Nature* **256**, 376-379 (1975).
9. A. Malhotra, P. Penczek, R. K. Agrawal, I. S. Gabashvili, R. A. Grassucci, R. Jünemann, N. Burkhardt, K. H. Nierhaus, and J. Frank, *Escherichia coli* 70 S ribosome at 15 Å resolution by cryo-electron microscopy: localization of fmet-tRNAf^{Met} and fitting of L1 protein, *Journal of molecular biology* **280**, 103-116 (1998).
10. P. B. Rosenthal and R. Henderson, Optimal determination of particle orientation, absolute hand, and contrast loss in single-particle electron cryomicroscopy, *Journal of molecular biology* **333**, 721-745 (2003).
11. B. Boettcher, S. A. Wynne, and R. A. Crowther, Determination of the fold of the core protein of hepatitis B virus by electron cryomicroscopy, *Nature* **386**, 88-91 (1997)
12. M. van Heel and M. Schatz, Fourier shell correlation threshold criteria, *Journal of structural biology* **151**, 250-262 (2005).
13. G. Cardone, K. Grünewald, and A. C. Steven, A resolution criterion for electron tomography based on cross-validation, *Journal of structural biology* **151**, 117-129 (2005).
14. P. Penczek, M. Marko, K. Buttle, and J. Frank, Double-tilt electron tomography, *Ultramicroscopy* **60**, 393-410 (1995).

15. S. Lanzavecchia, F. Cantele, P. L. Bellon, L. Zampighi, M. Kreman, E. Wright, and G. A. Zampighi, Conical tomography of freeze-fracture replicas: a method for the study of integral membrane proteins inserted in phospholipid bilayers, *Journal of structural biology* **149**, 87-98 (2005).
16. C. V. Iancu, E. R. Wright, J. Benjamin, W. F. Tivol, D. P. Dias, G. E. Murphy, R. C. Morrison, J. B. Heymann, and G. J. Jensen, A "flip-flop" rotation stage for routine dual-axis electron cryotomography, *Journal of structural biology* **151**, 288-297 (2005).
17. C. A. Diebolder, F. J. Beurskens, R. N. de Jong, R. I. Koning, K. Strumane, M. A. Lindorfer, M. Voorhorst, D. Ugurlar, S. Rosati, A. J. Heck, J. G. van de Winkel, I. A. Wilson, A. J. Koster, R. P. Taylor, E. Ollmann Saphire, D. R. Burton, J. Schuurman, P. Gros, and P. W. Parren, Complement Is Activated by IgG Hexamers Assembled at the Cell Surface, *Science* **343**, 1260-1263 (2014).
18. N. V. Dudkina, G. T. Oostergetel, D. Lewejohann, H. P. Braun, and E. J. Boekema, Row-like organization of ATP synthase in intact mitochondria determined by cryo-electron tomography, *Biochimica et Biophysica Acta (BBA)-Bioenergetics* **1797**, 272-277 (2010).
19. S. Nickell, R. Hegerl, W. Baumeister, and R. Rachel, Pyrodictium cannulae enter the periplasmic space but do not enter the cytoplasm, as revealed by cryo-electron tomography, *Journal of structural biology* **141**, 34-42 (2003).
20. A. G. Myasnikov, Z. A. Afonina, and B. P. Klaholz, Single particle and molecular assembly analysis of polyribosomes by single-and double-tilt cryo electron tomography, *Ultramicroscopy* **126**, 33-39 (2013).
21. D. Chen, H. Friedrich, and G. d. With, On Resolution in Electron Tomography of Beam Sensitive Materials, *The Journal of Physical Chemistry C* **118**, 1248-1257 (2014).
22. A. Guesdon, S. Blestel, C. Kervrann, and D. Crétien, Single versus dual-axis cryo-electron tomography of microtubules assembled in vitro: Limits and perspectives, *Journal of structural biology* **181**, 169-178 (2013).
23. D. N. Mastronarde, Dual-axis tomography: an approach with alignment methods that preserve resolution, *Journal of structural biology* **120**, 343-352 (1997).
24. R. H. M. Schoenmakers, R. A. Perquin, T. F. Fliervoet, W. Voorhout, and H. Schirmacher, New software for high resolution, high throughput electron tomography, *Microscopy and Analysis* **19**, 5-6 (2005).
25. H. Winkler and K. A. Taylor, Marker-free dual-axis tilt series alignment, *Journal of structural biology* **182**, 117-124 (2013).
26. F. Cantele, E. Paccagnini, G. Pigino, P. Lupetti, and S. Lanzavecchia, Simultaneous alignment of dual-axis tilt series, *Journal of structural biology* **169**, 192-199 (2010).
27. P. A. Penczek, Three-dimensional spectral signal-to-noise ratio for a class of reconstruction algorithms, *Journal of structural biology* **138**, 34-46 (2002).
28. M. Unser, C. S. Sorzano, P. Thevenaz, S. Jonic, C. El-Bez, S. De Carlo, J. F. Conway, and B. L. Trus, Spectral signal-to-noise ratio and resolution assessment of 3D reconstructions, *Journal of structural biology* **149**, 243-255 (2005).
29. H. Heidari Mezerji, W. Van den Broek, and S. Bals, A practical method to determine the effective resolution in incoherent experimental electron tomography, *Ultramicroscopy* **111**, 330-336 (2011).

30. P.A. Penczek, and J.Frank, *Resolution in electron tomography. Electron Tomography* 307-330 (2006).
31. I. Claassen, J. Meylis, P. van der Ley, C. Peeters, H. Brons, J. Robert, D. Borsboom, A. van der Ark, I. van Straaten, and P. Roholl, Production, characterization and control of a Neisseria meningitidis hexavalent class 1 outer membrane protein containing vesicle vaccine, *Vaccine* **14**, 1001-1008 (1996).
32. C. L. Hendriks, L. J. Van Vliet, B. Rieger, G. M. P. van Kempen, and M. van Ginkel, DIPimage: a scientific image processing toolbox for MATLAB, Quantitative Imaging Group, Faculty of Applied Sciences, Delft University of Technology, Delft, The Netherlands (1999).
33. S. Wu, J. Liu, M. C. Reedy, H. Winkler, M. K. Reedy, and K. A. Taylor, Methods for identifying and averaging variable molecular conformations in tomograms of actively contracting insect flight muscle, *Journal of structural biology* **168**, 485-502 (2009).
34. J.R. Kremer, D.N.Mastronarde, and J.R.McIntosh, Computer visualization of three-dimensional image data using *IMOD*. *Journal of structural biology* **116**, 71-76 (1996).
35. J. J. Fernandez, S. Li, and R. A. Crowther, CTF determination and correction in electron cryotomography, *Ultramicroscopy* **106**, 587-596 (2006).
36. A. S. Frangakis and R. Hegerl, Noise reduction in electron tomographic reconstructions using nonlinear anisotropic diffusion, *Journal of structural biology* **135**, 239-250 (2001).
37. E. B. Saff and A. B. Kuijlaars, Distributing many points on a sphere, *The Mathematical Intelligencer* **19**, 5-11 (1997).
38. B. Heymann and D. M. Belnap, Bsoft: image processing and molecular modeling for electron microscopy, *Journal of structural biology* **157**, 3-18 (2007).
39. R. N. Bracewell and A. C. Riddle, Inversion of fan-beam scans in radio astronomy, *The Astrophysical Journal* **150**, 427 (1967).
40. P. A. Penczek, Resolution measures in molecular electron microscopy, *Methods in enzymology* **482**, 73-100 (2010)

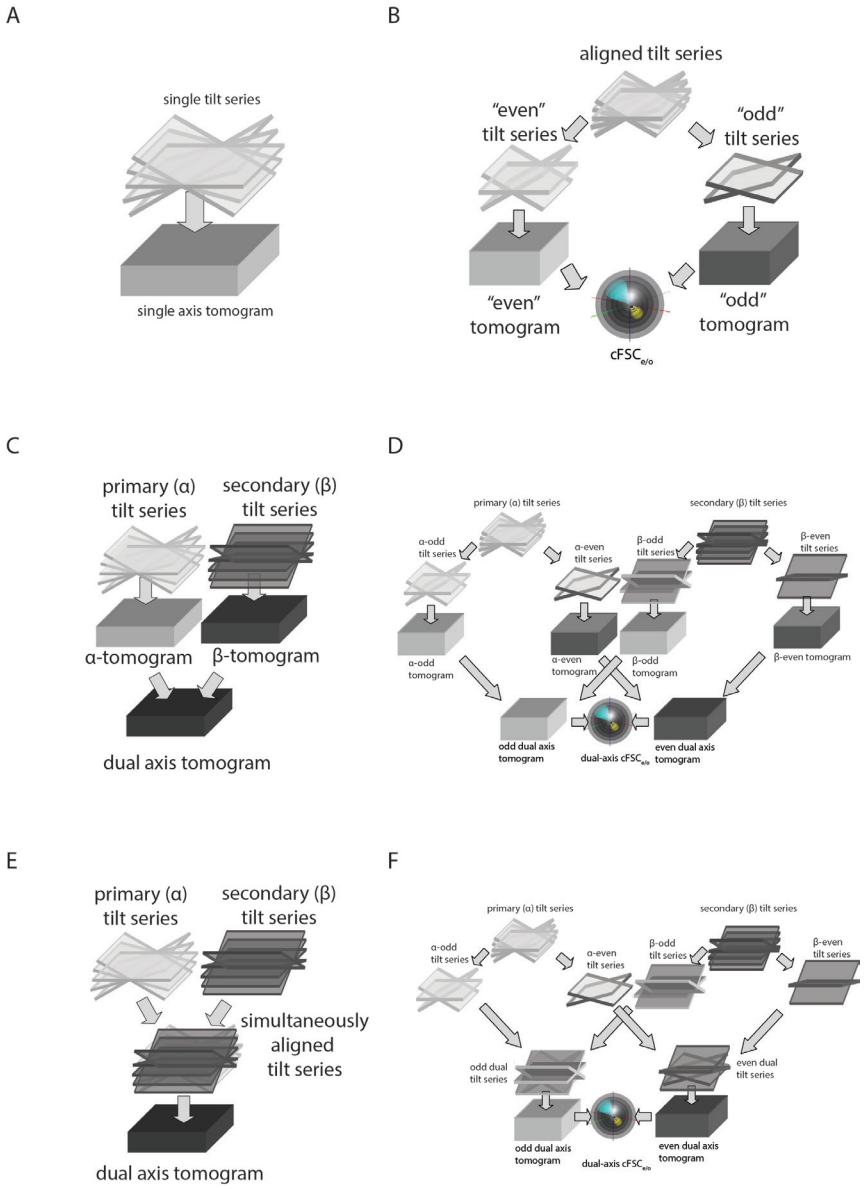

Supplemental Figure S1: cFSC$_{e/o}$ workflows for tomograms with different reconstruction schemes. A-B: Single-axis reconstruction workflow (A) and approach used to create even/odd split tomograms for conical Fourier shell correlation measurements (B). C-F: Reconstruction procedures and the workflows for even/odd data splitting for the two different dual-axis reconstruction approaches discussed. In *IMOD* and *Inspect3D* independently aligned and reconstructed single tilt tomograms are merged (C). Accordingly, even and odd dual-axis tomograms for cFSC$_{e/o}$ calculations are created by tilt axis merging after back projection (D). E. Dual-axis reconstruction in *Protomo* is based on simultaneous alignment of all projection images prior to back-projection into one volume. F. Even and odd dual-axis tomograms for cFSC$_{e/o}$ calculations are therefore created by merging projection images from perpendicular axes before image alignment.

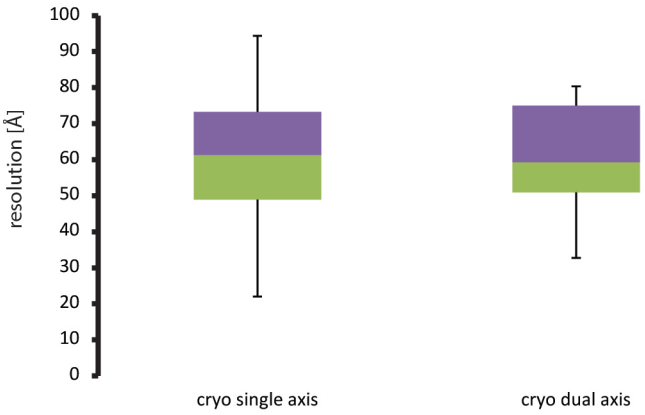

Supplemental Figure S2: Tukey box plot of cFSC$_{e/o}$ measurements. Resolution analysis of single and dual axis cryo electron tomograms from Figure 2A showing median values of 6.1 nm and 5.9 nm.

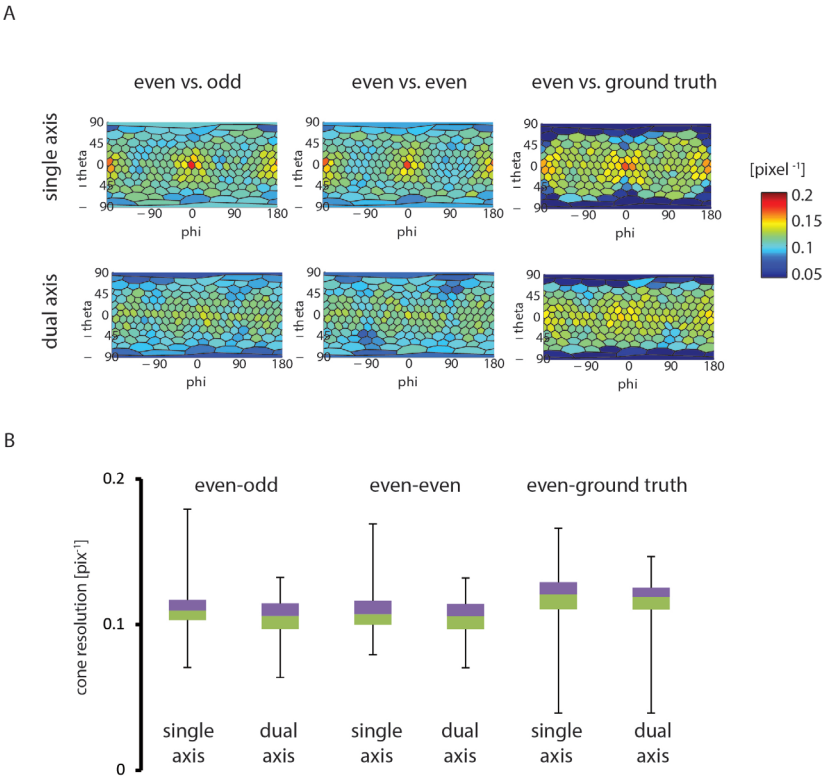

Supplemental Figure S6: cFSC$_{e/o}$ measurements on simulated data. Cone resolution maps of simulated single and dual axis data in *IMOD* comparing tomograms from even and odd split data (left column), tomograms from even split data with independent noise and identical SNR (center column), and tomogram from even data with original data and matched SNR (right column) (A). Tukey box plot of measurements in (B).

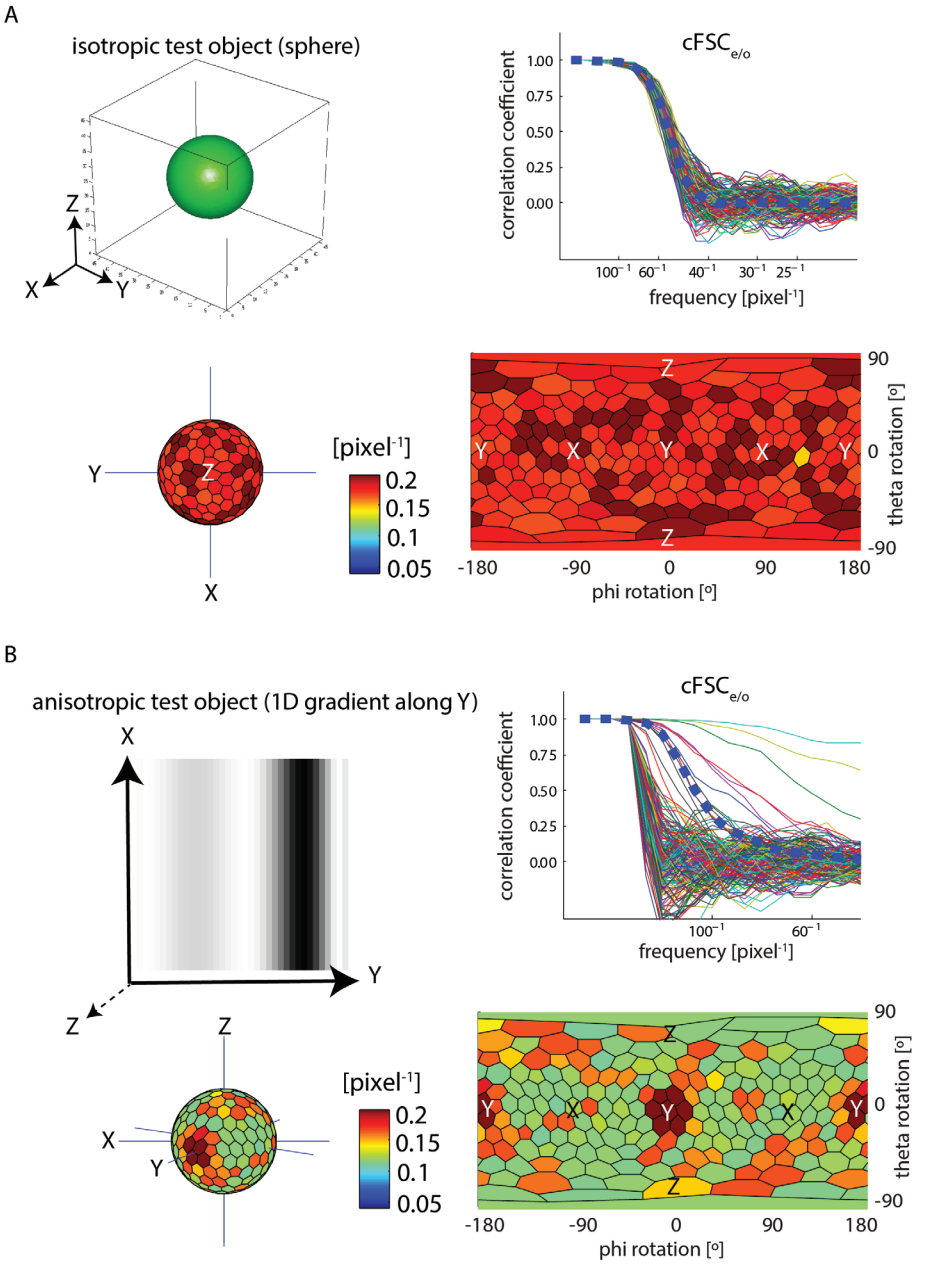

Supplemental Figure S3: cFSC$_{e/o}$ and detection of resolution anisotropy. A: we used a hollow sphere as an isotropic object (upper left panel) to evaluate the implementation. The individual cFSC$_{e/o}$ curves (upper right panel); spherical (lower left panel) and planar (lower right panel) cone correlation maps show an isotropic pattern of resolution. B: One dimensional gradient as a highly anisotropic test pattern (upper left panel) to evaluate the implementation. The individual cFSC$_{e/o}$ curves (upper right panel); cone correlation maps indicate highest correlation in the direction of the gradient (lower panels). The conical Fourier shell correlation was measured between volumes containing similar objects but independent Gaussian noise (σ=1).

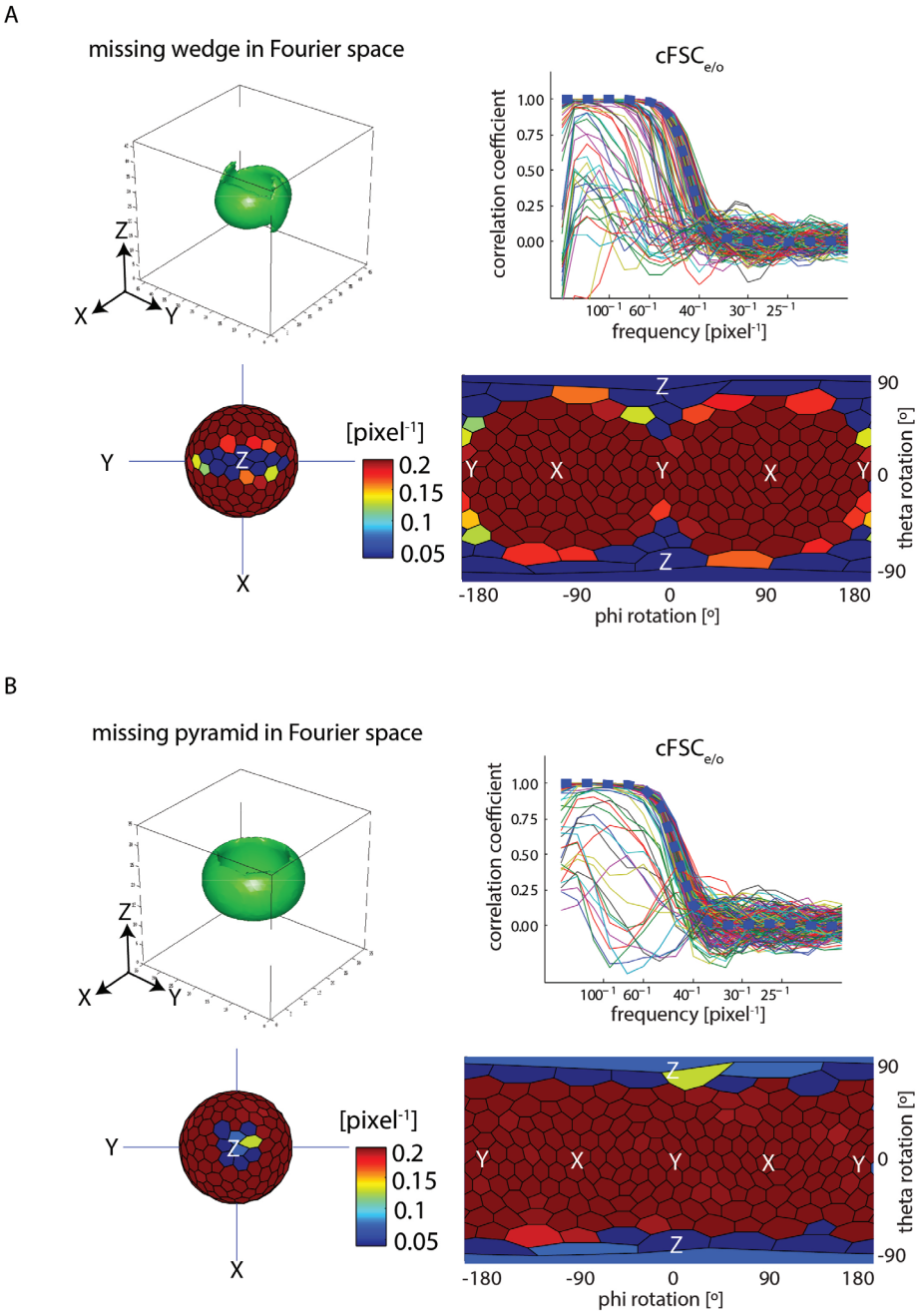

Supplemental Figure S4: cFSC$_{e/o}$ to detect missing areas in Fourier space. A: An isotropic object (shell used in supplemental Fig. S2A) with a masked missing wedge in Fourier space (upper left panel). The individual cFSC$_{e/o}$ curves (upper right panel), and spherical (lower left panel) and planar cone resolution maps (lower panels). B: An isotropic object with a missing pyramid in Fourier space. Conical Fourier shell correlation was measured between volumes containing similar objects but independent Gaussian noise (σ=1).

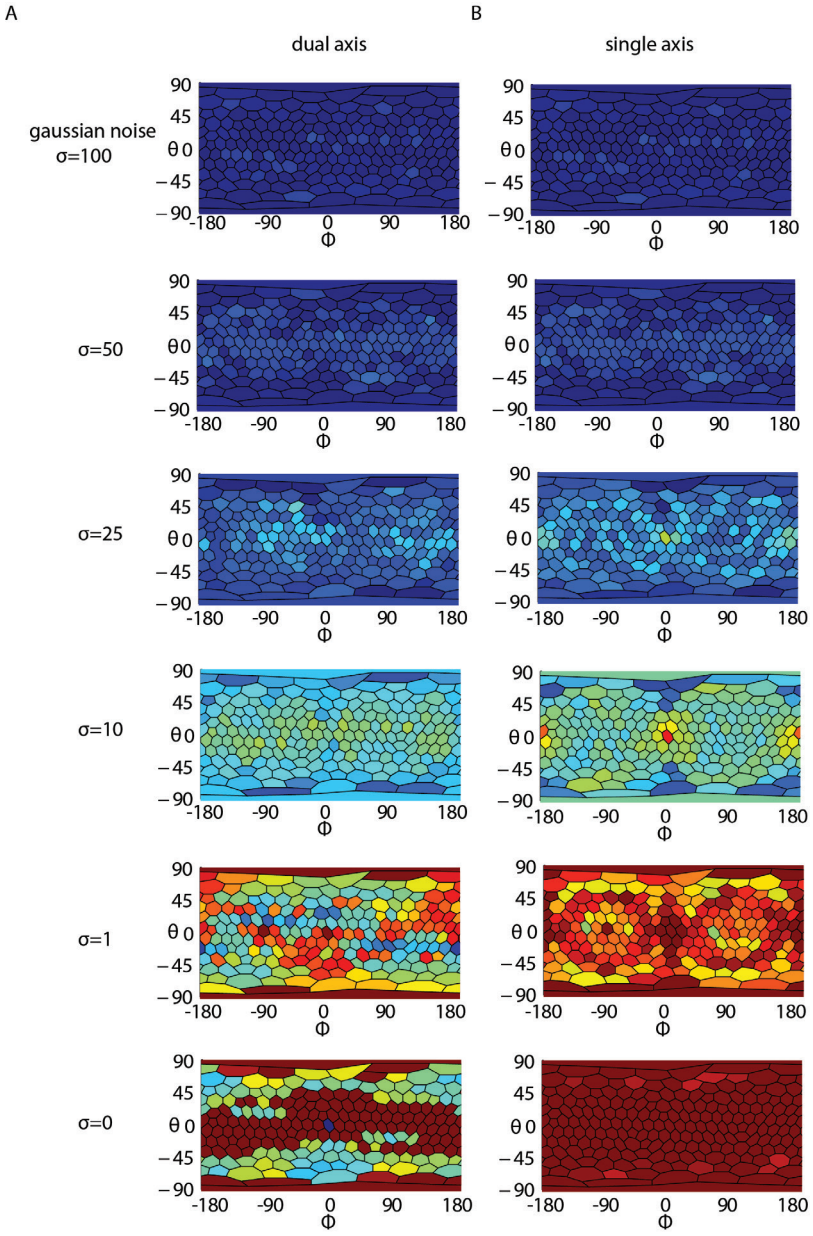

Supplemental Figure S5: cFSC$_{e/o}$ to measure resolution isotropy depending on noise levels in tomographic reconstructions. Cone resolution maps of dual-axis (A) and single-axis (B) electron tomograms with varying noise levels. Gaussian noise was added to projection images of an isotropic object (a shell as used in supplemental Fig. S3 and S4). Noise levels range from high noise (σ=100, upper panels) to no noise (σ=0, lower panels). At noise levels similar to cryo-electron tomograms (σ~10), cone resolution maps show characteristic features such as missing areas (low resolution) and common lines (high resolution). All tomograms were reconstructed in *IMOD*.

CHAPTER 6

SUMMARIZING DISCUSSION

Christoph A. Diebolder[1,2]

[1]Crystal and Structural Chemistry, Bijvoet Center for Biomolecular Research, Department of Chemistry, Faculty of Science, Utrecht University, 3584 CH Utrecht, The Netherlands

[2]Department of Molecular Cell Biology, Section Electron Microscopy, Leiden University Medical Center, 2300 RC Leiden, The Netherlands

THE NEW ERA OF CRYO-EM IN STRUCTURAL BIOLOGY

This thesis describes the structural research on two immunologic initiation complexes by cryo-electron microscopy. In addition, methodological work is conduceted related to the achievable resolution of cryo-EM reconstructions: Which factors are limiting and how can the resolution in tomograms be measured? During the last five years, since the start of the research described in this thesis, significant methodological breakthroughs have been accomplished in the field of cryo-EM which have had large impact on the possibilities of cryo-EM studies on protein complexes, including the complexes described in this thesis and related immunologic complexes.

As noted in **chapter 4**, which provides an overview on the resolution limiting factors in cryo-electron tomography, cryo-EM has recently gained significant importance in structural biology. Several technical breakthroughs made these rapid developments possible. Concerning hardware, the availability of more and more sensitive high-resolution direct electron detectors had a dramatic impact, providing images of electron dose sensitive structures with a precedent quality due to their dramatically increased modulation transfer function (MTF) and detection quantum efficiency (DQE). Ongoing developments of these type of detectors aim for even further improvement of their technical specifications (*1*). Other promising features of these sensitive detectors are the possibilities to collect with high-speed sequences of image in "movie mode", which allows post-data acquisition correction for beam-induced sample motion, or in "electron counting mode" for super-resolution data collection at twice the Nyquist frequency by determining the location of electron impact on the detector with an accuracy smaller than one pixel (*2*). Because of these technological developments, cryo-EM single particle reconstructions show, in some cases, a resolution close to the models provided by X-ray crystallography (*3*). As of April 2015, the highest resolution single particle reconstructions deposited at the Electron Microscopy Data Bank (EMDB) are the 2.6 Å icosahedral reconstruction of rotavirus VP6l , a symmetric (D7 symmetry) proteasome structure at 2.8 Å resolution (*4*) and 2.9 Å unsymmetrical reconstruction (C1 symmetry) of the *E.coli* ribosome.

Another significant hardware development was the commercial availability of a stable phase plate less than six months ago. This device, positioned in the back focal plane of the objective lens in the transmission electron microscope column, dramatically increases the (low spatial frequency) image contrast by shifting the phase of the scattered electron beam by $\pi/2$. The phase shift allows imaging of frozen hydrated samples with high contrast without the need for defocusing. The first imaging experiments in the field, in fact, show a spectacular improvement in image contrast. For a long time the Zernike type of phase plate seemed to be the most promising design and, indeed, impressive publications of these (experimental) phase plates that consisted of holy films positioned at the back focal plane showed promising results (*5*). However, it appeared that these films show in practical usage stability issues related to material fatigue of the holey carbon film. This instability requires regular replacement and realignment and therefore hinders high-throughput data acquisition. A promising alternative to the Zernike phase plate type, as well as to other proposed types of phase plates that were described during the last decade, was the design recently described and referred to as the Volta phase plate (*6*). In the Volta phase plate, several technological issues are circumvented by the creation of "virtual" holes in heated continuous carbon films. The phase shift is induced "on the fly" and is explained –despite not yet fully understood yet – by beam induced

charge causing a local potential on the film that has a reverting phase shift effect of the un-scattered electron beam. Cryo-ET will benefit from the phase plate in particular, and initial studies are exploring the potential of this technology (*7,8*).

Apart from hardware developments the continuously and ongoing improvement of workflows in cryo-ET during data collection and processing steps enabled a significant improvement in the resolution that can be practically attained with sub-tomogram averaging (*9*). Improved resolution was shown to be possible by optimization of three resolution limiting parameters: [I] total dose limitation to 40 E/Å2 to reduce the radiation damage, [II] defocus estimation at 100 nm accuracy to allow precise CTF correction (*10*), and [III] acquisition of very large data sets, comprising >30.000 asymmetric units. Sub-tomogram averages of immature HIV capsids at 8.8 Å resolution could be achieved (*11*). And even the dream of 'structural biology *in situ*' seems to be in reach (*12*).

Concerning software, two recent developments have had a beneficial effect on the resolution in cryo-EM by tackling two major resolution-limiting issues in the processing of cryo-EM data: Sample heterogeneity and beam induced motion. The first issue is related to the question on how to classify images of a heterogeneous set of particles. Structure determination by Cryo-EM/ET is generally an ill-posed mathematical problem because data sets are noisy and incomplete. As a consequence, resulting models are prone to model bias and over-fitting at high frequencies (the model rather describes noise than signal). A solution to this problem is given by regularization by prior external knowledge. In structural biology, prior knowledge can be incorporated by invoking information related to particle orientations, such as the perpendicularity of the "C1-Eiffel-towers" to the liposome membrane described in **chapter 2**, or symmetry, such as the assumed helical symmetry in the inflammasome reconstruction in **chapter 3**. However, in many cases, a priori knowledge is limited, and wrong assumptions lead to biased and incorrect results. A more generally valid piece of prior knowledge would be the smoothness of the biological sample and, consequently, low pass (or other type of) spatial filtering is part of many images processing pipelines. However, the choice of filter settings is not straightforward and over-fitting is a common problem in the electron microscopy field (*13*).

A recent breakthrough regarding this classification issue was achieved by introducing maximum likelihood classification approaches that have increasingly replaced supervised classification (*14,15*). Maximum likelihood classification does not require a priori information and results in more robust and reliable reconstructions. Particularly small datasets still require regularization by additional a priori information which can be incorporated in terms of Bayesian probabilities (*16*). This combined "regularized likelihood" optimization has been implemented in several EM image processing packages (*17*) which has started its triumphant success in structural biology.

A second important issue tackled by advanced post-acquisition data processing is beam-induced sample movement (*18*). Conventional charged coupled device (CCD) detectors are less sensitive for the impinging electrons and require relatively long exposure times, leading to more blurred images as compared to the latest types of direct electron detectors. These detectors allow for high-speed movie-like data collection. Dedicated algorithms that can align the frames within such, combined with selecting specific sequences of frames, has allowed to achieve close-to-atomic-resolution of ribosome reconstruction using no more than 35.000 particles (*19*). Currently, more advanced algorithms are explored for alignment and the combination of movie sequences of more challenging smaller particles (*20*).

Another relevant issue in the context of recent resolution improvements in cryo-EM is the proper validation of cryo-EM maps and their resolution. Several recent examples illustrate how easily the structural biologist can get trapped in the pitfalls hidden in the noise of their reconstructed data sets. Without doubt, the largest danger being noise-fitting against user-provided templates, often referred to as the Einstein-in-noise phenomenon (*13*). Several standards have been established to prevent over interpretation of cryo-EM reconstructions, e.g. gold-standard FSC measurements and the recording tilt-pair images (*21*). Other advanced resolution estimation methods aim to get grip on the issue of resolution anisotropy. A local resolution criterion, rather a directional as described on **chapter 5**, has been proposed for single particle reconstructions (*22*). Here, the FSC is calculated in sub-volumes of the reconstructed map. Recently, an alternative local resolution measure has been introduced that attempts to circumvent the issues related to FSC-based methods (*23*). Both methods still need to find their way into the electron tomography field and might, together with conical FSC, prove to be useful validation tools in structural biology.

However, in the light of the increasingly improving resolution obtained in single particle reconstruction and sub-tomogram averaging, one has to realize that a number indicating high resolution is not a goal in itself. On one hand, FSC-based methods are rather an internal consistency measure and an unambiguous resolution estimation can only be performed if the attained single particle EM map has sufficient, <4Å, resolution to allow for a cross validation using atomic models.

On the other hand, significantly lower resolution maps as provided by cryo-ET do not necessarily lack relevant information, especially when the drawn conclusions from those maps are supported by additional structural and functional data. The sub-tomogram average presented in **chapter 2** is a good example, not surpassing several nm resolution. Nevertheless and without doubt, the averages presented in chapters two and three would have benefited significantly from the recent technical developments described above. Most likely, exciting new structural insights based on higher resolution maps obtained by cryo-ET for these and many other macromolecular machineries can be expected in the near future.

Finally, it should be stressed that cryo-EM, compared to other methods such as X-ray crystallography, is still a relatively young technique in structural biology. In addition to the issues of attaining and validating (high-resolution) cryo-EM maps, further fundamental issues concerning basic conventions and accessibility of data still need to be solved. In this light, progress has been made regarding standardization of file formats (*24*) and establishment of frameworks to deal with large amounts of data originating from different modalities (*25*), which became necessary after a period with increasing Babylonian confusion. A central element in these latest developments is the availability and accessibility of public data archives. While it became common practice during the last five years to deposit final 3D reconstructions together with the accompanying fitted atomic models to established data banks, e.g. EMDB and PDB, this is not yet the case for the underlying raw data sets based on which the maps are generated. Nevertheless, very recently, a data bank for raw electron micrographs was introduced, the Electron Microscopy Pilot Image Archive (EMPIAR) (*25*). Although only a few datasets have been deposited so far, amongst them the raw tilt series of C1-IgG hexamers shown in **chapter 2** (EMPIAR-10009), the need for raw data deposition is becoming increasingly clear for several reasons: To avoid data loss, to allow for rigorous peer review in order to check the validity of scientific claims, as test data sets, and to allow improvement of reconstructions and scientific models by future reconstruction methods.

CRYO-ET BASED INSIGHTS INTO CLASSICAL COMPLEMENT ACTIVATION AND INFLAMMASOME ASSEMBLY

Chapter 2 provides a general model for classical complement activation by IgG antibodies, which is based on Fc mediated hexamerization on haptenated surfaces. This finding inspired a novel technology platform, the HexaBody™, aiming to optimize CDC of therapeutic antibodies that require minimized FC engineering which does not affect affinity or specificity of the parent antibody (*26*). Potential applications of CDC-enhanced antibodies include treatment of cancers. First preclinical studies on several blood cancer targeting antibodies show the potential of this technology (*27*). Enhanced CDC induced by increased Fc hexamerization was confirmed in preclinical studies for the relevant blood cancer targets CD20 and CD38 (*28*). Other studies also reveal impact of induced hexamerization on therapeutic EGFR-antibodies which naturally lack CDC capabilities (*29*). Noteworthy, IgG hexamerization here not only induces CDC by but also enhances ADCC on lung and colon cancer cells by formation of C5a (*30*). Hexabodies might also be useful for the treatment of infectious diseases. Interestingly, monoclonal antibodies are thus far not widely used in therapy of infections (*31*). One reason could be that polyclonal antisera are often more efficient in complement activation than individual monoclonal antibodies, possibly because of simplified hexamer formation particularly at low antigen concentration. On the other hand, the use of polyclonal antisera is not desirable due to safety and quality concerns. It is conceivable that efficient antibody treatment in the future will consist of a mix of several monoclonal antibodies comprising a variety specificities, affinities and sub-classes. Another important finding in Chapter 2, i.e. that monovalent binding is sufficient or even beneficial for CDC, states that a combination with bi-specific antibodies and/or antibody-drug conjugates seems promising for both the treatment of cancer and infections (*32*). Other implications were found for the field of transplantation where it is advantageous to inhibit CDC. It has been suggested that FC binding peptides like the one used in the study might be used to reduce transplant rejection (*33*). Further, the IgG hexamerization model explains the high CDC capability of hexameric FC-fusion proteins which were designed for intravenous immunoglobulin therapy (*34*).
At first glance, the assembled IgG hexamer strongly resembles the structure of IgM, an antibody sub-class that occurs in humans as native pentamers or hexamers (*35*). Likewise, both (and in particular the hexamer) are very strong complement activators because C1q binding is facilitated by increased avidity without the requirement to assemble six monomers (*36*). But how is spontaneous complement activation by IgM prevented in absence of antigens, which in case of IgG drive the CDC inducing antibody clustering? It is believed that IgM in solution occupies a conformation in which C1q binding is sterically hindered and that antigen binding induces major conformational changes that make the binding sites accessible (*37*). However, further structural studies, possibly including cryo-EM, will be needed to verify this "starfish-to-staple" conversion model (*38*).

Cryo-ET was used in **chapter 3** to study the quaternary structure of the polymerized NAIP5/NLRC4 inflammasome, which was found to arrange into a helical assemble. Fitting of the recently published crystal structure of inactive NLRC4 resulted in a model for activation of this NLR. How do these structural insights of NAIP5/NLRC4 complexes help to understand the mechanisms of inflammasome formation? Recent research activity sheds light on to the signaling mechanisms of this

heterogeneous group of cytosolic pattern recognition receptors (*39*). At least for the sub-group of ASC dependent inflammasomes, a hierarchical structural architecture has been established (*40*) which is based on ligand recognition, release of auto-inhibition, and nucleated prion-like polymerization (*41*). Indeed, such multimerization mechanism has been reported for several inflammasome components, e.g. PYD induced ASC polymerization and CARD induced caspase-polymerization (*42*). The data presented in **chapter 3** now provides evidence that this is also the case for NLRC4 during the assembly in the ASC independent NAIP5/NLRC4 inflammasome. It is, in fact, tempting to extend the recently proposed "unified mechanism of ASC dependent inflammasome formation" (*43*) to their ASC independent members. Undoubtedly, the results presented leave urgent open questions, the most burning one probably being: How does the current model for NLR signaling explain the huge and much more complex structures seen by *in vivo* super-resolution fluorescence microscopy (*44*)? Answering this question requires a transition from *in vitro* structural analysis of isolated compounds to *in situ* imaging of whole assembled inflammasomes. Future experiments aiming to unveil this secret might include (integrated) cryo-(super-resolution) correlative light and electron microscopy (*45*), likely in combination with advanced sample preparation techniques such as focused ion beam lamella milling that allows for high-resolution cellular tomography (*46*).

REFERENCES

1. G. McMullan, A. R. Faruqi, R. Henderson, N. Guerrini, R. Turchetta, A. Jacobs, and G. Van Hoften, Experimental observation of the improvement in MTF from backthinning a CMOS direct electron detector, *Ultramicroscopy* **109**, 1144-1147 (2009).
2. G. McMullan, A. R. Faruqi, D. Clare, and R. Henderson, Comparison of optimal performance at 300keV of three direct electron detectors for use in low dose electron microscopy, *Ultramicroscopy* **147**, 156-163 (2014).
3. X. c. Bai, G. McMullan, and S. H. Scheres, How cryo-EM is revolutionizing structural biology, *Trends in biochemical sciences* **40**, 49-57 (2015).
4. M. G. Campbell, D. Veesler, A. Cheng, C. S. Potter, and B. Carragher, 2.8 Å resolution reconstruction of the Thermoplasma acidophilum 20S proteasome using cryo-electron microscopy, *eLife* **4**, e06380 (2015).
5. W. Dai, C. Fu, D. Raytcheva, J. Flanagan, H. A. Khant, X. Liu, R. H. Rochat, C. Haase-Pettingell, J. Piret, and S. J. Ludtke, Visualizing virus assembly intermediates inside marine cyanobacteria, *Nature* **502**, 707-710 (2013).
6. R. Danev, B. Buijsse, M. Khoshouei, J. M. Plitzko, and W. Baumeister, Volta potential phase plate for in-focus phase contrast transmission electron microscopy, *Proceedings of the National Academy of Sciences* **111**, 15635-15640 (2014).
7. S. Asano, Y. Fukuda, F. Beck, A. Aufderheide, F. Förster, R. Danev, and W. Baumeister, A molecular census of 26S proteasomes in intact neurons, *Science* **347**, 439-442 (2015).
8. Y. Fukuda, U. Laugks, V. Luciç, W. Baumeister, and R. Danev, Electron cryotomography of vitrified cells with a Volta phase plate, *Journal of structural biology* **190**, 143-154 (2015).

9. F. K. Schur, W. J. Hagen, A. de Marco, and J. A. Briggs, Determination of protein structure at 8.5 Å resolution using cryo-electron tomography and sub-tomogram averaging, *Journal of structural biology* **184**, 394-400 (2013)
10. L. M. Voortman, M. Vuloviç, M. Maletta, A. Voigt, E. M. Franken, A. Simonetti, P. J. Peters, L. J. van Vliet, and B. Rieger, Quantifying resolution limiting factors in subtomogram averaged cryo-electron tomography using simulations, *Journal of structural biology* **187**, 103-111 (2014).
11. F. K. Schur, W. J. Hagen, M. Rumlovc, T. Ruml, B. Müller, H. G. Kräusslich, and J. A. Briggs, Structure of the immature HIV-1 capsid in intact virus particles at 8.8 Å resolution, *Nature* **517**, 505-508 (2015).
12. A. Dubrovsky, S. Sorrentino, J. Harapin, K. T. Sapra, and O. Medalia, Developments in cryo-electron tomography for in situ structural analysis, *Archives of Biochemistry and Biophysics* (2015); doi:10.1016/j.abb.2015.04.006.
13. R. Henderson, Avoiding the pitfalls of single particle cryo-electron microscopy: Einstein from noise, *Proceedings of the National Academy of Sciences* **110**, 18037-18041 (2013).
14. S. H. Scheres, H. Gao, M. Valle, G. T. Herman, P. P. Eggermont, J. Frank, and J. M. Carazo, Disentangling conformational states of macromolecules in 3D-EM through likelihood optimization, *Nature Methods* **4**, 27-29 (2007).
15. F. J. Sigworth, A maximum-likelihood approach to single-particle image refinement, *Journal of structural biology* **122**, 328-339 (1998).
16. S. H. Scheres, A Bayesian view on cryo-EM structure determination, *Journal of molecular biology* **415**, 406-418 (2012).
17. S. H. Scheres, RELION: implementation of a Bayesian approach to cryo-EM structure determination, *Journal of structural biology* **180**, 519-530 (2012).
18. A. F. Brilot, J. Z. Chen, A. Cheng, J. Pan, S. C. Harrison, C. S. Potter, B. Carragher, R. Henderson, and N. Grigorieff, Beam-induced motion of vitrified specimen on holey carbon film, *Journal of structural biology* **177**, 630-637 (2012).
19. X. c. Bai, I. S. Fernandez, G. McMullan, and S. H. Scheres, Ribosome structures to near-atomic resolution from thirty thousand cryo-EM particles, *eLife* **2**, e00461 (2013).
20. S. H. Scheres, Beam-induced motion correction for sub-megadalton cryo-EM particles, *eLife* **3**, e03665 (2014).
21. R. Henderson, A. Sali, M. L. Baker, B. Carragher, B. Devkota, K. H. Downing, E. H. Egelman, Z. Feng, J. Frank, and N. Grigorieff, Outcome of the first electron microscopy validation task force meeting, *Structure* **20**, 205-214 (2012).
22. J. B. Heymann and D. M. Belnap, Bsoft: image processing and molecular modeling for electron microscopy, *Journal of structural biology* **157**, 3-18 (2007).
23. A. Kucukelbir, F. J. Sigworth, and H. D. Tagare, Quantifying the local resolution of cryo-EM density maps, *Nature Methods* **11**, 63-65 (2014).
24. A. Cheng, R. Henderson, D. Mastronarde, S. J. Ludtke, R. H. Schoenmakers, J. Short, R. Marabini, S. Dallakyan, D. Agard, and M. Winn, MRC2014: Extensions to the MRC format header for electron cryo-microscopy and tomography, *Journal of structural biology* (2015); doi:10.1016/j.jsb.2015.04.002.
25. A. Patwardhan, A. Ashton, R. Brandt, S. Butcher, R. Carzaniga, W. Chiu, L. Collinson, P.

Doux, E. Duke, and M. H. Ellisman, A 3D cellular context for the macromolecular world, *Nature structural & molecular biology* **21**, 841-845 (2014).

26. J. P. Melis, K. Strumane, S. R. Ruuls, F. J. Beurskens, J. Schuurman, and P. W. Parren, Complement in therapy and disease: Regulating the complement system with antibody-based therapeutics, *Molecular immunology* (2015); doi:10.1016/j.molimm.2015.01.028.
27. F. J. Beurskens, C. A. Diebolder, R. de Jong, M. Voorhorst, S. Verploegen, K. Strumane, M. A. Lindorfer, R. P. Taylor, R. I. Koning, and E. O. Saphire, Enhanced IgG hexamerization mediates efficient C1q docking and more rapid and substantial complement-dependent cytotoxicity; preclinical proof of concept, *Molecular immunology* **61**, 257 (2014).
28. R. Taylor, M. Lindorfer, E. Cook, C. Zent, R. Burack, F. Beurskens, J. Schuurman and P. Parren, The molecular sequence of events leading to complement-dependent cytotoxicity (CDC) is accelerated for CD20 antibodies harboring mutations that enhance hexamer formation. *Molecular Immunology* (2015); doi:10.1016/j.molimm.2015.03.013.
29. F. Beurskens, S. Derer, A. Tammen, J. Schuurman, P. Parren T. Valerius: Hexamerization of EGFR-directed antibodies induces potent complement-dependent cytotoxicity of tumor cells. *Molecular Immunology* (2015); doi:10.1016/j.molimm.2015.03.013.
30. S. Derer, M. Cossham, T. Rösner, C. Kellner, F. Beurskens, M. Peipp and T. Valerius: A complement-optimized EGFR antibody improves CR3-dependent cytotoxic functions of granulocytes against tumor cells via C5a. *Molecular Immunology* (2015); doi:10.1016/j.molimm.2015.03.013.
31. V. Irani, A. J. Guy, D. Andrew, J. G. Beeson, P. A. Ramsland, and J. S. Richards, Molecular properties of human IgG subclasses and their implications for designing therapeutic monoclonal antibodies against infectious diseases, *Molecular immunology* (2015); doi:10.1016/j.molimm.2015.03.255.
32. R. Kontermann, Dual targeting strategies with bispecific antibodies, *mAbs* **4,** 182-197 (2012).
33. M. L. Ford, Literature Watch Implications for transplantation, *American Journal of Transplantation* **15**, 1133 (2015).
34. D. M. Czajkowsky, J. T. Andersen, A. Fuchs, T. J. Wilson, D. Mekhaiel, M. Colonna, J. He, Z. Shao, D. A. Mitchell, and G. Wu, Developing the IVIG biomimetic, Hexa-Fc, for drug and vaccine applications, *Scientific reports* **5**, (2015).
35. R. Müller, M. A. Gräwert, T. Kern, T. Madl, J. Peschek, M. Sattler, M. Groll, and J. Buchner, High-resolution structures of the IgM Fc domains reveal principles of its hexamer formation, *Proceedings of the National Academy of Sciences* **110**, 10183-10188 (2013).
36. T. D. Randall, R. M. Parkhouse, and R. B. Corley, J chain synthesis and secretion of hexameric IgM is differentially regulated by lipopolysaccharide and interleukin 5, *Proceedings of the National Academy of Sciences* **89**, 962-966 (1992).
37. D. M. Czajkowsky and Z. Shao, The human IgM pentamer is a mushroom-shaped molecule with a flexural bias, *Proceedings of the National Academy of Sciences* **106**, 14960-14965 (2009).
38. A. Feinstein and E. A. Munn, Conformation of the free and antigen-bound IgM antibody molecules, *Nature* **224**, 1307-1309 (1969).
39. Q. Yin, T. M. Fu, J. Li, and H. Wu, Structural Biology of Innate Immunity, *Annual Review of*

Immunology **33**, (2015).
40. A. V. Hauenstein, L. Zhang, and H. Wu, The hierarchical structural architecture of inflammasomes, supramolecular inflammatory machines, *Current opinion in structural biology* **31**, 75-83 (2015).
41. G. A. Newby and S. Lindquist, Blessings in disguise: biological benefits of prion-like mechanisms, *Trends in cell biology* **23**, 251-259 (2013).
42. A. Lu and H. Wu, Structural mechanisms of inflammasome assembly, *FEBS Journal* **282**, 435-444 (2015).
43. A. Lu, V. G. Magupalli, J. Ruan, Q. Yin, M. K. Atianand, M. R. Vos, G. F. Schröder, K. A. Fitzgerald, H. Wu, and E. H. Egelman, Unified polymerization mechanism for the assembly of ASC-dependent inflammasomes, *Cell* **156**, 1193-1206 (2014).
44. S. M. Man, L. J. Hopkins, E. Nugent, S. Cox, I. M. Glück, P. Tourlomousis, J. A. Wright, P. Cicuta, T. P. Monie, and C. E. Bryant, Inflammasome activation causes dual recruitment of NLRC4 and NLRP3 to the same macromolecular complex, *Proceedings of the National Academy of Sciences* **111**, 7403-7408 (2014).
45. F. G. A. Faas, M. Barcena, A. V. Agronskaia, H. C. Gerritsen, K. B. Moscicka, C. A. Diebolder, L. F. van Driel, R. W. A. L. Limpens, E. Bos, and R. B. G. Ravelli, Localization of fluorescently labeled structures in frozen-hydrated samples using integrated light electron microscopy, *Journal of structural biology* **181**, 283-290 (2013).
46. M. Marko, C. Hsieh, R. Schalek, J. Frank, and C. Mannella, Focused-ion-beam thinning of frozen-hydrated biological specimens for cryo-electron microscopy, *Nature Methods* **4**, 215-218 (2007).

SAMENVATTENDE DISCUSSIE IN HET NEDERLANDS

HET NIEUWE TIJDPERK VAN CRYO-EM IN DE STRUCTUUR BIOLOGIE

Dit proefschrift beschrijft het structuur onderzoek met behulp van cryo elektronen microscopie (cryo-EM) naar twee immuun complexen die het immuun systeem activeren. Daarnaast is methodologisch werk gedaan dat gerelateerd is aan het oplossend vermogen (resolutie) die bereikbaar is met cryo-EM reconstructies: welke factoren zijn limiterend en hoe kan de resolutie in tomogrammen worden gemeten. In de afgelopen vijf jaar, sinds de start van het onderzoek dat in dit proefschrift is beschreven, zijn er cruciale methodologische doorbraken bereikt het onderzoeksveld van de cryo-EM die een grote impact hebben op de mogelijkheden die cryo-EM heeft met betrekking tot het ophelderen van eiwitcomplexen, inclusief die in dit proefschrift worden beschreven en gerelateerde immuun complexen.

Zoals wordt beschreven in **hoofdstuk 4,** waarin een overzicht wordt gegeven van de factoren die de resolutie in cryo elektronen tomogrammen beperken, is recentelijk cryo-EM belangrijker geworden binnen de structuur biologie. Diverse technische doorbraken hebben deze snelle ontwikkelingen mogelijk gemaakt. Wat betreft de apparatuur heeft het beschikbaar komen van steeds efficiëntere elektronen detectoren een enorme impact gehad, en zorgden deze detectoren voor opnames met een ongeëvenaarde kwaliteit van elektronen stralingsgevoelige structuren, vanwege hun dramatisch verbeterde modulatie transfer functie (MTF) en kwantum detectie efficiëntie (DQE). De huidige ontwikkelingen met betrekking tot deze types detectoren doelen op voornamelijk een verbetering van hun specificaties (*1*). Andere veelbelovende kenmerken van deze gevoelige detectoren zijn de mogelijkheden om met hoge snelheid opnames te maken in "film-modus", die het mogelijk maakt om de data achteraf te corrigeren voor elektronenbundel geïnduceerde beweging van het object, of om in "elektronen tel modus" super-resolutie data op te nemen bij twee maal de Nyquist frequentie door de locatie van de impact van de elektronen op de detector te bepalen met een nauwkeurigheid die kleiner is dan een pixel (*2*). Vanwege deze technische ontwikkelingen benaderen sommige reconstructies van eiwitdeeltjes die zijn gemaakt met cryo-EM het oplossend vermogen van modellen die gemaakt kunnen worden met Röntgendiffractie (*3*). Sinds april 2015 zijn de hoogste resolutie van reconstructies van eiwitdeeltjes die gedeponeerd zijn in de Elektronen Microscopische Data Bank (EMDB) de 2.6 Å icosaëdrisch symmetrische reconstructie van rotavirus VPI6, een zevenvoudig symmetrische (D7) proteasome structuur met een resolutie van 2.8 Å (*4*) en een 2.9 Å asymmetrische reconstructie (C1) van het *E.coli* ribosoom.

Een andere belangrijke ontwikkeling van apparatuur is het commercieel beschikbaar komen van de fase plaat, minder dan zes maanden geleden. Dit apparaat, dat geplaatst wordt in het imaginaire focusvlak van de objectief lens in de kolom van de elektronen microscoop, vergroot het contrast van het beeld (bij lage ruimtelijke frequenties) enorm door de fase van de bundel van elektronen die interactie met het sample hebben gehad met ½ π pi te verleggen ten opzichte van de doorvallende bundel. Dit fase verschil maakt het mogelijk om gevitrificeerde samples met hoog contrast af te beelden zonder te defocusseren. De opnames van de eerste experimenten met deze fase plaat laten inderdaad een spectaculaire verbetering van het beeld contrast zien. Lange tijd leek het erop

dat het Zernike-type fase plaat het meest veelbelovende ontwerp was (*5*). Echter, het bleek dat deze films in het dagelijks gebruik praktische problemen hadden met de stabiliteit, gerelateerd aan materiaalmoeheid van het koolvlies met gaten (de fase plaat). Deze instabiliteit maakt dat de fase plaat een regelmatige vervangen en uitgelijnd moet worden, wat hoge doorvoer van data hindert. Een veelbelovend alternatief voor de Zernike-type fase plaat, evenals andere voorgestelde types van fase platen die in de laatste decade zijn beschreven, was het onlangs beschreven ontwerp die de Volta fase plaat wordt genoemd (*6*). In de Volta fase plaat worden diverse technische moeilijkheden omzeilt door het maken van een "virtueel gat" in een continue koolstof film. De fase verandering wordt geïnduceerd "on-the-fly" (door en tijdens het belichten met de elektronen bundel) en wordt verklaard –ondanks dat het nog niet goed begrepen wordt – door elektronen bundel geïnduceerde oplading die een lokaal potentiaal op het vlies induceert die een fase verandering tot gevolg heeft op de onafgebroken elektronen bundel. In het bijzonder cryo-ET zal zijn voordeel doen met de fase plaat en de eerste onderzoeken zijn bezig om de mogelijkheden van deze technologie in kaart te brengen (*7,8*).

Buiten de apparatuur ontwikkelingen maakten ook de continue en voortdurende verbeteringen van de werkstroom in cryo-ET tijdens data collectie en beeldverwerking stappen een belangrijke verbetering in oplossend vermogen mogelijk dat kan worden behaald met het middelen van delen van tomogrammen (*9*). Een verbeterde resolutie is mogelijk gemaakt door optimalisatie van drie resolutie limiterende parameters: [I] het beperken van de elektronen dosis tot 40 e/ $Å^2$ om stralingsschade te verminderen, [II] verbeterde bepaling van de defocus waarde tot 100 nm. om de precieze contrast doorgang functie te corrigeren en [III] het opnemen van hele grote datasets, opgebouwd uit meer dan 30.000 asymmetrische unit cellen. Hiermee konden sub tomogram gemiddelden van immature HIV capsiden tot 8.8 Å resolutie bereikt worden (*11*). En zelfs de droom van 'structurele biologie in de cel' lijkt binnen bereik te zijn (*12*).
Wat betreft de software zijn er twee ontwikkelingen die een positief effect op de resolutie in cryo-EM hebben gehad door de twee voornaamste oplossend vermogen beperkende factoren in de beeldverwerking van cryo-EM data aan te pakken. Het eerste probleem is gerelateerd aan de vraag hoe beelden te classificeren uit een heterogene set van deeltjes. Structuur analyse door cryo-EM/ET zijn over het algemeen een wiskundig problemen zonder eenduidige oplossing omdat de opgenomen beelden vaak veel ruis hebben en niet compleet zijn. Een gevolg daarvan is dat de resulterende modellen gevoelig zijn voor model afwijkingen en het oplijnen van ruis bij hoge frequenties (het model beschrijft de ruis beter dan het signaal). Een oplossing voor dit probleem wordt gegeven door regularisatie door externe voorkennis. In the structurele biologie kan voorkennis bijvoorbeeld worden ingebracht door het invoegen van de oriëntatie van deeltjes, zoals de orthogonale richting van de 'C1-Eiffel torens' ten opzichte van de membraan van het liposoom zoals beschreven in **hoofdstuk 2**, of door het opleggen van symmetrie, zoals word aangenomen is in spiraal symmetrie in de reconstructie van het inflammasome in **hoofdstuk 3**. Echter, in veel gevallen is voorkennis beperkt en foute aannames leiden naar foute resultaten. Een meer algemeen aanvaardbaar ingebrachte voorkennis zou zijn de ruwe vorm van het biologische sample en, ten gevolge daarvan, kan low-pass (of een ander type van) ruimtelijke filtering in vele gevallen deel zijn van de strategie voor beeldverwerking. Maar ook, gerelateerd aan het filteren, de keuze van de filter parameters is niet rechttoe rechtaan en over-fitten is een gebruikelijk probleem

in elektronen microscopie (*13*).

Een recente doorbraak voor dit classificatie probleem is bereikt door de introductie van de meest waarschijnlijke schatter classificatie aanpakken die, meer en meer de supervisie classificatie heeft vervangen (*14,15*). Meest waarschijnlijke schatter classificatie heeft geen voorkennis nodig en resulteert in een meer robuuste en betrouwbare reconstructies. Zeker kleine datasets hebben nog steeds regularisatie door voorkennis nodig die geïncorporeerd kan worden in Bayseaanse waarschijnlijkheden (*16*). Deze gecombineerde "gereguleerde meest waarschijnlijke schatter" optimalisatie is geïmplementeerd in diverse EM beeldverwerkingsprogramma's (*17*) die hun overwinnende succes zijn gestart in structuur biologie.
Een tweede belangrijk issue dat is opgelost door geavanceerde beeldverwerking na het opnemen van de data is elektronen bundel geïnduceerde beweging van het preparaat (*18*). Conventionele ladingsgekoppeld component detectoren (CCD) zijn minder gevoelig voor de inkomende elektronen en hebben een relatief lange belichtingstijd nodig, die leid tot meer bewogen beelden vergeleken met de meest recente types directe elektronen detectoren. Deze detectoren maken het mogelijk om met een hoge snelheid korte filmpjes op te nemen. Specifieke algoritmen kunnen de individuele beelden van deze filmpjes oplijnen, en gecombineerd met het selecteren van specifieke beelden, heeft het zodanig mogelijk gemaakt om bijna atomair oplossend vermogen te halen in reconstructies van het ribosoom met maar 35.000 deeltjes (*19*). Tegenwoordig, worden meer geavanceerde algoritmes onderzocht voor het uitlijnen en combineren van deze filmpjes van nog uitdagendere, kleinere deeltjes (*20*).

Een ander relevante zaak in de context van de recente verbeteringen met betrekking tot het oplossend vermogen in cryo-EM is het gepast meten van het oplossend vermogen in de cryo-EM mappen. Diverse recente voorbeelden illustreren hoe makkelijk een structuur bioloog gevangen kan worden in de vallen die verborgen zijn in de ruis van de gereconstrueerde datasets. Zonder twijfel is het grootste gevaar het uitlijnen van ruis in door de gebruiker aangeleverde uitlijnmodellen, vaak omschreven als het "Einstein-uit-ruis" fenomeen (*13*). Diverse standaard voor beeldverwerking zijn in stelling gebracht om over interpretatie van cryo-EM reconstructies te voorkomen, bijvoorbeeld het gouden-standard Fourier schil correlatie (FSC) metingen en het opnemen van tilt-paar beelden (*21*). Andere geavanceerde resolutie schatting methoden doelen op het grip krijgen van het issue van anisotropie in het oplossend vermogen. Een lokaal criterium, eigenlijk een richtingscriterium, zoals beschreven in **hoofdstuk 5**, is voorgesteld voor eiwit reconstructies (*22*). Hier wordt de FSC berekend voor deel-volumes uit de berekende map. Onlangs is er een alternatieve lokale resolutiemeting geïntroduceerd die probeert de issues gerelateerd vaan de FSC gebaseerde methoden (*23*). Beide methoden moeten hun weg nog vinden in de elektronen tomografie en zouden, samen met de kegel FSC, bruikbaar kunnen blijken te zijn als validerend gereedschap in de structuur biologie. Echter, in het licht van de alsmaar verbeterende resolutie die bereikt kan worden met reconstructies van enkele deeltjes en het middelen van tomogramdelen moet men zich realiseren dat een enkel getal dat de resolutie aangeeft niet een doel is op zich. Aan de ene kant zijn FSC gebaseerde methoden meer een meting van de interne consistentie van een dataset en een ondubbelzinnige schatting van het oplossend vermogen kan alleen bereikt worden als de bereikte map van de losse deeltjesgoed genoeg is (beter dan 0.4 nm.) om te testen tegen atomaire

modellen.
Aan de andere kant, de reconstructies die door middel van cryo-ET worden gemaakt hebben een duidelijk mindere resolutie maar missen daardoor niet per se relevant informatie, zeker niet als de voortkomende conclusies van deze reconstructies ondersteund worden door andere structuur en functionele data. De gemiddelden van tomogram delen die beschreven worden in **hoofdstuk 2** zijn excellente voorbeelden. Beide hebben een oplossend vermogen dat beter is dan een paar nm. Desondanks en zonder twijfel zouden de gemiddelden die gepresenteerd worden in deze twee hoofdstukken enorm geprofiteerd hebben van de recente technische ontwikkelingen die hierboven worden beschreven. Hoogst waarschijnlijk kunnen in de nabije toekomst sensationele nieuwe resultaten verwacht worden van deze en vele andere macromoleculaire machine van reconstructies met hogere resolutie door cryo-ET.

Tot slot moet het benadrukt worden dat cryo-EM, vergeleken met andere methoden zoals Röntgen kristallografie, een relatief jonge techniek is in de structuur biologie. En buiten de issues van het bereiken en valideren van (hoge resolutie) cryo-EM mappen, moeten ook andere fundamentele zaken, die betrekking hebben op basale conventies en toegankelijkheid van data nog opgelost worden. In dit licht is er voortgang gemaakt met betrekking tot de data formaten (*24*) en met betrekking tot de mogelijkheden om om te gaan met grote hoeveelheden data die van verschillende modaliteiten komt (*25*), wat noodzakelijk werd na een periode van Babylonische verwarring. Een centraal element in deze recente ontwikkelingen is de beschikbaarheid en toegankelijkheid van de openbare data archieven. Terwijl het in de laatste vijf jaar gebruikelijk werd om een uiteindelijke 3D reconstructie samen met de bijbehorende ingepaste atomaire mappen in gerenommeerde databanken te deponeren, bijvoorbeeld de EMDB en de PDB, is dit nog niet het geval voor de ruwe data waarop de berekende mappen zijn gebaseerd. Desondanks is onlangs een databank voor elektronen microkopie beelden geïntroduceerd (EMPIAR) (*25*). Ondanks dat er slechts een handje vol dataset gedeponeerd zijn is onder deze sets de ruwe tilt serie van het C1-IgG hexameren uit **hoofdstuk 2** (EMPIAR-10009), de behoefte aan ruwe data depositie wordt om diverse redenen steeds duidelijker: om het verlies van data tegen te gaan, om een rigoureuze check van de validiteit van de wetenschappelijke claims mogelijk te maken, en om verbeteringen van de reconstructies en wetenschappelijke modellen door toekomstige methoden mogelijk te maken.

INZICHT IN KLASSIEKE COMPLEMENT ACTIVATIE EN DE OPBOUW VAN HET INFLAMMASOME GEBASEERD OP CRYO ELEKTRONEN TOMOGRAFIE.

Hoofdstuk 2 geeft een algemeen model voor de klassieke complement activatie door IgG antilichamen, die gebaseerd is op Fc gemedieerde hexamerisatie op antigene oppervlaktes. Deze bevinding staat aan de basis van een nieuwe technologie platform, de Hexabody™, die erop gericht is op de CDC (complement afhankelijke cytotoxiciteit) van therapeutische antilichamen te verbeteren door minimale veranderingen aan te brengen in de Fc domeinen, die de specificiteit van het antilichaam niet aantast (*26*). Een belangrijke mogelijke toepassing van deze CDC-verbeterde antilichamen is de behandeling van kanker. De eerste preklinische studies van diverse bloed kanker bindende antilichamen laten de mogelijkheden van deze technologie zien (*27*).

Verbeterde CDC die wordt geïnduceerd door de hexamerisatie van Fc is bevestigd in preklinische studies voor relevante bloed kanker targets CD20 en CD38 (*28*). Andere onderzoeken maken ook de impact van de geïnduceerde hexamerisatie duidelijk op therapeutische EGFR-antilichamen, die van nature geen CDC laat zien (*29*). Belangrijk om te vermelden is dat IgG hexamerisatie niet alleen CDC opwekt door het verbeteren van de ADCC op long en darmkanker cellen door vorming van C5a (*30*). Hexabodies zouden ook bruikbaar kunnen zijn voor het behandelen van infecties (*31*). Een reden zou kunnen zijn dat polyklonale antiserums vaak niet efficiënter zijn in het activeren van het compliment systeem dan individuele monoklonale antilichamen, mogelijk doordat gesimplificeerde hexameer formatie optreed bij lage antilichaam concentraties. Aan de ander kant, je gebruik van polyklonale antisera is niet wenselijk uit overwegingen van veiligheid en kwaliteit. Het is voor te stellen dat efficiënte antilichaam behandelingen in de toekomst zullen bestaan uit een mix van diverse monoklonale antilichamen met een variëteit in specificatie en affiniteiten en subklassen. Met betrekking tot een andere belangrijke bevinding die is beschreven in **hoofdstuk 2** –namelijk dat monovalente binding genoeg is of zelf beter is voor de CDC – lijken ook een combinatie van bi-specifieke antilichamen en/of antilichaam-drug conjugaties veelbelovend voor de behandeling van kanker en infecties (*32*). Nadere implicaties zijn gevonden die betrekkingen hebben op transplantatie, waar het voordelig is om CDC tegen te gaan. Het is gesuggereerd dat Fc binding peptiden, zoals gebruikt zijn in de studie gebruikt zou kunnen worden om afstoting van transplantaten te verminderen (*33*). Verder verklaart het IgG hexamerisatie model de hoge CDC capaciteit van hexameer Fc-fusie eiwitten die ontworpen waren intraveneuze immunoglobuline therapie (*34*).
Op het eerste gezicht lijkte de geassembleerde IgG hexameer sterk op de structuur van IgM, een antilichaam subklasse die in de mens van nature voorkomt als pentameren en hexameren (*35*). Beide zijn ook vergelijkbaar sterke activators (en voornamelijk de hexameer) van complement omdat C1q binding wordt gefaciliteerd door verhoogde binding zonder de voorwaarde dat er zes antilichaam monomeren moeten assembleren (*36*). Maar hoe wordt spontane activatie door IgM voorkomen in de afwezigheid van antigenen die in het geval van IgG de CDC geïnduceerde antilichaam laten clusteren? Men denkt dat IgM in oplossing een vorm aanneemt waarin C1q binding ruimtelijk verhinderd wordt en dat antigeen binding een grote ruimtelijke veranderingen opwekt die bindingsplaatsen toegankelijk maakt (*37*). Echter, toekomstige structuur studies, mogelijk ook cryo-EM, zijn nodig om dit "zeester-naar-nietje" hervormingsmodel te toetsen.

Cryo-ET is gebruikt in **hoofdstuk 3** om de quaternaire structuur van gepolymeriseerd NAIP5/NLRC4 inflammasome te bestuderen, die een spiraal bleek te vormen. Het passen van de recent gepubliceerde kristalstructuur van inactief NLRC4 resulteerde in een model voor activatie van deze NLR. Hoe kunnen deze structurele inzichten van NAIP5/NLRC4 complexen helpen om het mechanisme van inflammasome vorming helpen te begrijpen? Recente onderzoeksactiviteiten schijnen licht op de signaalmechanismen van deze heterogene groep cytosole patroon herkenningen receptoren (*39*). Ten minste voor de subgroep van ASC afhankelijke inflammasomen is een hiërarchisch gestructureerde architectuur voorgesteld (*40*) die gebaseerd is op de herkenning van liganden, vrijlating van zelf-inhibitie en genucleëerde prion-achtige polymerisatie (*41*). Inderdaad zijn zulke multimerisatie mechanismen gerapporteerd voor diverse inflammasome componenten, zoals bijvoorbeeld PYD geïnduceerde ASC polymerisatie en CARD geïnduceerde

caspase polymerisatie (*42*). De data die nu wordt gepresenteerd in **hoofdstuk 3** biedt bewijs dat dit ook het geval is voor NLRC4 tijdens de assemblage in het ASC onafhankelijke NAIP5/NLRC4 inflammasome. Het is inderdaad aanlokkelijk om de recent voorgestelde "eenduidige mechanismes van ASC afhankelijke inflammasome formatie" (*43*) uit te breiden naar hun ASC onafhankelijke leden. Ongetwijfeld laten de gepresenteerde resultaten urgente vragen open, waarvan de meeste belangrijke is: Hoe verklaart het huidige model voor NLR signaleren de enorme complexen en nog gecompliceerdere structuren die worden gezien in vivo door super-resolutie fluorescentie microscopie (*44*)? Deze vraag heeft een aanpak nodig die het structurele onderzoek verplaats van in vitro op gezuiverde componenten naar het in situ zichtbaar maken van geheel geassembleerde inflammasomen. Toekomstige experimenten doelen om dit geheim te ontrafelen zouden gebruik kunnen maken van geïntegreerde cryo- (super-resolutie) correlatieve licht en elektronen microscopie (*45*), en waarschijnlijk in combinatie met geavanceerde sample preparatie technieken zoals gefocusseerde ionen straal frezen van lamellen die hoge resolutie tomografie in de cel mogelijk maken (*46*).

ZUSAMMENFASSENDE DISKUSSION IN DEUTSCHER SPRACHE

DIE NEUE ÄRA DER KRYO-ELEKTRONENMIKROSKOPIE IN DER STRUKTURBIOLOGIE

Die vorliegende Arbeit beschreibt die strukturelle Erforschung zweier immunologischer Initiationskomplexe mittels Kryo-Elektronenmikroskopie (Kryo-EM). Zusätzlich wurde methodologische Arbeit mit dem Ziel durchgeführt die Auflösung von Kryo-EM-Rekonstruktionen zu verbessern. Zentrale in diesem Zusammenhang stehende Fragen sind: Welche Faktoren wirken sich auflösungslimitierend aus und wie kann die Auflösung in Tomogrammen überhaupt gemessen werden? Innerhalb der vergangenen fünf Jahre, während der Entstehung der vorliegenden Arbeit, wurden bahnbrechende methodische Entwicklungen im Feld der Kryo-EM erzielt. Diese Entwicklung hat bereits großen Einfluss auf die strukturbiologische Forschung. Beispiele dafür sind die hier beschriebenen immunologischen Proteinkomplexe.

Wie **Kapitel 4** zu entnehmen ist, das einen Überblick über die limitierenden Faktoren bezüglich der Auflösung der Kryoelektronentomografie gewährt, hat die Kryo-EM innerhalb der vergangenen Jahre erheblich an Bedeutung im Bereich der Strukturbiologie gewonnen. Zahlreiche technische Durchbrüche trugen zu dieser schnellen Entwicklung bei. Bezüglich der Apparatur hatten zunehmend verfügbare sensible und hochauflösende, direkte Elektronendetektoren einen großen Einfluss. Insbesondere bei der Abbildung von strahlungsempfindlichen Strukturen wurden hochauflösende Abbildungen beispielloser Qualität erreicht. Dies ist auf eine verbesserte Modulationsübertragungsfunktion (MTF) und Detektorquantenausbeute (DQE) zurückzuführen. Die gegenwärtige Weiterentwicklung derartiger Detektoren zielt auf eine weitere Verbesserung ihrer technischen Spezifikationen ab (*1*). Ein vielversprechendes Merkmal dieser sensiblen Detektoren besteht in der Aufnahme von Hochgeschwindigkeitssequenzen im „Filmaufzeichnungsmodus". Dieser erlaubt eine nachträgliche Korrektur der strahlungsinduzierten Probenbewegung. Des weiteren besteht die Möglichkeit der Aufnahme im „Elektronen- Zählmodus" für eine hochauflösende Datenerfassung bei zweifacher NyquistFrequenz; dies geschieht durch Positionsermittlung der auf dem Detektor auftreffenden Elektronen mit Sub-Pixel-Genauigkeit (*2*). Aufgrund dieser technologischen Entwicklungen weist die Kryo-EM-Einzelpartikel-Rekonstruktion in einigen Fällen eine Auflösung auf, die der der Kristallstrukturanalyse gleichkommt. Die Einzelpartikel-Rekonstruktion mit der höchsten Auflösung in der Electron Microscopy Data Bank (EMDB), (Stand April 2015) sind: Die 2,6 Å-Rekonstruktion des ikosaedrischen Rotavirus VP61, die symmetrische 2,8 Å-Rekonstruktion des Proteasoms (D7-Symmetrie) (*4*) und eine asymmetrische 2,9 Å-Rekonstruktion des *E.coli*-Ribosoms.

Seit kurzem kommerziell erhältliche stabile Phasenplatten stellen einen weiteren, äußerst bedeutenden Fortschritt in der Instrumentation dar. Dieses Bauteil, platziert in der hinteren Brennebene der Objektivlinse des Elektronenmikroskops, führt zu einer drastischen Erhöhung des niederfrequenten Bildkontrasts durch eine Phasenverschiebung des durch die Probe gestreuten Elektronenstrahls um $\pi/2$. Diese Phasenverschiebung ermöglicht eine kontrastreiche Abbildung von gefroren-hydratisierten Proben, ohne dass eine Unterfokussierung nötig wäre. Erste Experimente deuten tatsächlich auf eine spektakuläre Verbesserung des Bildkontrasts hin. Lange Zeit galt das Phasenplatten-Design nach Zernike als aussichtsreichstes. Mit dieser experimentellen Phasenplatte, die aus einer in der hinteren Brennebene positionierten Apertur besteht, wurden

vielversprechende Ergebnisse erzielt (*5*). Es stellte sich jedoch heraus, dass diese oder ähnliche Platten in der praktischen Anwendung Stabilitätsprobleme aufweisen, die auf Materialermüdung zurückzuführen sind. Diese Instabilität erfordert regelmäßigen Austausch und Re-Kalibrierung und ist somit einer Hochdurchsatz-Datenerfassung hinderlich. Eine vielversprechende Alternative zur Zernike-Phasenplatte und anderen Platten ähnlicher Bauart stellt die unlängst beschriebene sogenannte Volta-Phasenplatte dar (*6*). Diese Platte umgeht etliche technische Probleme durch die Generierung virtueller Löcher in einem aufgeheizten, unperforierten Kohlenstofffilm. Obwohl noch nicht völlig verstanden, wird die spontan induzierte Phasenverschiebung mit dem Aufbau eines strahlungsinduzierten, lokalen Ladungspotential auf dem Film erklärt, welches wiederum den umkehrenden Phasenverschiebungseffekt des ungestreuten Elektronenstrahls zur Folge hat. Insbesondere die Kryo-Elektronentomografie (Kryo-ET) wird zukünftig von der Phasenplatte profitieren und erste Studien untersuchen bereits das Potential dieser Technologie (*7,8*).

Neben Hardware-Entwicklungen fand zudem eine stetige Verbesserung der Arbeitsabläufe in Kryo-ET Datenerfassung und Datenverarbeitung statt. Dies führt zu einer gesteigerten Auflösung in der Sub-Tomogramm-Mittelung (*9*). Die verbesserte Auflösung wurde durch die Optimierung dreier auflösungslimitierender Parameter erzielt: [I] Beschränkung der Gesamtdosis auf 40 E/Å^2 und die damit verbundene Verminderung von Strahlungsschäden, [II] Bestimmung des Defokus mit einer Genauigkeit von 100 nm zwecks präziser CTF-Korrektur (*10*) und [III] Erhebung großer Datensätze bestehend aus >30.000 asymmetrischen Einheiten. Auf diese Weise konnten Sub-Tomogramm-Mittelungen unreifer HIV-Kapside mit einer Auflösung von 8,8 Å erreicht werden (*11*). Damit scheint der Traum der 'Strukturbiologie *in situ*' in greifbare Nähe zu rücken (*12*).

Hinsichtlich der Software gab es jüngst zwei Entwicklungen, die sich positiv auf die Auflösung in der Kryo-Elektronenmikroskopie auswirken. Hierdurch wurden zwei wichtige auflösungslimitierende Probleme in der Verarbeitung von Kryo-EM-Daten gelöst: Probenheterogenität und strahlungsinduzierte Bewegung. Das erste Problem betrifft die Frage, wie die Klassifizierung von Abbildungen einer heterogenen Probe vorgenommen werden kann. Unvollständige und verrauschte Datensätze stellen in der Kryo-EM und Kryo-ET bei der Strukturbestimmung ein unterbestimmtes mathematisches Problem dar. Hieraus ergeben sich häufig Modellbefangenheit und Überanpassung bei hohen Frequenzen (das Modell beschreibt vielmehr Rauschen als Signal). Eine Lösung für dieses Problem findet sich in der Regularisierung durch externes Vorwissen. Beispielsweise können Vorkenntnisse bezüglich der Pertikelorientierung berücksichtigt werden, so wie beispielsweise die vertikale Ausrichtung der „C1-Eiffeltürme" über der Liposommembran, wie in **Kapitel 2** beschrieben oder auch die in **Kapitel 3** angenommene helikale Symmetrie bei der Inflammasom-Rekonstruktion. In vielen Fällen ist *a priori*-Wissen jedoch nur begrenzt verfügbar und führt zu befangenen und damit fehlerhaften Ergebnissen. Ein allgemein gültiges, nützliches Vorwissen wäre beispielsweise die Ebenheit der biologischen Probe. Dementsprechend sind das Tiefpassfilter oder vergleichbare Filter Teil vieler Bildverarbeitungs-Pipelines. Zudem ist die korrekte Wahl der Filtereinstellungen nicht einfach und sog. Überanpassung ist ein wohlbekanntes Problem in der Elektronenmikroskopie (*13*). Die Einführung der „maximalen Wahrscheinlichkeits-Klassifizierung", stellt einen Durchbruch in der Frage nach den Klassifizierungskriterien dar. Sie steht im Begriff die überwachte Klassifizierung abzulösen (*14,15*). Die maximale Wahrscheinlichkeits-Klassifizierung bedarf keinerlei Vorwissens und führt zu wesentlich robusteren und zuverlässigeren Rekonstruktionen. Insbesondere bei kleinen Datensätzen herrscht weiterhin der Bedarf an

Regularisierung durch zusätzlichem *a priori*-Informationen, welche im Sinne des Bayesschen Wahrscheinlichkeitsbegriffs berücksichtigt werden können (*16*). Diese kombinierte „regularisierte Wahrscheinlichkeits-Optimierung" wurde bereits in einzelne EM-Bildverarbeitungspakete implementiert und hat einen triumphalen Einzug in die Strukturbiologie gehalten (*17*).

Ein zweites wichtiges Problem, das von der modernen Datenverarbeitung gelöst wurde, besteht in der strahlungsinduzierten Bewegung der Probe (18). Herkömmliche CCD-Sensoren reagieren weniger empfindlich auf auftreffende Elektronen und benötigen relativ lange Belichtungszeiten, was zur Bildunschärfe beiträgt. Bei den neuesten direkten Elektronendetektoren fällt diese deutlich geringer aus. Diese Art Detektoren ermöglichen eine Filmsequenz-Datenerfassung. Dedizierte Algorithmen, welche in der Lage sind eine derartige Sequenz zu alignieren, ermöglichten eine Ribosom-Rekonstruktion in beinahe atomarer Auflösung unter Verwendung von weniger als 35.000 Molekülen (*19*). Derzeit werden weitere Algorithmen entwickelt, welche eine entsprechende Verarbeitung von Datensätzen kleinerer Partikel ermöglicht (*20*).

In der Validierung von Kryo-EM-Karten und deren Auflösung besteht ein weiteres relevantes Problem dem sich neueste Entwicklungen in der Kryo-Elektronenmikroskopie widmen. Mehrere aktuelle Beispiele verdeutlichen, wie leicht der Strukturbiologe den Überblick verlieren kann, angesichts des Meeres an rekonstruierten Datensätzen und wie er sich im Rauschen dieses Meeres verlieren kann. Zweifelsohne stellt die Überanpassung befangener Modelle, oft auch als „Einstein-in-noise"-Phänomen bezeichnet, die größte Gefahrenquelle dar (*13*). Mehrere einheitliche Normen wurden festgelegt, um ein Überinterpretieren von Kryo-EM-Rekonstruktionen zu vermeiden. Hierzu zählen die Goldstandard-FSC-Messung oder die Tilt-Pair-Bildaufnahme (*21*).

Weitere Weiterentwicklungen zielen auf die Messbarkeit der Auflösungsanisotropie ab. Für die Einzelpartikelrekonstruktion (*22*) wurde kürzlich anstatt dem in **Kapitel 5** beschriebenen direktionalen Auflösungskriterium vielmehr ein lokales Auflösungskriterium vorgeschlagen. Hierbei wird die Fourier-Schalen-Korrelation (FSC) in Teilvolumen der rekonstruierten 3D-Karte vorgenommen. Zudem wurde einalternatives lokales Auflösungskriterium eingeführt, welches versucht die Nachteile FSC-basierter Methoden (*23*) zu umgehen. Beide Methoden müssen sich allerdings erst noch in der Elektronentomografie durchsetzen. Dann aber könnten sie sich durchaus gemeinsam mit der konischen Fourier-Schalen-Korrelation als nützliche Werkzeuge bei der Validierung strukturbiologischer Daten erweisen.

Im Lichte immer neuer Auflösungsrekorde sowohl in der Sub-Tomogramm-Mittelung als auch in der Einzelpartikelanalyse darf allerdings nicht vergessen werden, dass hohe nominale Auflösungswerte kein Selbstzweck sind. Einerseits sind FSC-basierte Methoden allenfalls als Maßstäbe interner Konsistenz anzusehen und die wirkliche Auflösung einer Einzelpartikelrekonstruktion kann lediglich dann akkurat bestimmt werden, wenn die wahre Auflösung 4Å unterschreitet, da nur bei diesen Werten eine Kreuzvalidierung mit atomaren Modellen durchführbar ist. Andererseits besitzen Rekonstruktionen mit geringer nominaler Auflösung, wie sie beispielsweise in der Kryo-Elektronentomografie gängig ist, nicht unbedingt weniger Aussagekraft; dies triff vor allem dann zu, wenn die Schlussfolgerungen durch weitere strukturelle und funktionelle Daten untermauert sind. Ein gutes Beispiel hierfür ist die Sub-Tomogramm-Mittelung aus **Kapitel 2**, welche lediglich über eine nominale Auflösung von mehreren Nanometern verfügt. Zweifellos hätte die Rekonstruction aber vom Einsatz der bereits beschriebenen technischen Neuerungen profitiert. Es ist daher anzunehmen, dass wir in naher Zukunft mit einer Flut von hochauflösenden Kryo-ET-

Rekonstruktionen von diesen und anderen makromolekularen Maschinerien rechnen können.
Verglichen mit anderen Methoden der Strukturbiologie, wie etwa der Kristallstrukturanalyse, handelt es sich bei der Kryo-Elektronenmikroskopie jedoch noch um eine recht junge Technik. So ist es nicht verwunderlich, dass neben offensichtlichen Fragen nach der Verbesserung und der Validierung der Auflösung von Kryo-EM-Karten, weiter reger Diskussionsbedarf bezüglich einheitlicher Konventionen oder freier Datenverfügbarkeit herrscht. Hinsichtlich der Vereinheitlichung von Dateiformaten (*24*) und der Schaffung von Rahmenbedingungen im Umgang mit großen Datensätzen verschiedener Modalitäten (*25*) wurden bereits wesentliche Fortschritte erzielt, was nach einer Phase babylonischer Verwirrung unabdinglich wurde. Zentrales Element einer jener Fortschritte stellen öffentlich zugängliche Datenbanken dar. Während es mittlerweile gängiger Praxis entspricht, publizierte EM-Modelle in einschlägigen Datenbanken wie der *EMDB* oder der *PDB* zu hinterlegen, trifft dies auf die zugrunde liegenden Rohdaten noch nicht zu. Abhilfe könnte eine vor Kurzem etablierte eine Datenbank für Roh-Mikroskopische Aufnahmen schaffen, das sogenannte *Electron Microscopy Pilot Image Archive* (*EMPIAR*; *25*). Bisher wurden jedoch nur wenige Rohdatensätze hinterlegt, darunter u.a. die Kippserien der C1-IgG_6-Komplexe aus **Kapitel 2** (*EMPIAR*-Eintrag 10009). Dabei ist eine entsprechende Archivierung aus vielerlei Gründen unerlässlich um: Datenverlust zu vermeiden, ein gründliches Peer-Review zu gewährleisten, die Grundlage wissenschaftlicher Aussagen zu überprüfen, Testdatensätze verfügbar zu machen und um Raum für die Verbesserung von Rekonstruktionen und resultierenden Modellen durch zukünftige Methoden zu ermöglichen.

EINBLICKE IN DIE VORGÄNGE DER KLASSISCHEN KOMPLEMENTAKTIVIERUNG UND DER INFLAMMASOM-BILDUNG MITTELS KRYO-ELEKTRONENTOMOGRAFIE

Kapitel 2 liefert ein allgemeingültiges Modell für den klassischen Aktivierungsweg des Komplementsystems durch IgG-Antikörper (Immunglobuline). Diese Aktivierung fußt auf einer Fc-vermittelten Hexamerisierung auf haptenierten Oberflächen. Dieses Ergebnis inspirierte eine neuartige translationale Technologieplattform, den sogenannten HexaBody™. Mithilfe dieser Plattform wird eine Optimierung der komplementvermittelten Zytotoxizität (engl. CDC) von therapeutischen Antikörpern durch minimales Fc-Engineering erreicht, ohne dabei jedoch sonstige Eigenschaften wie Affinität und Spezifität des Ausgangsantikörpers zu verändern. Die Krebstherapie gehört zu einer der möglichen Anwendungsspektren solcher CDC-verstärkten Antikörper. Erste präklinische Studien mit verschiedenen Antikörpern zur Behandlung maligner Blutzelllinien lassen bereits das Potential dieser Technologie erahnen (*27*). Verstärkte, durch Fc-Hexamerisierung induzierte, CDC wurde in präklinischen Studien für die relevanten Blutkrebs-Angriffspunkte CD20 und CD38 bestätigt (*28*). Weitere Studien belegen überdies die Auswirkungen induzierter Hexamerisierung auf therapeutische EGF-Rezeptor-Antikörper, welche üblicherweise keine Fähigkeit zur komplementabhängigen Zytotoxizität besitzen (*29*). Bemerkenswerterweise induziert IgG-Hexamerisierung in diesem Fall nicht nur CDC, sondern verstärkt auch eine antikörperabhängige, zellvermittelte Toxizität (engl. ADCC) gegenüber Lungen- und Dickdarmkrebszellen. Dieser Vorgang wird durch die Bildung des Anaphylatoxins C5a hervorgerufen (*30*).

Ferner könnten sich Hexabodies bei der Behandlung von Infektionskrankheiten ebenfalls als hilfreich erweisen. Interessanterweise haben monoklonale Antikörper bisher noch keine breite Anwendung bei der Behandlung von Infektionen finden können (*31*). Einer der Gründe hierfür könnte darin liegen, dass polyklonale Antiseren oftmals effizientere Komplementaktivierer sind als dies bei monoklonalen Antikörpern der Fall ist. Dies ist vermutlich auf erleichterte Hexamerisierung speziell bei geringer Antigendichte zurückzuführen. Allerdings ist die Verwendung polyklonaler Antiseren aus Sicherheits- und Qualitätsgründen nicht erstrebenswert. Es ist vorstellbar, dass effiziente Antikörpertherapien zukünftig aus einer Mischung unterschiedlicher monoklonaler Antikörper bestehen werden, welche ihrerseits eine Vielzahl unterschiedlicher Spezifitäten, Affinitäten und Sub-Klassen umfassen wird.
Ein weiteres wichtiges in **Kapitel 2** diskutiertes Ergebnis ist das der monovalenten Bindung und dessen vorteilhafte Auswirkung auf die komplementvermittelte Zytotoxizität. Eine Kombinationstherapie mit bispezifischen Antikörpern und/oder Antikörper-WirkstoffKonjugaten bei der Behandlung von Krebs und Infektionskrankheiten erscheinen daher sinnvoll (*32*). Andere Implikationen ergeben sich für die Transplantationsmedizin, in der eine Komplement-Inhibierung angestrebt wird. So wurde der Einsatz von Fc-bindenden Peptiden, wie sie in dieser Studie verwendet wurden, vorgeschlagen, um Transplantatabstoßungen zu unterdrücken (*33*). Des Weiteren erklärt das Modell der IgG-Hexamerisierung die hohe CDC-Aktivität hexamerer Fc-Fusionsproteine deren Einsatz aus der intravenösen Immunoglobulin-Therapie bekannt ist.
Auf den ersten Blick ähnelt das IgG-Hexamer stark der Struktur des IgM-Antikörpers (Immunoglobin M), welcher im Menschen als natürlicher Pentamer oder Hexamer auftritt. Entsprechend sind beide (jedoch insbesondere IgM-Hexamer) Komplement-Aktivatoren, da die Bindung von C1q durch erhöhte Avidität erleichtert wird, ohne dass eine Zusammenlagerung von sechs Monomeren erforderlich wäre (*36*). Aber wie wird eine spontane Komplementaktivierung durch IgM in Abwesenheit von Antigenen, die im Fall von IgG ursächlich für Antikörper-Clustering sind, verhindert? Es wird vermutet, dass IgM in Lösung eine Konformation besitzt, in der C1q sterisch daran gehindert wird zu binden und dass Antigenbindung eine erhebliche Konformationsänderung verursacht, die die Bindestellen zugänglich macht (*37*). Jedoch müssen zukünftige Studien (womöglich unter Einbeziehung der Kryo-EM) zeigen, ob diese als „starfish-to-staple" bezeichnete Konformationsänderung sich tatsächlich als wahr herausstellt.

Kryo-ET wurde auch in **Kapitel 3** eingesetzt, um die Quartärstruktur des polymerisierten NAIP5-NLRC4-Inflammasoms zu untersuchen. Hierbei stellte sich heraus, dass dieses sich in einer Helix anordnet. Ein Vegleich mit der kürzlich veröffentlichten Kristallstruktur des inaktiven NLRC4 resultierte in einem Aktivierungsmodell für diesen NOD-ähnlichen Rezeptor (engl. NLR). Es stellt sich die Frage, wie uns diese strukturellen Einblicke in den NAIP5-NLRC4-Komplex dazu beitragen können die grundlegenden Mechanismen der Inflammasom-Assemblierung zu verstehen? Forschungsaktivität der jüngsten Vergangenheit gewährt Einblicke in die Signaltransduktionsmechanismen dieser heterogenen Gruppe zytosolischer Mustererkennungsrezeptoren (*39*). Zumindest für die Untergruppe der ASC-abhängigen Inflammasome hat sich ein hierarchisches Aktivierungsmodell durchgesetzt (*40*). Dies basiert auf Ligandenerkennung, dem Lösen der Autoinhibierung und Keimbildung für Prion-ähnliche Polymerisierung (*41*). Tatsächlich wurde solch ein Multimerisierungs-Mechanismus für

verschiedene Inflammasom-Komponenten beschrieben, wie beispielsweise für PYD-induzierte ASC-Polymerisierung und CARD-induzierte Caspasen-Polymerisierung (*42*). Die in **Kapitel 3** veröffentlichten Daten sind ein erster Anhaltspunkt für die Vermutung, dass dies auch für NLRC4 während der Zusammenlagerung des ASC-unabhängigen NAIP5-NLRC4-Inflammasoms der Fall ist. Die Versuchung ist in der Tat groß das vorgeschlagene „vereinte Aktivierungsmodell ASC-abhängiger Inflammasomen" (*43*) auf seine ASC-unabhängigen Mitglieder auszuweiten.

Zweifellos drängen uns die Ergebnisse einige Fragen auf. Die vermutlich dringendste lautet hierbei wohl: Wie kann das derzeitige Model der NLR-Signaltransduktion die enormen und sehr viel komplexeren Strukturen erklären, wie sie in Fluoreszenz-Mikroskopie *in vivo* beobachtet werden (*44*)? Die Beantwortung dieser Frage erfordert den Übergang von der Untersuchung isolierter Bestandteile zur in situ-Darstellung komplett assemblierter Inflammasomen. Zukünftige Experimente mit dem Ziel diesem Geheimnis auf die Spur zu kommen werden womöglich (integrierte) Kryo-(superauflösende), korrelative Licht-und Elektronenmikroskopie (*45*) beinhalten – vermutlich in Kombination mit weiterentwickelten Probenpräparationstechniken wie etwa dem Lammellenfräsen mit fokussierten Ionensrahlen (engl. FIB-milling), die hochauflösende zelluläre Elektronentomografie erlauben (*46*).

ACKNOWLEDGEMENTS

Just in case that you aren't much involved in things like complement, inflammasomes, electron tomography, conical Fourier shell correlation, structural biology or scientific research in general, I'd like to tell you two things: First, the fact that you kept on reading until here means you are very brave, I am proud of you, soon it is over (real professionals always start here, next time you know). Second, you might ask yourself how it's possible that a single person decides to solve a more or less important research question, designs, performs and repeats many more or less clever experiments, interprets all the more or less meaningful data, and many years later comes up with a more or less useful booklet like this? Well, it is not. Such a huge task cannot be completed by a single person. Many brains, hands, wallets and hearts are needed for this, and now it is time to acknowledge their contribution:

First of all, I would like to express my gratitude to my promotors, Piet, Bram, and Roman. You have been my triumvirate over the years, and together you promoted me to this point. Piet, doing a PhD isn't always easy, and keeping a PhD student motivated is probably the most important task for a promotor. And honestly, your contagious excitement about a new result was always sufficient motivation for me to go ahead. Having scientific discussions or writing papers with you together is a great experience and a lot of fun! I am feeling honored to have been able to solve -with your help- one of the big mysteries of complement activation. Bram, my 'complementing' promotor, you always supported me and had an open ear for all questions, worries and complains. I've been profiting a lot from your pioneering work and deep knowledge about electron microscopes. Not least by providing an excellently equipped lab you enabled me to perform any experiment I could have wished for. Roman, you have been my daily supervisor since my first day as student in the Netherlands you are contributing the most to my scientific career. I could now make a long list with things I owe you thanks for, but I want to particularly thank you for the most valuable thing, your friendship.

Next, I want to thank my close collaborators I worked together with on the various projects described in this thesis. Els and Eric, thank you for 'recruiting' me for the inflammasome project. What started as a little side project developed to a very intense collaboration, and, after some difficulties yielded in some really enjoyable publications. And on top I am now unerringly able to tell apart butterflies, left and right-handed caterpillars, starships, diablos, and hourglasses, thanks. Frank B., Paul, Rob, Kristine and Janine. The collaboration with you guys at Genmab (of course together with Sara and Albert Heck from Utrecht and all the Americans) was a truly lucky occurrence for me and resulted in a really special story we can all be proud of! Good luck with the HexaBody™, I am looking forward to the day it saves a first life! Frank F.: How many times did I enter your office to ask you trivial computer related questions, to admit that I burned some CPUs or demand a software package that could simultaneously calculate conical Fourier shell correlations, write my thesis and cook coffee? Sorry, I will never be able to bring you enough cookies to pay for that. Ronald, thanks for saddling my daily workhorse, the F20. (BTW, F20, buddy, I hear you are slowly recovering from surgery, but I guess being an $Icorr^+$ doesn't feel bad after all, thank you for making all these nice images over the years! At this point it is time to also mention all the people at FEI who made many of my favorite "toys" and whom I had the chance to work with).

Doing a PhD in two different labs has both advantages and disadvantages (just to be clear here, the

pros clearly outweigh the cons, I highly recommend everyone to do it). However, when it comes to acknowledge the colleagues for their helping hand, advice or an enjoyable coffee break, a clear disadvantage is the risk of forgetting to mention someone and I already sincerely apologize if this this happened here.

First, I would like to thank all current and former members of the electron microscopy unit at the Leiden University Medical Center. Montse, Carolina, Cristina, Jos, Erik, Aat, Mieke, Karine, Jack, Marco, Sacha and Raimond. It was really a pleasure having you around all these years and to learn from you! Next, my regards to all postdocs, PhD students and students: Thom, Milos, Mani, Fateme, all Kasias, Kévin, Linda, Lennard, Wil, Daphne, Joost, Tom, Sander and Gert-Jan, having you guys in the lab was always great fun! Now some special words to my fellow PhD students: Marjon, my lab sister, since our first baby-steps as researchers until some days ago we shared an office. Thank you for your support and the great time (we *still* have to drink a bottle)! Barbara, I learned so much from you about movies, 'music' and funny animal pictures. Thanks for arranging all these movie nights! Charlotte, thanks for providing me and the rabbits with all the delicious calories, you're the best bunny sitter ever! ~~F20~~, Maarten, take care of your new buddy ~~Maarten~~ F20, you'll get used to ~~him~~ it! Of course, many additional thanks to the daylight MCB-people for countless daylight coffee breaks and Willem for keeping my PC running.

Let's make a move to my second home, the crystal and structural chemistry group in Utrecht. Foremost I'd like to thank all those who instinctively seek shelter upon hearing the phrase 'come to the meeting!'. Pramod, Xiaoguang, Deniz, Remco, Camilla, Revina, Joke, Ramesh, Michael, Federico, Jin, joining group meetings with you made me a real complementologist (although, some of you tried, I'll never be a proper biochemist or crystallographer though, forget it). However, *not* to forget all the others from Crystal and structural chemistry group: Loes, Bert, Martin, Cecile, Koutar, Arie, Joke, Caroline, Louris, Matti, Hedwich, Nadia, Tim, Tom, Toine, Ton, Ramesh, Harma, the Arjens, Dennis and the UPEs. Thanks for providing me with such a friendly work environment. Even though I did not spend most of the time with you, I never felt like a guest of even a stranger, but as a real group member, thank you (some people say that's only because I only showed up for pleasant duties like X-mas dinners, lab outings, trips to Istanbul, Christmas markets or to the black forest, sports, poker and drinks. Well, maybe, so what?)! Some special thanks to Peng, you've been a great mate throughout the years, and it was an honor to be your paranymph!

Leaving the home country to do a PhD isn't necessarily an easy thing, and indeed that is true. However, the easiest is not always the best, and I must say that coming to the Netherlands has been one of the best decisions in my life. Holland is my new home (Ja hoor, ik praat nog steeds niet lekker Nederlands, maar misschien heb ik nog even wat tijd nodig, dus blijf ik nog een beetje, groetjes naar de mensen bij NeCEN), and many people have been contributing to this. Thanks to my former housemates at Akkerhoornbloem, in particular Janine, thank you for your support when I badly needed it. Some extra thanks to the people in my new neighborhood, in particular all Franks for the nice flowers and the tasty bagels.

Of course I don't forget my roots, und darum wechsle ich jetzt mal die Sprache. Ich möchte mich zunächst mal bei meinem ersten Mentor aus Stuttgarter Zeiten bedanken. Mike, danke, dass du mir die Elektronenmikroskopie nahegebracht hast, hat sich doch gelohnt, oder? Natürlich schöne Grüße an meine ehemaligen Kommilitonen! Besondere Freundschaften verdienen besondere Erwähnung. Marc und Sebastian, danke für die sprichwörtlich guten alten Zeiten!

Und dann ist da natürlich meine Familie. Selbige hat sich vor einigen Jahren schlagartig um die Streks vergrößert, worauf ich ganz besonders stolz bin. Diedtmuth, Farina, Rickmer (allzeit gut Flug), Tabea (besonderen Dank für deinen editoriellen Input), Andrew, Steffi, Mateo, bin so froh zum Clan zu gehören, mit Euch ist es niemals langweilig! Meine lieben Münchener, ich weiß, ich melde mich viel zu selten, wird Zeit dass ich mal wieder auf ein Weißbier vorbeikomme (oder auch zwei. Ja, besser zwei!). Jörg und Philipp. Wenn Ihr es nicht schon wärt würde ich sagen: Ihr seid wie Brüder zu mir, danke dass Ihr heute meine Paranimfen seid! Mama, Papa, Euch bin ich ganz besonders dankbar, für alles, ich hab mir noch nie eine bessere Familie vorstellen können! Ich verkneife mir jetzt die berühmte, last-but-not-least Floskel, meine liebe Linda. Denn damit würde ich dir nicht gerecht werden. Denn du bist einfach das Beste, was es gibt, und entsprechend dankbar bin ich. Punkt.

CURRICULUM VITAE

Christoph Diebolder was born on 4th April 1981 in Geislingen an der Steige, Germany, where he completed the secondary school in 2001 followed by one year of civilian service in the local hospital. He took up studies in Technical Biology as undergraduate and graduate student at the University of Stuttgart. During these studies he worked in the in the group of PD Dr. Michael Schweikert at the Institute of Biology on the ultra structure of bacterial inclusion bodies and wrote his thesis about the genome structure of the bacteriophage MS2 after a first research stay with dr. Roman Koning at the Leiden University Medical Center in 2008. After receiving his Diploma degree in 2009, he moved to the Netherlands to start his PhD research in the groups of prof. Piet Gros at Utrecht University and prof. Bram Koster at the Leiden University Medical Center. His research under supervision of dr. Roman Koning was focused on structural immunology using and developing cryo-electron tomography as principal technique. In 2014, Christoph Diebolder joined the group of Bram Koster as researcher and became facility operator at the Netherlands Center for Electron Nanoscopy (NeCEN) in 2015.

LIST OF PUBLICATIONS

C. A. Diebolder, E. F. Halff, A. J. Koster, E. G. Huizinga, R. I. Koning, Cryo-Electron Tomography of the NAIP5-NLRC4 Inflammasome - Implications for NLR Activation, *submitted*.

C. A. Diebolder, F.G.A. Faas, A. J. Koster, and R. I. Koning, Conical Fourier Shell Correlation Applied to Electron tomograms, *Jounal of Structural Biology* **190**, 215-223 (2015).

C. A. Diebolder, F. J. Beurskens, R. N. de Jong, R. I. Koning, K. Strumane, M. A. Lindorfer, M. Voorhorst, D. Ugurlar, S. Rosati, A. J. Heck, J. G. van de Winkel, I. A. Wilson, A. J. Koster, R. P. Taylor, E. Ollmann Saphire, D. R. Burton, J. Schuurman, P. Gros, and P. W. Parren, Complement Is Activated by IgG Hexamers Assembled at the Cell Surface, *Science* **343**, 1260-1263 (2014).

F.G.A. Faas,M. Bárcena, A.V. Agronskaia, H. C. Gerritsenc, K.B. Moscicka, **C.A. Diebolder**, L.F. van Driel, R.W.A.L. Limpens, E. Bos, R.B.G. Ravelli, R.I. Koning , A. J. Koster, Localization of fluorescently labeled structures in frozen-hydrated samples using integrated light electron microscopy, *Journal of Structural Biology* **181**. 283-290 (2013)

E. F. Halff, **C. A. Diebolder**, M. Versteeg, A. Schouten, T. H. Brondijk, and E. G. Huizinga, Formation and structure of a NAIP5-NLRC4 inflammasome induced by direct interactions with conserved N-and C-terminal regions of flagellin, *Journal of Biological Chemistry* **287**, 38460-38472 (2012).

C. A. Diebolder, A. J. Koster, and R. I. Koning, Pushing the resolution limits in cryo electron tomography of biological structures, *Journal of Microscopy* **248**, 1-5 (2012).

SHORTLIST OF FREQUENTLY USED ABBREVIATIONS

C1	complement component 1, consisting of C1q, $C1r_2$ and $C1s_2$
CARD	caspase activation and recruitment domain
Caspase1	cysteine-dependent aspartate-directed protease 1
CDC	complement dependent cytotoxicity
cFSCe/o	conical Fourier shell correlation of eben/odd split datasets
CP	classical pathway of complement activation
CTF	contrast transfer function
DNP	dinitrophenyl
DQE	detector quantum efficiency
EM	electron microscopy
ET	electrontomography
Fab	fragment antigen binding
Fc	fragment crystallizing
(F)FT	(fast) Fourier transform
FLIC-$D0_L$	larger D0 construct of Salmonella flagellin
FSC	Fourier shell correlation
IgG	Immunoglobulin G
IL-1β	interleucin 1β
LRR	leucin rich repeat
MTF	modulation transfer function
NACHT	NAIP, CIITA , HET-E and TP1
NAIP	NLR family, apoptosis inhibitory protein
NBD	nucleotide binding domain
NLR	NOD-like receptor
NOD	nucleotide-binding oligomerization domain
PAMP	pathogen associated molecular pattern
PRR	PAMP recognition receptor
TEM	transmission electron microscopy
(W)HD	(winged) helix domain

And they all lived happily ever after.
Jonas Jonasson, The 100-Year-Old Man Who Climbed Out the Window and Disappeared